UNIVERSITY OF CALIFORNIA

Los Angeles

Integrated Wirelessly Powered Solutions for Medical Implants and Internet of Things

A dissertation submitted in partial satisfaction
of the requirements for the degree
Doctor of Philosophy in Electrical and Computer Engineering

by

Hamed Rahmani

2020

ABSTRACT OF THE DISSERTATION

Integrated Wirelessly Powered Solutions
for Medical Implants and Internet of Things

by

Hamed Rahmani
Doctor of Philosophy in Electrical and Computer Engineering
University of California, Los Angeles, 2020
Professor Aydin Babakhani, Chair

Wireless system-on-chip devices are emerging as the most promising solution for future wireless sensing with applications in medical implants and the Internet of Things (IoT). On one side, energy extraction from ambient sources facilitates permanent powering techniques required for long-term operation. On the other side, the high integration capability of commercial CMOS technology opens the opportunity for high-resolution sensing and data communication with a compact form-factor. In this dissertation, My research builds a foundation for joint wireless power delivery, low-power sensing, and wireless communication in such highly integrated systems yielding a paradigm shift in the design and development of future ubiquitous low-power wireless systems.

This thesis presents the design, implementation, and experimental evaluation of integrated wirelessly powered solutions for next-generation medical implants and IoT devices. To this end, First, I leverage the high integration capabilities of CMOS technology and try to develop integrated systems for power delivery, environmental sensing, and wireless data communication. The small power budget available for an integrated solution

severely limits its functionality and operating range. Hence, individual wirelessly powered solutions may not be able to satisfy the application requirements of future medical implants and IoT devices. To address this problem, I leverage another important feature of a commercial CMOS technology that is the low fabrication cost. I show how complex tasks such as localization and be realized using a swarm of millimeter-sized integrated chips.

In this dissertation, I introduce the challenges of wireless power transmission to fully integrated systems on CMOS technology and present two types of RF power receiver systems for near-field and far-field electromagnetic region. I propose a comprehensive optimization algorithm for maximizing the power transfer efficiency and choosing the optimum frequency for wireless power transmission.

Next, I present the world's most power-efficient wireless transceiver with an integrated wireless power delivery system. I demonstrate a fully on-chip operation and utilize two sets of loop and dipole antenna for wireless power delivery and data communication, respectively. I will explain how we achieve a 150 Mbps uplink communication data rate under a stringent power budget by introducing a power management technique.

I will then, discuss the opportunities offered by this platform to enhance next-generation IoT and medical devices. In particular, we tackle the limited operating range by forming a synchronized distributed sensor network built from fully on-chip integrated systems. Also, we address the power scarcity challenges in biomedical/environmental sensing by adopting extensive low-power design techniques.

This interdisciplinary research direction incorporates advancements such as applied physics, machine learning, healthcare, and wireless networking.

The dissertation of Hamed Rahmani is approved.

Chih-Kong Ken Yang

Dejan Markovic

Danijela Cabric

Aydin Babakhani, Committee Chair

University of California, Los Angeles

2020

To the memory of my mother . . .

TABLE OF CONTENTS

LIST OF FIGURES

LIST OF TABLES

ACKNOWLEDGMENTS

Now that my Ph.D. endeavor is coming to an end, I would like to extend my gratitude to those people who helped me during this journey.

First, I would like to thank my thesis supervisor, Professor Aydin Babakhani. I have gained many valuable experiences working with him that will certainly help me during my professional career.

I am also grateful to Professor Danijela Cabric, Professor Dejan Markovic, and Professor C.K. Ken Yang for serving on my thesis committee and providing constructive feedback after my Ph.D. candidacy. Their technical input greatly helped me in preparing this dissertation.

I thank Professors Sudhakar Pamarti, Shervin Moloudi, Ethan Wang, Hoomad Darabi, Behzad Razavi, and Danijela Cabric for their wonderful graduate courses. Attending their courses at UCLA has greatly helped me to broaden my insight into different aspects of Electrical engineering. Also, I had the opportunity to discuss some of the technical aspects of my research projects with them and benefit from their knowledge and experiences.

I feel fortunate for having amazing collaborators during my Ph.D. studies. I want to express my gratitude to Dr. Hilary Coller (Biological Chemistry Department, UCLA) and Dr. Philip Scumpia (UCLA, Medicine). Their expertise and knowledge greatly helped me during the wound sensing project.

I am thankful to all members of UCLA Integrated Sensors Laboratory and Rice Integrated Circuits Systems group: Dr. Babak Jamali, Dr. Yuxiang Sun, Dr. Jaeeun Jang, Sam Razavian, Mostafa Hosseini, Yash Mehta, Mahdi Forghani, Iman habibagahi, Dr. Mahdi Assefzadeh, Dr. Peiyu Chen, Dr. Charles Chen, Dr. Himashu Aggrawal, and Dr. Xuebei Yang. In particular, I want to thank Babak for helping me through the early stages of my research. Besides, I enjoyed many conversations we had about different topics that helped me to keep my mind off the work and stay fresh.

The long working hours and the challenges one may face toward completion of a Ph.D.

degree may sometimes become tedious. I was fortunate enough to have many friends around me whom I could talk with and enjoy their company. I want to thank my friends at UCLA and Rice: Seyyed Mohammad Kazempour, Babak Jamali, Hossein Razavi, Mehrdad Babamir, Hani Esmaeelzadeh, Mahmoud Elhebeary, Shi Bu, and Jiyue Yang.

Most of all, I want to thank my family, Farhad, Maryam, Mahdie, Zahra, Masoud, and Parisa. Words cannot express how grateful I am to them for their infinite patience and their support and sacrifice. It is so unfortunate that I have not met them over five years due to F-1 visa limitations and travel ban. Most importantly, I want to thank my best friend and my wife, Yasaman, without whom it would not be possible to complete this journey. Her love and support have always kept me going through any difficulties. As a fellow graduate student, I also had the chance to discuss technical aspects of my research with her and benefited from her technical input and valuable feedback toward the completion of this dissertation.

VITA

2014	B.Sc. (Electrical Engineering) Sharif University of Technology, Tehran, Iran.
2014	Rice Electrical and Computer Engineering Fellowship Rice University, Houston, TX.
2014–2017	Graduate Research Assistant Rice University, Houston, TX.
2014–2017	Texas Instruments Distinguished Fellowship Rice University, Houston, TX.
2017	M.Sc. (Electrical and Computer Engineering) Rice University, Houston, TX.
2018	RFIC Design Engineering Intern Qualcomm Technologies, Inc., San Diego, California.
2018	Advanced to PhD Candidacy University of California, Los Angeles.
2019	Microwave Theory and Techniques Society Graduate Fellowship for Medical Applications University of California, Los Angeles.
2018–Present	Graduate Research Assistant University of California, Los Angeles.

PUBLICATIONS

1- **H. Rahmani**, Y. Sun, M. Kherwa, S. Pal, A. Babakhani,"Coherent Radiation from a Swarm of Wirelessly Powered and Synchronized Sensor Nodes," *IEEE Sensors Journal,2020.*

2- **H. Rahmani***, M. Archang*, B. Jamali*, M Forghani, A. Ambrus, D. Ramalingam, Z. Sun, P. Scumpia, H. Coller, A. Babakhani"Towards a Machine-Learning-Assisted Dielectric Sensing Platform for Point-of-Care Wound Monitoring," *IEEE Sensors Letters, 2020.* * Equally contributed authors.

3- **H. Rahmani**, A. Babakhani,"An Integrated Battery-Less Wirelessly Powered RFID Tag with Clock Recovery and Data Transmitter for UWB Localization," *International Microwave Symposium (IMS), 2020.*

4- **H. Rahmani**, A. Babakhani,"A 1.6mm^3 Wirelessly Powered Reconfigurable FDD Radio with On-Chip Antennas Achieving 4.7pJ/b TX and 1pJ/b RX Energy Efficiencie," *Custom Integrated Circuit Conference (CICC), March 2020.*

5- **H. Rahmani**, A. Babakhani,"A Dual-Mode RF Power Harvesting System With an On-Chip Coil in 180-nm SOI CMOS for mm-Sized Biomedical Implants," *IEEE Transactions on Microwave Theory and Techniques.*

6- **H. Rahmani**, A. Babakhani, "A 434 MHz Dual-Mode Power Harvesting System with an On-chip Coil in 180 nm CMOS SOI for mm-Sized Implants," *International Microwave Symposium (IMS)*, 2018.

7- **H. Rahmani**, A. Babakhani, "A Wireless Power Receiver with an On-chip Antenna for Millimeter-size Biomedical Implants in 180 nm SOI CMOS," *International Microwave Symposium (IMS)*, 2017.

8- **H. Rahmani**, A. Babakhani, "A fully integrated electromagnetic energy harvesting circuit with an on-chip antenna for biomedical implants in 180 nm SOI CMOS," *IEEE SENSORS*, 2016.

CHAPTER 1

Introduction

1.1 Motivation

Wireless System-on-Chip (SoC) devices are becoming increasingly popular nowadays and are utilized in a broad range of applications. In particular, medical implants and Internet-of-Things (IoT) can be considered as two dominant sectors that are enables based on the development of robust and reliable SoCs. Fig. 1.1 shows some examples of various applications of wireless SoCs in the medical and IoT domain. Nowadays, wireless SoCs are used for different medical purposes such as cardiac pacemakers, neural recording and stimulation systems, targeted drug delivery, and even as a wireless pill. On the other hand, wireless SoCs have been proposed for many IoT applications such as wearable electronics, supply chain management, machine motorizing, and Unmanned Aerial Vehicles (UAV). Despite the different nature of these application domains, they jointly demand some mutual systematic features form an SoC. Wireless operation, low-power consumption, low-cost SoC, and a compact form-factor are the imperative requirements of a robust SoC that is practical for the wide range of applications.

The main pillars of the next-generation sensing systems are based on sustainable power delivery, low-power connectivity, efficient processing algorithms, and ubiquitous sensing. Hence, the block diagram of a typical SoC can be viewed as Fig. 1.2. As illustrated, the SoC is equipped with power modules or energy harvesting sub-system, a sensing platform, an analog front-end for amplifying the signal, Analog-to-Digital (ADC) converter, and a

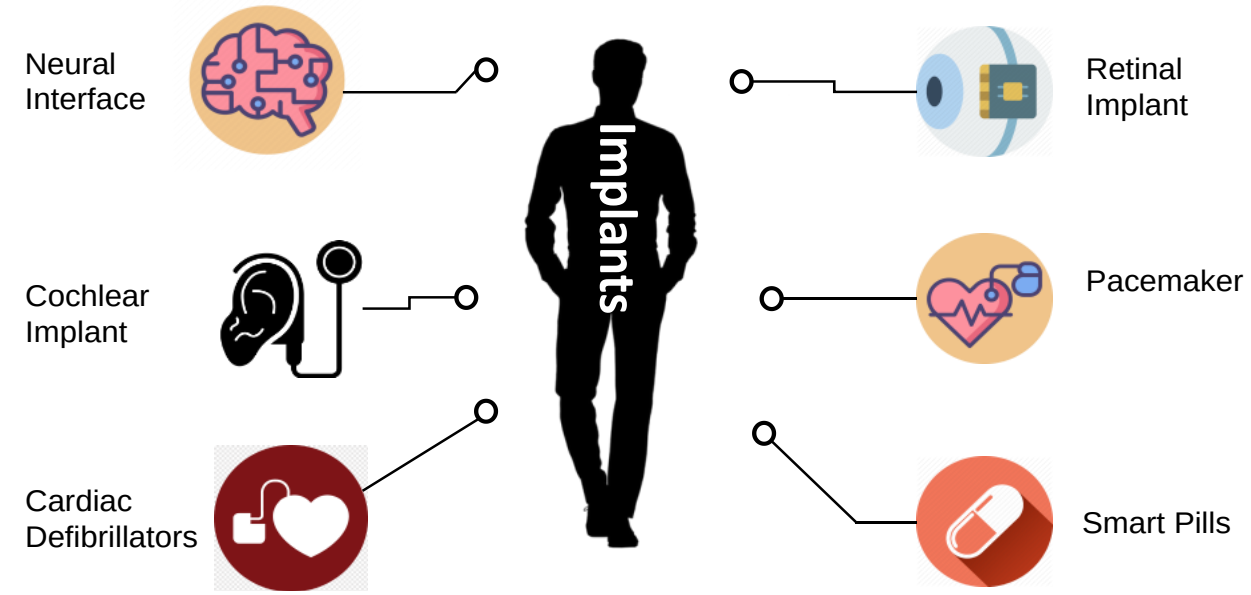

(a) Implantable SoCs in modern medicine.

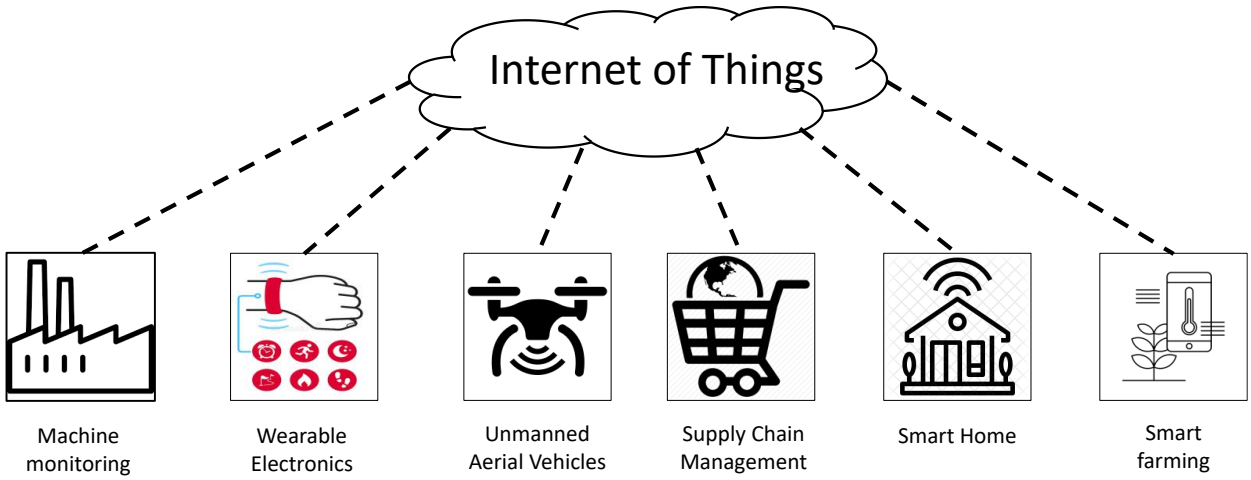

(b) Various applications of wireless SoCs for IoT.

Figure 1.1. Application examples of wireless system-on-chip devices.

data telemetry sub-system. The main challenge in the development of future SoCs reveals itself when a small form-factor is considered as one of the crucial criteria in the design process.

Miniaturization is one of the key requirements of next-generation wireless systems since

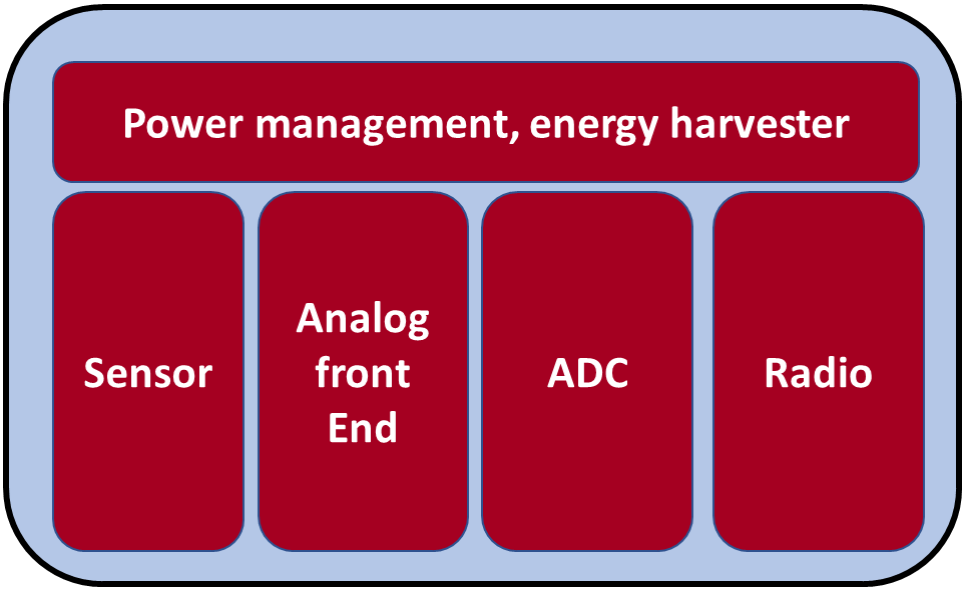

Figure 1.2. The building blocks of a typical wireless SoC.

it leads to unprecedented benefits both medical implants and IoT systems. in particular, a mm-sized form-factor results in the following advantages for implantable devices:

1. Higher sensor density
2. Improvement of Spatio-temporal resolution
3. Ultra-small recording scale
4. Minimal tissue damage and ease of encapsulation
5. Ease of implantation procedure

Miniaturization introduces a new set of challenges for implementation of the aforementioned pillars of future sensing systems. The available power budget scales with the form-factor that limits the functionality of a system and necessitates extensive power reduction techniques. In addition, due to the limited energy storage density of charge accumulation components such as capacitors, the stored energy within a small form-factor

becomes excessively difficult. data communication also faces serious challenges as the overall size of the system reduces. Electrically small antennas show poor radiation efficiency at lower frequencies and tend to be operated at the GHz frequency region. However, as the frequency increases, the propagation path loss becomes significantly large and causes the communication system to have a short-range operating range.

1.2 Dissertation Overview

In this dissertation, we propose integrated wirelessly powered solutions for tackling the challenges towards next-generation medical implants and IoT devices. First I discuss wireless power delivery options and techniques, and propose fully integrated power receiving systems both for near-field and far-field operating regions. Next, I build upon the proposed power harvesting system and introduce a fully integrated wirelessly powered radio for high-performance implants such as neural interface systems. Then, I present a coherent power combining technique for alleviating the high-path-loss problem in Wireless Sensor Networks (WSN) to improve the received Signal-to-noise (SNR) ratio and enable localization purposes. Finally, I discuss the potentials of a machine-learning-assisted sensing system for low-power and low-complexity SoCs and demonstrate how they can pave the way for smart sensing.

In Chapter 2, I present a dual-mode power harvesting system for millimeter-sized biomedical implants that is immune to the variation of wireless link parameters and loading. The design includes a multi-stage full-wave voltage rectifier, a power management unit, and a low dropout voltage regulator. Depending on the received RF power level, and the required power by the load, power delivery is conducted in continuous or duty-cycled mode. The system is fabricated in 180-nm Silicon On Insulator (SOI) CMOS technology with an active area of 2.56 mm^2 including an on-chip coil. RF power is transferred to the chip from a 2×2 cm^2 coil through 10 mm of air at 434 MHz. The efficiency of the designed

wireless link, which is the power transfer efficiency from the external coil to the on-chip coil, reaches up to 0.68 % (-21.7 dB) at 10 mm separation through the air. Keeping the transmitted RF power below 24 dBm, the system can provide a 1.08 V dc voltage for resistive loads larger than 20 kΩ continuously over time. When the harvested power is not enough to drive the load continuously, the system operates in duty-cycled mode. Measurement results show that the system can drive a 1kΩ load in the duty-cycled mode when the transmitted power level is 15 dBm.

Chapter 3 presents a fully integrated, wireless, RF-powered data transceiver for high-performance implants such as neural interfaces. The design occupies a total volume of 1.6 mm^3 with no need for an off-chip component. The integrated circuit (IC) receives power and downlink data with amplitude-shift-keying (ASK) modulation by an on-chip coil through an RF wireless link with an efficiency of -22.6 dB at 250 MHz. For uplink data transmission, we propose a transmitter (TX) based on a power oscillator stage directly connected to an on-chip dipole antenna that supports various data rates with both on-off-keying (OOK) and ultra-wideband (UWB) schemes. The design includes a power receiver system that enables the IC to operate under various power budgets by adjusting the duty cycle of the TX. With a 25 dBm power transmitter at a 1-cm distance, the RX achieves a maximum data rate to 2.5 Mbps with a power consumption of 2.6 μW. Also, the TX supports data rates of up to 150 Mbps with UWB modulation with a 15-cm operating range achieving energy efficiency of 4.7 pJ/b. This work improves RX and TX energy efficiencies by $\times 50$ and $\times 2.3$, respectively.

In Chapter 4, I discuss the opportunities offered by mm-sized integrated chips for IoT applications. In particular, I propose a novel technique to synchronize a swarm of sensor nodes at the RF domain and produce coherent radiation from the sensor nodes to increase the amplitude of the reflected signal. A network is formed by an array of microchips that are wirelessly powered, and upon activation, radiate back an RF signal. The phase of the radiated signals from each microchip is synchronized using a wireless reference signal. This technique results in a coherent amplitude combing and power amplification. The microchips

are fabricated in a 180-nm CMOS SOI technology. Each microchip occupies a total area of $3.9 \times 0.7\ mm^2$ that includes three on-chip dipole antennas that are used for power delivery, injection locking, and back RF reflection. Measurement results reveal that a reference signal in a frequency range of 7.72-7.79 GHz can successfully synchronize the reflected signals radiated from the microchips through a sub-harmonic injection locking scheme. A wireless reference signal of 7.733 GHz synchronizes an array of 2 × 2 microchips. The microchips are locked to half of the reference frequency and produce coherent radiation at 3.866 GHz. This scheme results in a power elevation of ∼12 dB on the reader's side.

I also present a fully integrated battery-less RFID tag that is fabricated in 180nm CMOS technology for localization and biomedical applications. The design is composed of a rectenna, a power management unit, a data receiver used for clock recovery, and a UWB transmitter. Power and clock signals are transferred to the tag through an inductive link at 250 MHz that is AKS-modulated with a square wave with a frequency of up to 2 MHz. The proposed tag can be used as a transponder to transmit back short pulses with a width of 50 ns when placed in proximity of a reader. Measured results show that the tag can also be used for communication purposes and communicate a sequence of digital data to a reader. The whole chip size including a loop antenna for power and clock recovery and a dipole antenna for the UWB transmitter is $2.4 \times 2.3\ mm^2$.

Chapter 5 concludes this dissertation by summarizing the key contributions and picturing the road-map of future miniaturized wireless SoCs.

CHAPTER 2

Wireless Power Transfer Systems for Millimeter-Sized Systems

2.1 Introduction

The first step toward a high-performance wireless SoC is to design a reliable powering method that is compatible with the requirements of next-generation sensing systems. Currently, wireless SoCs rely on batteries or inductive coupling for powering and few examples of commercial SoCs for medical applications and Internet of Things (IoT) is illustrated in Fig. 2.2. Due to the limitation of battery techology, battery-powered devices cannot be miniaturized below some certain limits. As a result, the overall for-factor, life-time, and cost of a battery powered system is not compatible with the specs of next-generation SoCs. On the other hand, commercial wirelessly powered devices based on inductive coupling utilize a pair of centimeter-sized coils and operate at low-MHz frequency ranges. Therefore, the integration capability of such systems is also limited by the coil sized that makes them impractical to address the form-factor requirements of future SoCs.

As a remedy to aforementioned problems associated with conventional powering techniques, researchers have explored alternative energy sources to enable a sustainable and compact powering method. Different powering techniques can be categorized based on their need to an external energy source for establishing the power link to an SoC as shown in Fig. **??**. Ambient energy sources that are present in the environment are labeled as intrinsic energy sources and few examples of them can be named as bio-fules,

Figure 2.1. Commercial wireless SoC examples.

thermo-electric, and body motion. Although intrinsic sources seem very attractive for powering wireless SoCs, they fail to provide sufficient power densities and cannot be used for high-performance devices. On the other hand, the powering methods that utilize an external power transmitter render in high power densities. Wireless power transmission systems based on electroomagnetic waves, ultrasonic, and light have been demonstrated as a promising approach for delivering milli-Watts of power mm-sized systems [2]. In particular, wireles power transfer systems based on electromagnetic waves are very interesting for mm-sized SoCs since they can jointly address the requirements of medical implants and IoT devices. A wireless power transfer system operating in near-field electromagnetic region is suitable for short-range distances and provides high power densities and is applicable to medical implants. It worth mentioning that high-frequency electromagnetic waves have also been promising for sensing and spectroscopy applications as well [3–7]. Electromagnetic waves can be also focused in a narrow beam-width to enable long-range power delivery with low power densities and fulfill the requirements of an IoT device. Therefore, power transfer systems based on electromagnetic waves are explored in this thesis.

Evolution of implantable devices (IMD) has opened a new gate toward finding new diagnosis and treatment methods in the modern medicine. Due to the clinical constraints, a practical implant should operate without any transcutaneous wire connection, which

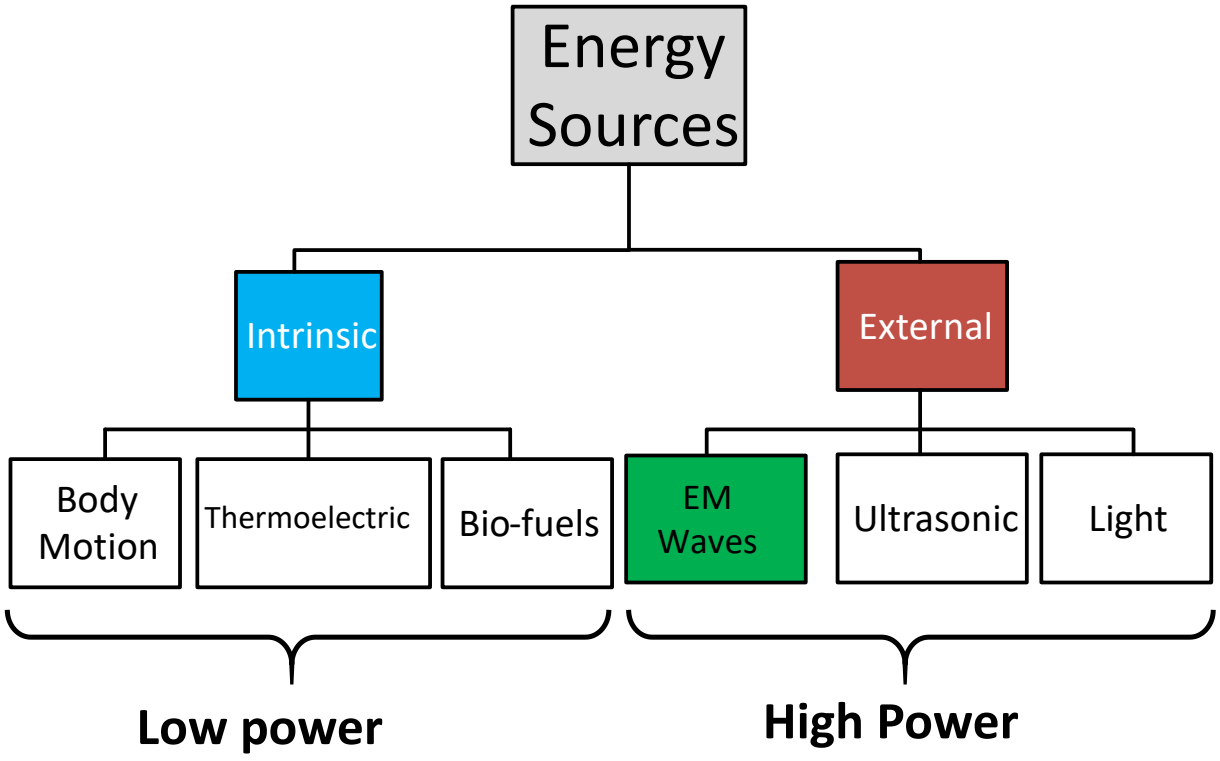

Figure 2.2. Classification of powering techniques based on the power density.

raises serious challenges for powering an IMD. Therefore, development of a robust wireless power harvesting system is the key step toward building a high-performance implant that can be used for clinical purposes. On the other hand, emerging applications of IMDs, such as Brain Machine Interface (BMI) demand biological signal acquisition with a high data rate and a high spatial resolution. For instance, research on the anatomical, physiological, and computational bases of speech production has made important strides in recent years but has been limited by a glaring lack of information on the dynamics of the speech production process. This is a methodological limitation related with the low spatio-temporal resolution of widely available tools such as fMRI, EEG, behavioral, and stroke lesion based approaches [8–10]. Miniaturizing the size of an IMD is the solution for improving the spatio-temporal resolution of the recorded signals since it leads to a higher

sensor density and enables signal recording at an ultra-small structural scale. In addition, smaller implants cause less damage to the living tissues, ease up the encapsulation process, and are easier to be implanted [11–13].

With recent advances in integrated semiconductor technology, the size of a wirelessly powered IMD is dominantly controlled by the dimensions of power harvesting modules. Miniaturizing the size of receiving coil be integrated with the required circuitry leads to the total system area reduction. In addition, the receiving coil can be integrated with rest of the required circuitry on the same CMOS chip, which significantly reduces the total cost of the system, improves reliability, and eliminates the need of post-fabrication processes. Most of the traditional wireless power transfer (WPT) techniques are based on inductive coupling between two cm-sized coils and operate at low-MHz or sub-MHz frequency range [14–16]. Bulky receiving coil of these systems is fabricated on a separate substrate and is attached to rest of the system by bond wires. Although these systems achieve a high value of power transfer efficiency through two coils, the large form-factor of the Rx coil makes them impractical for powering small IMDs. Increasing the RF carrier frequency makes it possible to shrink the size of a receiving coil to millimeter-scale. As the carrier frequency increases, the rate of changes in the incident magnetic flux on the receiving coil raises, which results in boosting the induced voltage [17, 18]. In addition, the Q-factor of small coils increases at higher frequencies [19, 20]. Although shrinking the size of a receiving coil degrades the power transfer efficiency, there has been a lot of efforts to develop a mm-sized power harvesting system to benefit from the advantages of miniaturization [19–28].

The functionality of an IMD is dominantly determined by the available power. Therefore, delivering the maximum power is one the most important goals in the design process. A practical power harvesting system requires additional circuitry for converting captured sinusoidal signals to a dc voltage. The additional circuitry represents other sources of power loss in the system. The overall Power Transfer Efficiency (PTE) is defined as the

delivered power to load of the power harvesting system (P_{load}) over available power by the generator (P_G) as defined in (2.1).

$$PTE = \frac{P_{load}}{P_G} = \eta_{link} \times \eta_{RF-DC} \tag{2.1}$$

$$\eta_{RF-DC} = \eta_{rec} \times \eta_{reg} \tag{2.2}$$

The PTE can be viewed as multiplication of wireless link efficiency (η_{link}) and RF to dc conversion efficiency (η_{RF-DC}). Voltage rectifier and regulator are the most important circuitry required for RF to dc conversion. Therefore, η_{RF-DC} can be considered as multiplication of rectifier efficiency (η_{rec}) and regulator efficiency (η_{reg}). All terms in (2.1) and (2.2) are defined later in the rest of this paper.

Intervening biological tissues show an absorptive behavior toward electromagnetic waves, which becomes worse at higher frequencies [29]. The tissue absorption makes the wireless power delivery to a mm-sized implant very challenging since the amount of transmitted power should be kept below a certain threshold that is defined by safety standards. Moreover, the amount of received power at the Rx side is very sensitive to the composition of the intervening biological medium, alignment of the coils, and the separating distance [30, 31]. In addition to the challenges that are related to the wireless link, non-linear behavior of the required circuitry for RF to DC conversion and the load variation of a power harvesting system greatly impact the amount of harvested dc power and changes the available power for an implant.

In this work, we present a mm-sized power harvesting system to address the challenges of wireless power transmission to small implants that stem from the variation of wireless link parameters and varying power consumption of an IMD. In this paper, we analyze the effect of system level parameters such as type and thickness of intervening tissues on the performance of a WPT system and provide a design procedure for optimal design of a

mm-sized on-chip coil for miniaturized implants. We also introduce a power management technique that enables the system to drive a wide range of loads.

This paper is an extension of [32] and explains the design procedure of the power harvesting system in more details. It includes more extensive simulation results and provides updated measurement results for characterizing the performance of the fabricated chip. The remainder of this paper is organized as follows. Section 2 gives an overview of a WPT system and analyzes the effect of wireless link parameter. The design procedure for the on-chip coil and the Tx coil is discussed in this part. Section 3 describes the design of a multi-stage voltage rectifier and shows how the characteristics of the voltage rectifier are affected by the operating frequency and the available RF power level. Circuit schematics and system architectures of the power management unit and the voltage regulator are described in Section 4. The performance of the power harvesting system is characterized in Section 5, which is followed by the conclusion in Section 6.

2.2 Wireless Link: Design and Analysis

2.2.1 Wireless Link Modeling

Traditional WPT systems for implantable devices use a pair of coils to inductively couple the energy from a primary coil outside the body to a secondary coil that is implanted. The operating frequency of these systems range from hundreds of kHz to few MHz and the size of Rx coil is in the order of few centimeters. Inductive near-filed systems that operate at hundreds of kHz or few MHz can achieve a very high link efficiency. Inductive coupling between two coils can be governed by Faraday's induction law and is proportional to the area of coils. Typically, link efficiency in these systems improves by using larger coils and increasing the number of turns. Traditional analysis methods for a WPT system that are mainly based on coupled mode theory may not be applicable to a system that operates at a relatively high frequency due to the following reasons: First, as the operating frequency

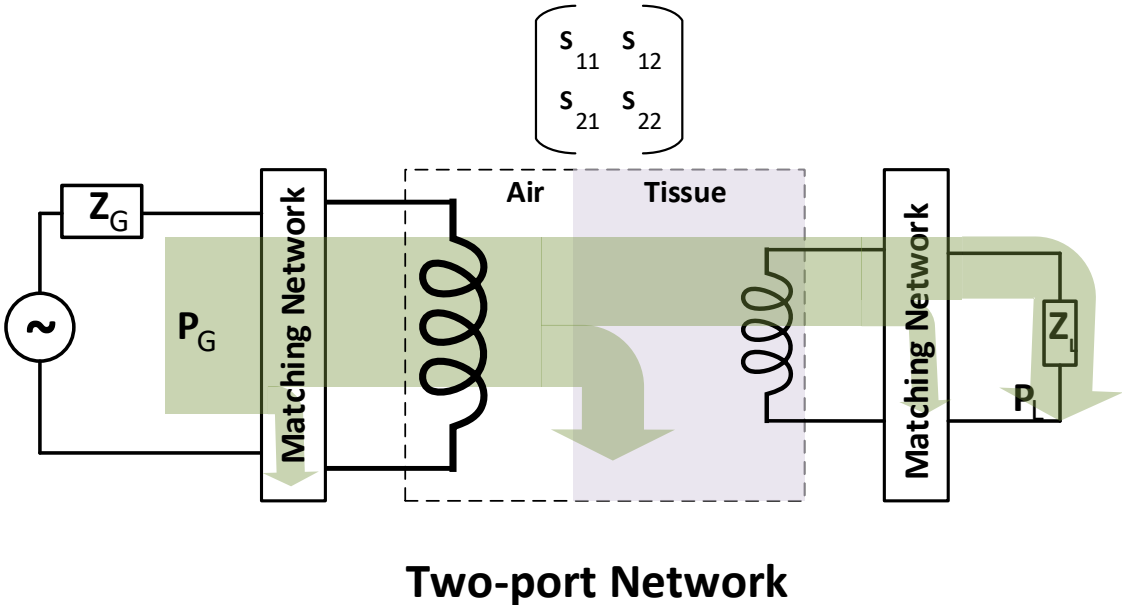

Figure 2.3. Power flow in the wireless link of WPT system.

increases, the wavelength of the electromagnetic waves become comparable to the dimension of the coils and separating distance. In this case, electromagnetic waves contain radiative fields and include both radiative and non-radiative components. A simple near-field inductive model for WPT systems only governs non-radiative fields and fails to address the effect of radiative components. Second, most of the traditional models assume that power transfer through tissue is almost same as energy transfer through the air since tissues are transparent to magnetic fields. This assumption is not valid in MHz frequency range and above since biological tissues pose significant issues on propagating of electromagnetic fields and greatly attenuate electric field. Therefore, unlike traditional analysis methods, intervening tissues cannot be ignored since they have a significant effect on link efficiency and the PTE.

Fig. 2.3 shows the power flow in a wireless link of a WPT system that utilizes RF electromagnetic waves for power transmission through biological tissues. The link efficiency can be defined as the ratio of the delivered power to load of the two-port network over the generated power by the RF source and can be divided into three distinguished terms as:

$$\eta_{link} = \frac{P_L}{P_G} = \eta_{m,Tx} \times \eta_{2port} \times \eta_{m,Rx} \tag{2.3}$$

The η_{2port} term contains power losses in the coils and the intervening medium while the $\eta_{m,Tx}$ and the $\eta_{m,Rx}$ represent the power losses due to impedance mismatch at the Tx and Rx sides, respectively. We have used a two-port network model for studying the wireless link. A two-port network approach can be utilized to calculate the η_{link} and other characteristics of the wireless link at any frequency. In addition, this approach is independent of the geometry of coils and composition of intervening medium between transmit (Tx) and receive (Rx) coils. Therefore, two-port network method is a general analysis method, which is independent of electromagnetic operating region (near-field or far-field). Characteristics of a two-port network can be fully described by its impedance parameters (Z-parameters) or Scattering parameters (S-parameters). However, extracting Z-parameters of a two-port network at high frequencies may be challenging or even impossible. On the other hand, S-parameters can be calculated at any frequency. Moreover, the S-parameters of a network can be converted to Z-parameters.

The S-parameters of the two-port network in Fig. 2.3 are determined by dimension and structure of the coils as well as the type and thickness of intervening medium. Therefore, the η_{2port} is an intrinsic characteristic of the wireless link. The most important step toward optimization of the wireless link is maximizing the η_{2port} since the impedance mismatch can be almost eliminated by using proper matching networks. Assuming the impedance of the generator (Z_G) is equal to the reference impedance (Z_0), the η_{2port} can be formulated based on the S-parameters of the network according to the following equations [33].

$$\eta_{2port}(f) = \frac{|s_{21}(f)|^2}{(1 - |\Gamma_{in}(f)|^2)(1 - |s_{22}(f)|^2)} \tag{2.4}$$

where

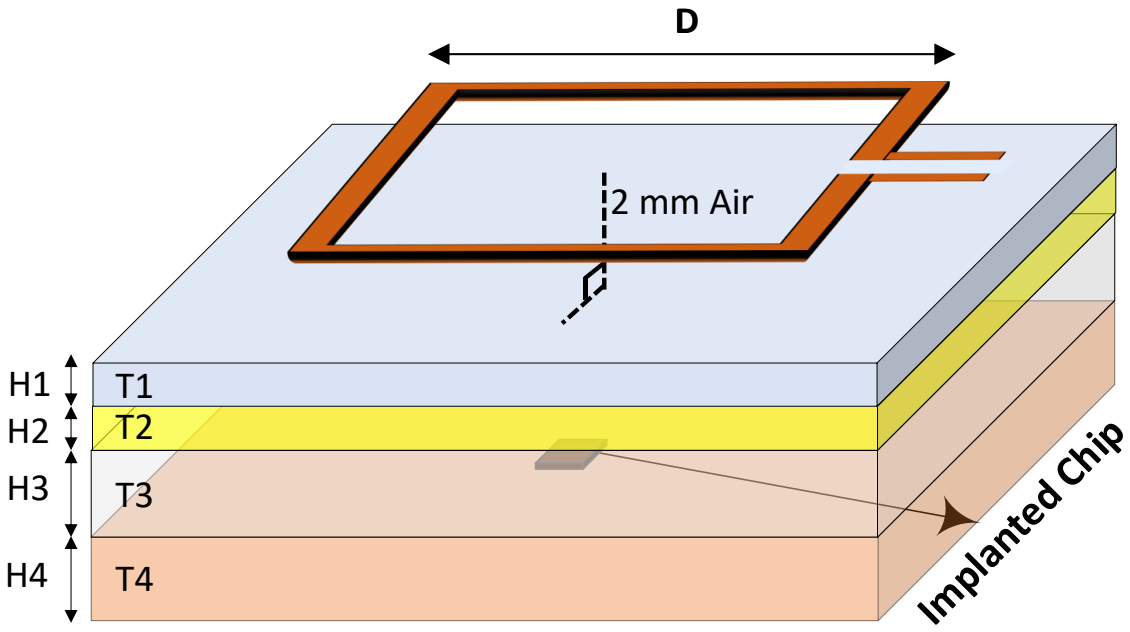

Figure 2.4. Configuration of the WPT system with a multi-layer model for intervening biological tissues.

$$\Gamma_{in}(f) = s_{11}(f) + \frac{s_{12}(f)s_{21}(f)\Gamma_L}{1 - s_{22}(f)\Gamma_L} \tag{2.5}$$

$$\Gamma_L = \frac{Z_L - Z_0}{Z_L + Z_0} \tag{2.6}$$

Equations (2.4)-(2.6) imply that the η_{2port} is also affected by the load. However, since the system is weakly coupled and the values of s_{12} and s_{21} are very small, variation of Z_L does not show a significant effect on the η_{2port}. In a two-port network system, different parameters are can be used based on the S-parameter to capture the impedance mismatch effect on TX and RX sides. The derivation of different power efficiency parameters is explained in Appendix A.

A conceptual model of a WPT system for IMDs is illustrated in Fig. 2.4. RF energy is transferred from an external coil to a mm-sized Rx coil that is integrated on a silicon chip and implanted in the human body. The intervening media between the coils is composed

of a 2 mm air gap and 11 mm of biological media. These values represent a reasonable estimation of the separating distance between the coils in most of IMD applications. In this model, intervening tissues are modeled by separated planar layers stacked on top of each other. The variables T_1, T_2, T_3, and T_4 in the WPT system model represent the type of each layer and H_1, H_2, H_3, and H_4 represent the thickness of corresponding layers. By choosing proper type and thickness for the planar layers, different human organs can be represented by this model. For instance, tissue composition in the human head and chest can be modeled by setting the variables in Fig. 2.4 according to Table 2.1.

Table 2.1

LAYER PROPERTIES FOR MODELING HUMAN HEAD AND CHEST

Variables	Head	Chest
T_1-H_1	Skin-2mm	Skin-3mm
T_2-H_2	Fat-2mm	Fat-3mm
T_3-H_3	Bone-7mm	Muscle-4mm
T_4-H_4	Dura-inf	Muscle-inf

Biological tissues can be modeled as a low-loss dielectric material with a complex dielectric constant. In addition, biological tissues show a frequency-dependent behavior toward electromagnetic waves. Hence, the complex dielectric constant is also a function of frequency and can be divided into a real part that represents electrical permittivity and an imaginary part that corresponds to electrical conductivity of the material as is written below:

$$\epsilon(f) = \epsilon_0\epsilon_1(f) + i\epsilon_2(f) = \epsilon'(f) + i\frac{\sigma(f)}{2\pi f} \tag{2.7}$$

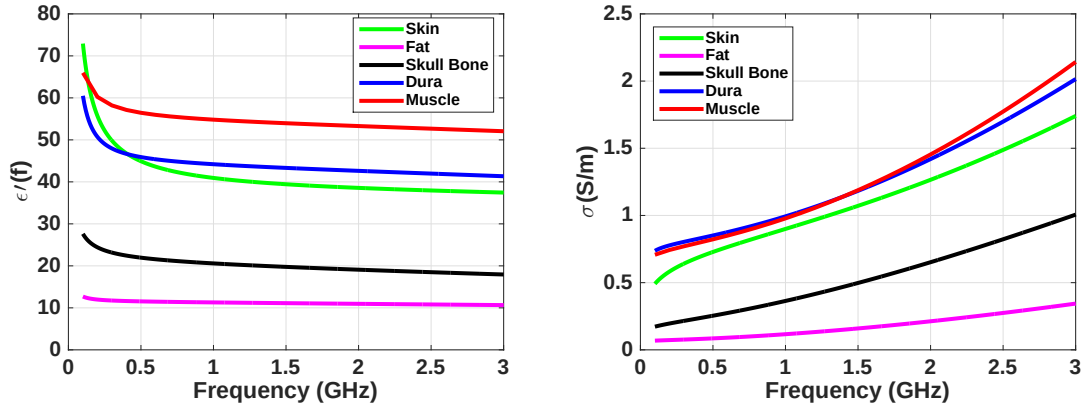

(a) (b)

Figure 2.5. Dielectric constant of different biological tissues. (a) Permitivitty (b) Conductivity.

In order to capture the frequency-dependent behavior of tissues into the planar model, we have used a cole-cole formula that provides a curve fitting method to formulate the complex dielectric constant of the evaluated layers in Table 2.1. Following the described approach in [34] leads to extracting the value of dielectric constant for a particular type of tissue. Permittivity and conductivity of the constituent tissues in Table 2.1 are plotted Fig. 2.5(a) and Fig. 2.5(b), respectively.

2.2.2 Coil Optimal Design

As it was described, the S-parameters of the two-port network is determined by the dimension of the coils and composition of the intervening media. Therefore, the η_{2port} can be enhanced by optimizing the Tx and Rx coils. For a near-field WPT system, extracted S-parameters can be used to represent a transformer model that is described by a primary coil, secondary coil, and mutual inductance between the coils. It has been shown that the maximum efficiency of an inductive wireless link can be formulated as [35]:

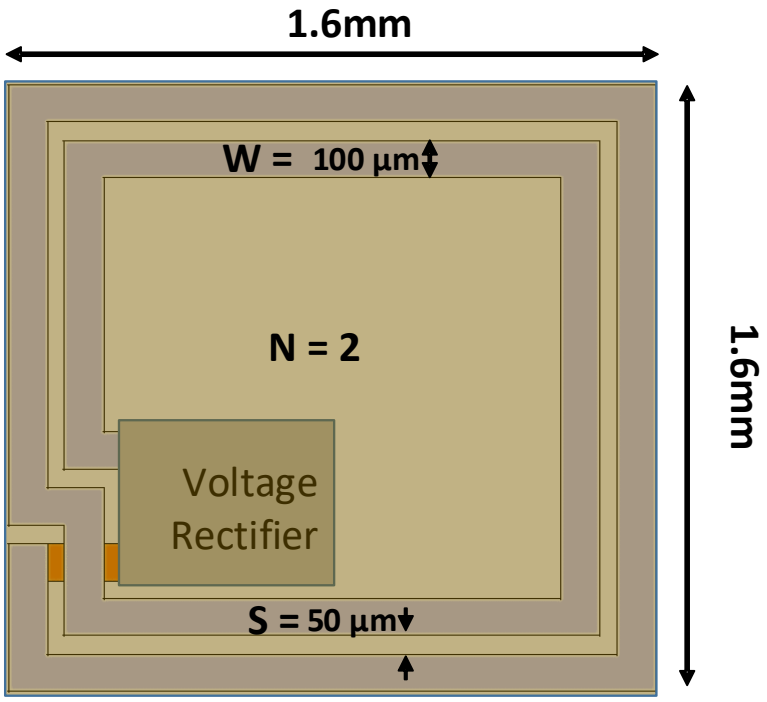

Figure 2.6. Detailed view of the on-chip coil. The picture is not drawn in scale.

$$\eta_{link,max} = \frac{k^2 Q_1 Q_2}{(1+\sqrt{1+k^2 Q_1 Q_2})^2} \tag{2.8}$$

Where Q_1 and Q_2 represent the quality factor of primary and secondary coils, respectively and k stands for the coupling coefficient between two coils. Optimal coils for WPT systems through air usually, have a high number of turns since the Q-factor of coils is believed to increase as a function of turn numbers. On the other hand, biological tissues at high frequencies have a relatively high electrical conductivity. The proximity to a lossy dielectric medium represents parasitic capacitive and resistive components and degrades the Q-factor of the coils. Although increasing the number of turns increases the self-inductance of a coil, it also results in higher parasitic components, which have a negative impact on the η_{link}. Therefore, the optimal number of turns for implantable coils is expected to be less than four [35, 36]. The effect of surrounding environment should be

considered in optimization process and an optimal design for a specific environment may not be optimal for a different environment. Multiple optimization methods have been proposed in the literature for improving the η_{link} [35–38]. Most of these methods follow an iterative method for link optimization that changes the parameters of Tx and Rx coils to improve the η_{link}. We have also utilized an iterative algorithm for coil design optimization. The main objective of the optimization algorithm is to find the combination of design variables that result in the maximum possible value of η_{2port}. The main design variables that are optimized are the maximum outer dimension of the Tx coil (D), number of turns in Rx coil (N), trace width of Rx coil (W), and spacing between the traces (S). Ideally, turn numbers, trace width, and trace spacing of the Tx coil should also be considered as other variables in the optimization process. However, adding all of these variables greatly expands the design space and imposes a huge EM simulation overhead. Therefore, we have assumed a single turn Tx coil with a trace width of 0.2 mm. The optimization method that is used in this work is described below:

- Step 1: Applying design constraints that are imposed by the application requirements such as available area and distance between the coils.
- Step 2: Initializing design variables of Rx coil such as number of turns (N), trace width (W), and spacing (S).
- Step 3: Detecting the optimum size of the Tx coil that maximizes the η_{2port}.
- Step 4: Modifying design variables of the Rx coil to optimize η_{2port}.
- Step 5: Following step 3 to step 4 until changing design parameters does not result in any improvement.

The main constraints in the design process are imposed by the requirements of a particular application. One of the main goals of this work is to shrink the size to mm-scale. Among

different implantable application, neural recording and stimulation devices have the most restricted area limitations. Therefore, we have optimized the design for neural recording implants and assumed that the maximum size of the Rx coil is 1.6 mm, which is a reasonable size for a neural implant. It has been shown that the optimal dimension of a Tx coil for wireless power transmission to a mm-sized coil that is located at distance d is bounded to a specific limit that is written in [35]:

$$D \leq d\sqrt{2(1+\sqrt{5})} \tag{2.9}$$

Considering the application requirements, we have narrowed down our design space by applying the following limits on the design variables:

- 5 mm $\leq D \leq$ 30 mm
- $1 \leq N \leq 4$
- 25 μm $\leq W \leq$ 150 μm
- 12 μm $\leq D \leq$ 100 μm

Following the optimization algorithm over the design space leads to an optimal design for the coils. We have implemented the Rx coil as a two-turn square-shaped loop with the dimensions that are shown in Fig. 2.6. The demonstrated plots in Fig. 2.7 show how the deviation of optimal design variables affect the maximum achievable η_{2port}. It should be noted that each point in Fig . 2.7 reports the maximum value of the η_{2port} that is simulated versus frequency (twenty-one different EM simulations). Due to the dependency of the S-parameters to systematic parameters of the wireless link, the maximum value of the η_{2port} is achieved at different frequencies. As it is evident from Fig.2.7(a), 2 cm is the optimal outer size for the Tx coil and outperforms the other evaluated dimensions. In addition, Fig. 2.7(b) reveals that using more than two turns in the Rx coil degrades the η_{2port}. The effect

of trace width can be clearly seen in Fig. 2.7(c). Although efficiency can be enhanced by widening the traces, it results in more occupied area. Since the Rx coil is integrated on the same silicon chip with rest of building blocks of an IMD, it is desired to keep the occupied area by the Rx coil as low as possible. Therefore, we have avoided using a larger trace width. Finally, the effect of spacing between the traces is depicted in Fig. 2.7(d).

2.2.3 Optimum Operating Frequency

As it was described before, transmitting RF energy at a higher operating frequency increases the rate of magnetic flux change and consequently induces higher voltage at Rx side. However, as the frequency increases, more power is dissipated in the intervening biological tissues. This phenomenon implies that there is an optimal operating frequency for wireless power transmission through biological tissues. We define the optimum frequency as the frequency that maximizes the η_{2port} of a WPT system.

$$f_{opt} = \arg\max_{f} \eta_{2port}(f) \tag{2.10}$$

Ideally, the optimum frequency should be the frequency that maximizes the PTE in (2.1). Reference [39] has proposed an equation-based optimization method for inductive WPT systems that includes the frequency-dependent behavior of a voltage rectifier in the optimization process. The authors have decoupled the optimization process of Tx and Rx coils assuming that the 0.01 mm^2 Rx coil is exposed to a uniform magnetic field. This assumption greatly simplifies the optimization process since it eliminates the need for an iterative optimization algorithm. Although the proposed optimization method is very insightful, the uniform magnetic field assumption does not hold for WPT systems with mm-sized Rx coils and the optimization process of the coils cannot be decoupled from each other [14, 19, 35–38]. Including the frequency-dependent behavior of the voltage rectifier in an iterative method expands the design space and significantly increases the simulation

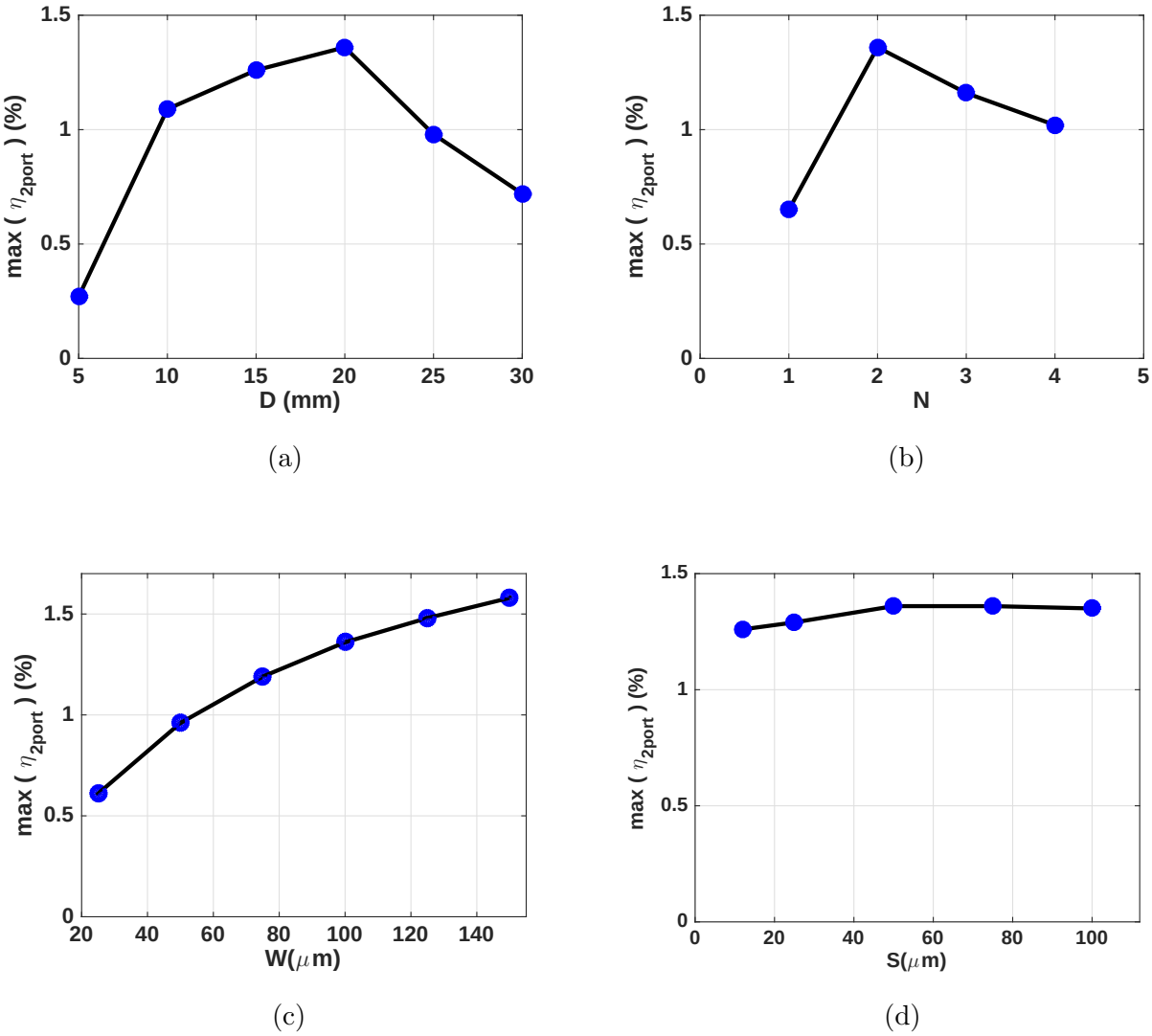

Figure 2.7. Variation of max(η_{2port}) with respect to the following design parameters: (a) Outer dimension of the Tx coil (D) when W = 100μm, N = 2, and S = 50 μm (b) Number of turn in the Rx coil (N) when D = 20 mm, W = 100 μ m , and S = 50 μ m (c) Trace width (W) when D = 20 mm, N = 2, and S = 50 μm (d) Spacing between the traces (S) when D = 20 mm, N = 2, and W = 100 μm .

time. Therefore, the operating frequency is selected based on the link characteristics and a shunt capacitor, which acts like a first-order matching network [40], is inserted between the Rx coil and the rectifier at the operating frequency. Through simulations, we found out that the variation of η_{RF-DC} is much smaller than η_{2port}. Simulation results are presented

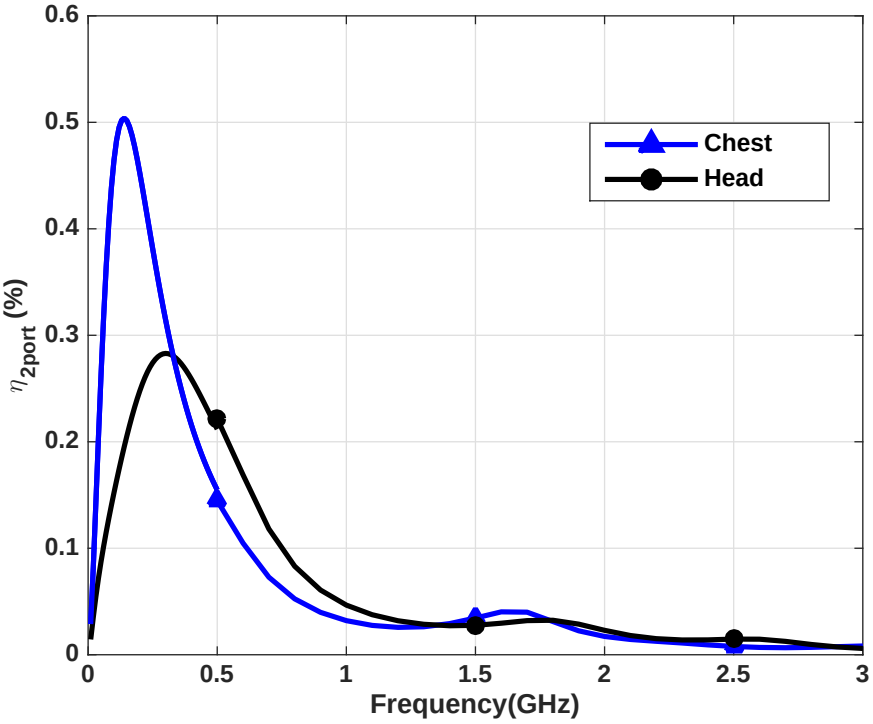

Figure 2.8. Two-port network efficiency of the wireless link with different tissue models considering the effect of parasitic metallic objects in the chip.

in next sections of this paper.

In order to evaluate the effect of tissue composition on η_{2port}, we have used Zeland IE3D simulation tool, which is a 3D Electromagnetic simulator to extract the S-parameters of the wireless link [41]. It should be noted that the metal pieces that are used for implementing the required circuitry degrade the η_{link}. Therefore, we have imported the entire silicon chip metallic objects into IE3D by importing the .gds file of the final layout. Details of the required circuitry and the complete chip micrograph are depicted later in this paper. The η_{2port} is plotted for the human head and chest models in Fig. 2.8. The degradation in η_{2port} peak value can be clearly seen by comparing the simulation results of Fig. 2.7 and Fig. 2.8. The simulation results indicate the f_{opt} and the maximum value of η_{2port} are strongly dependent on tissue composition of the wireless link as the f_{opt} differs by

160 MHz for power transmission through the head and chest layers. In addition, it can be seen that the η_{link} is very sensitive to the operating frequency and deviation from f_{opt} may significantly degrade performance of the system.

The presented simulation results highlight the effect of intervening tissues on the performance of a WPT system and the importance of operating at the f_{opt}. However, the composition and thickness of biological tissues in the human body are not same for all parts and vary depending on the organ. Even for a specific part of the body, the tissue composition differs from person to person based on their gender, race, and age [42]. In addition to tissue variation, the η_{2port} can be greatly degraded by coil misalignment or variation in the separating distance [43, 44], which are inevitable in a real case scenario. The high sensitivity of a WPT system that utilizes a mm-sized coil to the link parameters makes the wireless power delivery to an implant extremely challenging.

2.2.4 Specific Absorption Rate

The long-term exposure to RF and microwave waves has been proven to be very dangerous and raises serious concerns regarding the effects of EM waves on the human body. Specific Absorption Rate (SAR) is a well-known parameter for quantifying energy absorption in biological tissues that is caused by electric fields (E) passing through biological medium. The SAR is defined as the absorbed power per unit of tissue mass according to (2.11) where σ stands for electrical conductivity and ρ represents the mass density of the tissue.

$$SAR(W/Kg) = \frac{\sigma}{2\rho}|E|^2 \tag{2.11}$$

In order to limit the absorption of electromagnetic waves, safety regulations have been proposed by different organizations and nationalities. For instance, the IEEE C95.1-2005 safety standard for the human exposure to electromagnetic fields in the RF and microwave frequency range of 3 kHz to 300 GHz specifies 10 W/kg for the local SAR, and 0.4 W/kg

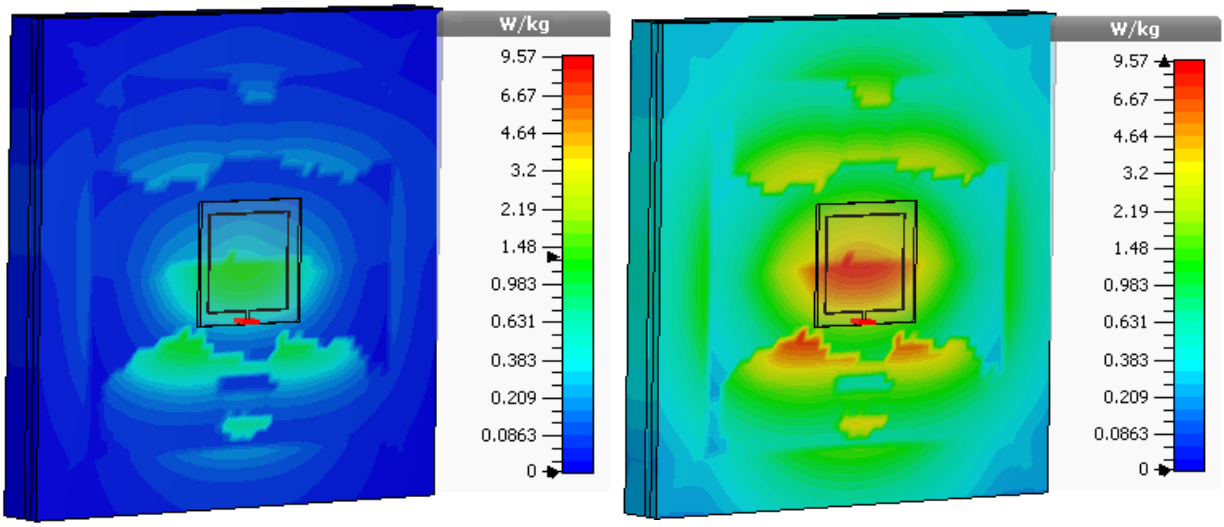

(a) (b)

Figure 2.9. SAR distribution in multi-layer model of the human head averaged over 10 gram of tissue with a reference power of 1W input power. (a) 500 MHz (b) 2 GHz.

for whole body as the maximum allowable absorption while the European Union limits the SAR to 2 W/kg and Federal Communications Commission (FCC) recognizes 1.6 W/kg as the maximum SAR value [45]. We have used Computer Simulation Technology (CST) 3D Electromagnetic simulation tool [46] to calculate SAR values in biological tissues of the human head model in Fig. 2.4. As stated before, the conductivity of the biological tissues increases as a function of frequency, which results in higher absorption. As an example, the SAR distribution in the head model at 500 MHZ and 2 GHz are shown in Fig. 2.9 with a log-scale colormap. The maximum SAR values are calculated based on IEEE C95.3 averaging method over 10 gram of tissue when the 2×2 cm^2 Tx coil is placed 2 mm above the closest layer and the input power to the Tx coil is 1W. Fig. 2.10 shows the maximum SAR value in the head model across frequency with respect to 1 Watt input power to the Tx coil. For a different input power level, these numbers can be scaled to calculate the maximum SAR value. As expected, the SAR value increases at higher frequencies, which limits the maximum deliverable power to the implanted system because the input power to the Tx coil

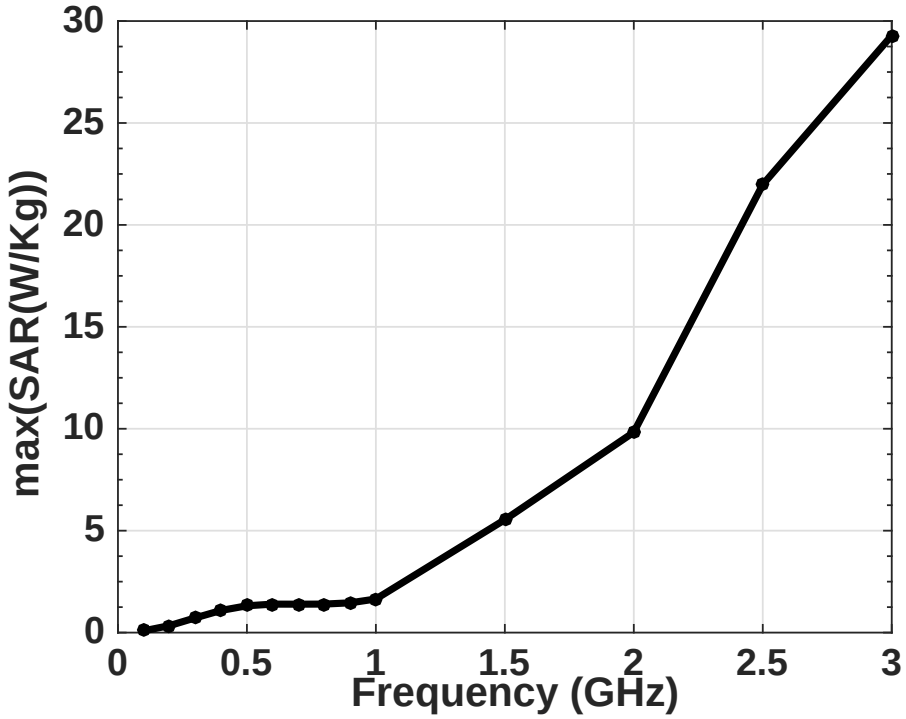

Figure 2.10. Maximum SAR value in multi-planar layer model of human head versus frequency when the input power to the Tx coil is 1W.

should be maintained below a certain threshold level to ensure the safety regulations are not violated. Considering the poor wireless link efficiency, the maximum deliverable power to the implanted chip is limited to few hundreds of micro-Watts when the operating frequency is about hundreds of MHz.

2.3 RF to DC Conversion

2.3.1 Voltage Rectifier

The received electromagnetic power induces a sinusoidal voltage across the Rx coil terminals that cannot be used directly for powering the building blocks of a typical IMD. A common technique to convert received sinusoidal signals to a dc voltage is using voltage

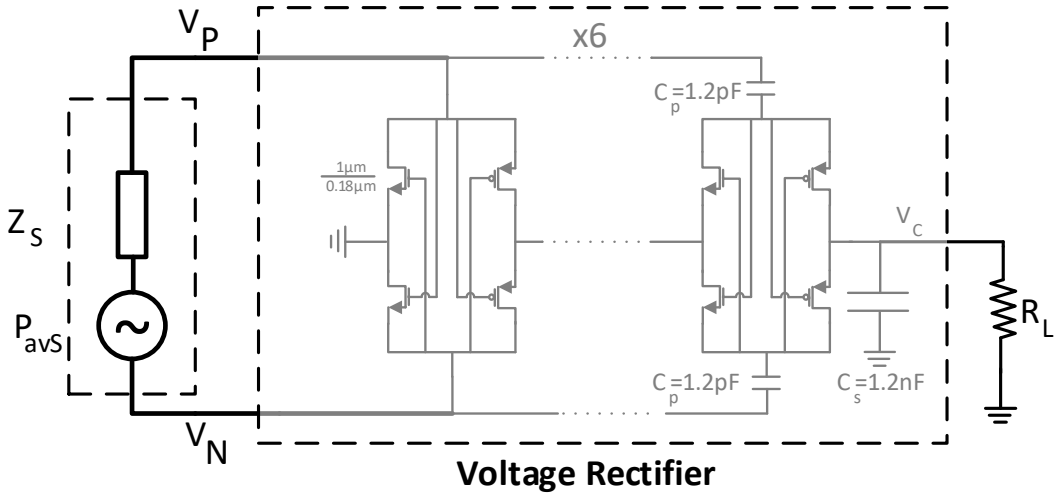

Figure 2.11. Simulation setup for characterizing the voltage rectifier in ADS.

rectifiers. Multiple topologies and techniques for implementing a voltage rectifier have been reported in the literature that provide different sensitivity and conversion efficiency [40, 47–49]. The minimum input power that is required to achieve a specific dc voltage for a particular load is known as the sensitivity of a rectifier while conversion efficiency is defined as the ratio of delivered power to load of a rectifier over the input RF power and is expressed as in (2.12). The tolerance of the power harvesting system to coil misalignment and wireless link parameters depends on the sensitivity of the voltage rectifier. On the other hand, poor conversion efficiency results in less available power for operation of the system. Therefore, it is very important to choose a topology that provides acceptable sensitivity and conversion efficiency. Among different structures, self-driven topology, which is a full-wave rectifier provides a good balance between the sensitivity and the conversion efficiency and is a good choice for mm-sized IMDs.

$$\eta_{rec}(P_{in}, R_L, f) = \frac{P_{DC}}{P_{in}} \tag{2.12}$$

The η_{rec} of a rectifier is a function of operating frequency (f), input RF power to the rectifier (P_{in}), and the dc load (R_L). Rectifiers are generally non-linear circuits and most of

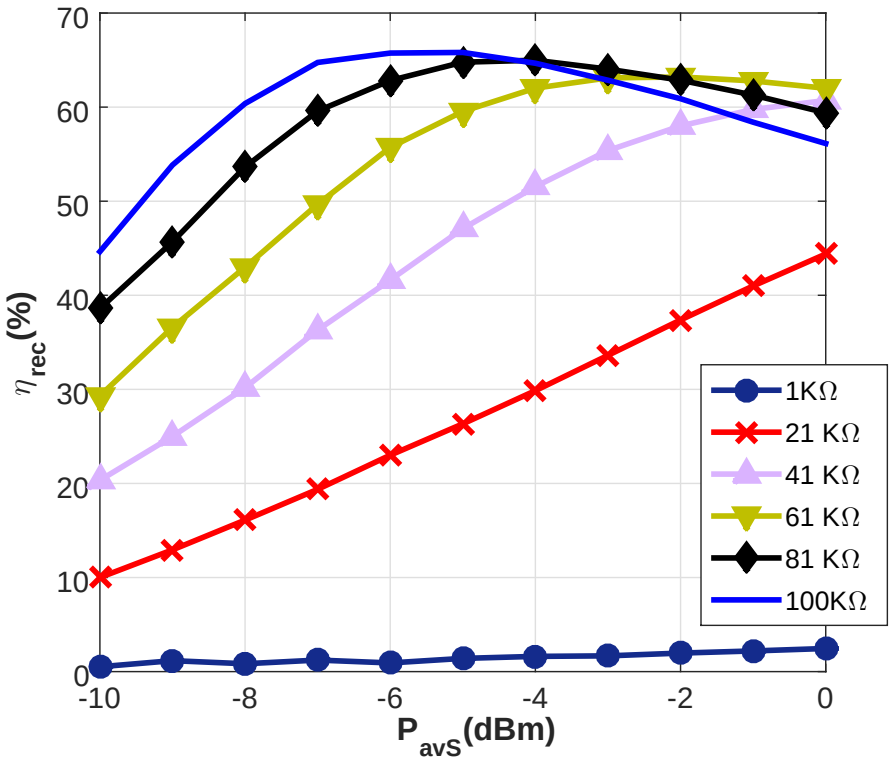

Figure 2.12. Conversion efficiency of the voltage rectifier versus available source power for different resistive loads. Source impedance: 500 Ω, operating frequency: 300 MHz.

their characteristics depend on the input power level [40, 50].

The amplitude of the sinusoidal signal that is captured by the Rx coil is not high enough and varies from tens to hundreds of milli-Volts depending on available power at the Rx side. Hence, a single stage rectifier cannot provide an acceptable dc voltage. However, the voltage level can be enhanced by using multiple cascaded rectifier units at the cost of lower conversion efficiency. The voltage rectifier that is used in this work, is composed of six cascaded stages connected to an on-chip capacitor (C_S = 1.2 nF) that is used to smooth the ripples at the output and store electrical energy. A circuit schematic of the voltage rectifier is shown in Fig. 2.11. All transistors in the rectifier schematic have a width of 1 μm and a length of 180 nm.

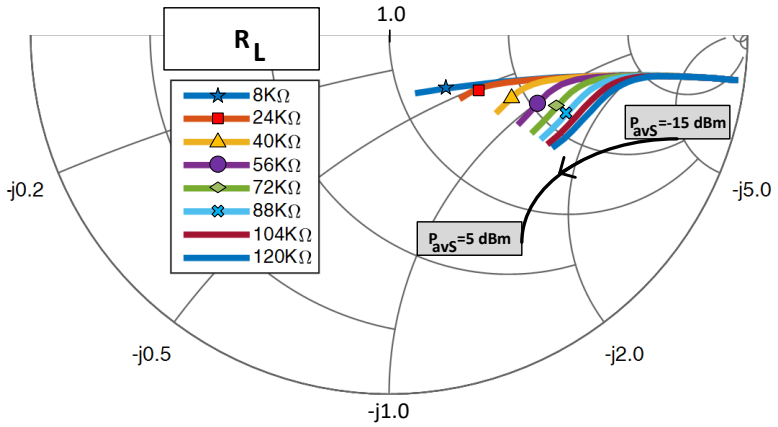

(a)

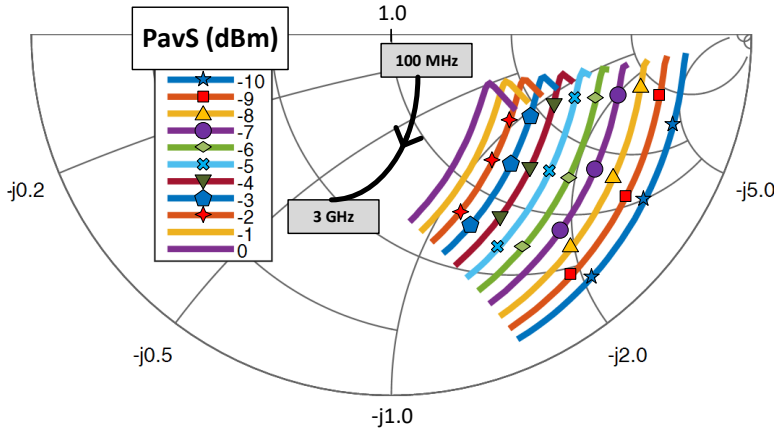

(b)

Figure 2.13. Reflection coefficient between the source ($Z_S = 500\ \Omega$ and $f = 300$ MHz) and the voltage rectifier (a) S_{11} versus P_{avS} for multiple values of R_L (b) S_{11} versus frequency for multiple values of P_{avS}.

Optimizing the η_{rec} is a complex task since it is dependent on the three terms that are shown in (2.12). We have simulated the rectifier with a setup that is shown in Fig. 2.11 in order to evaluate the effect of loading, operating frequency, and input power level on the characteristics of the rectifier. The power source presents a model for the on-chip Rx coil and

the P_{avS} is the available power at the receiving side that is transferred through the wireless link and is captured by the Rx coil. In addition, the operating frequency and the impedance of the power source in Fig. 2.11 are set to 300 MHz and 500 Ω, respectively. These values are obtained by assuming that the chip is implanted in the human head and the Rx coil is resonating with a shunt capacitor. The η_{rec} of the rectifier is simulated for different values of resistive loads (R_L) and is plotted in Fig. 2.12. As expected, the η_{rec} is strongly affected by the variation of P_{avS} and loading. According to Fig. 2.12, when the P_{avS} is low, the voltage rectifier shows a poor η_{rec} due to the fact that the induced voltage across the Rx terminals is not high enough to overcome the threshold voltage of the transistor. As the P_{avS} increases, the amplitude of the induced voltage raises and the rectifier gradually wakes up. However, the minimum required power for activation changes depending on the load size. The η_{rec} improves with P_{avS} increment until the reverse leakage current in the transistors become considerable. At this point, further increment of P_{avS} degrades the η_{rec}. This behavior can be seen for 61 $k\Omega$, 81 $k\Omega$, and 100 $k\Omega$ loads in Fig. 2.12. In addition, Fig. 2.12 also indicates that even for a given P_{avS}, η_{rec} can be optimized by controlling the load size.

Similarly, the input impedance of the voltage rectifier depends on the parameters in (2.12). We have used Keysight Advanced Design System (ADS) to simulate the voltage rectifier and evaluate the effect of operating frequency, input power level, and load size on the input impedance of the rectifier. The impedance value is calculated based on the result of Large Signal Scattering Parameter (LSSP) simulation, which takes the non-linearity of the rectifier into account.

Fig. 2.13(a) shows the variation of reflection coefficient versus P_{avS} for different values of R_L at 300 MHz where the P_{avS} is swept from -15 dBm to 5 dBm for each R_L. Similar to the statement that was made for the η_{rec}, at low input power levels, the rectifier is partially or completely off and it shows huge input impedance values. Therefore, the impedance that is seen by the power source in Fig. 2.11 can be considered as an open circuit.

Operating frequency is another important parameter that affects the input impedance.

The reflection coefficient between the source and the voltage rectifier for different levels of P_{avS} is shown in Fig. 2.13(b) where the frequency is swept from 100 MHz to 3 GHz while $R_L = 8$ kΩ. It should be noted that the impedance of the Rx coil is also a function of frequency. However, the impedance of Rx coil at resonance with an external shunt capacitor has a small variation over the frequency range of interest. Therefore, the value of source impedance has been set to 500Ω. According to this plot, the amount of reflected power is dominantly controlled by the input power level and is not impacted significantly with small variation of frequency. Therefore, the impedance mismatch between the Rx coil and the voltage rectifier is mainly dependent on the P_{avS}.

Impedance matching between the rectifier and the two-port network is necessary to maximize the delivered power to the implant and eliminate power reflection. As it was discussed in the last section, any variation in wireless link composition impact the η_{link} and f_{opt} , and consequently changes the P_{avS}. On the other hand, the impedance of the voltage rectifier is very sensitive to the P_{avS} as it is indicated in Fig. 2.13. Therefore, a practical matching network should be able to change the values of constituent components adaptively, which requires a processing unit for dynamic calibration. However, implementing a dynamic matching network requires additional circuitry for measuring the impedance of the network and the rectifier [26, 51–53]. Adding such a dynamic calibrator to the system imposes power and area overhead in the design while the improvement of η_{link} does not necessarily overweight the additional power consumption. Hence, instead of including an adaptive matching network in the design, we have decided to match the on-chip coil and the voltage rectifier by inserting a shunt capacitor between them. The terminals of the coil that are presented as V_P and V_N in Fig. 2.11 are available via two bond-pads on the chip. Depending on the characteristics of the wireless link and the f_{opt}, a proper matching capacitor is connected to these pads and resonates with the on-chip Rx coil and the voltage rectifier. The value of this capacitor can be changed for tuning the resonance frequency.

The results that are presented in this section reveal another important challenge for wireless power delivery to mm-sized IMDs. As it was shown, the η_{rec} and the input impedance of the voltage rectifier are very sensitive to the P_{avS}. On the other hand, the P_{avS} can be easily changed due to different causes that are discussed in the last section. As a result, the characteristics of the voltage rectifier are affected and the PTE is degraded significantly.

2.3.2 Power Management Unit

A high-performance IMD is composed of several power demanding sub-systems that may operate continuously over time or only for a specific time duration [2]. For instance, data telemetry and stimulation are two power-demanding tasks that are not conducted continuously and change the power consumption of an IMD significantly. Any change in the total power consumption of an IMD changes the effective impedance that is seen by the voltage rectifier and consequently changes the PTE. On the other hand, the available power level at the Rx coil can be easily changed because of the high sensitivity of the wireless link and may cause a power harvesting system not to be able to drive the building blocks of an IMD. A practical power harvesting platform for such systems should be able to deliver milli-Watts of power for the operation of the IMD. However, based on the presented results and analysis on SAR values, η_{link} , and the η_{rec} of the voltage rectifier in previous sections, the maximum harvested power by the mm-sized chip is limited to few-hundreds of micro-Watts.

We have designed and proposed a power harvesting system that is immune to the variations of the η_{link} and can power up implants with a wide range of power consumption. Depending on the available power at the Rx coil terminals and the power consumption of the load, the power delivery mode can be continuous or duty-cycled. Duty-cycled operation of the power-demanding blocks such as a data transceiver is a well-known technique to cope with the limited available power in wirelessly powered systems [47, 54]. Typically, an IMD is composed of sensor array, data transceiver, logic control unit, Analog to Digital

Converter (ADC), and stimulation unit that dominantly controls the power consumption of an IMD. The system architecture of the proposed power harvesting system along with building blocks of a typical IMD is depicted in Fig. 2.14. The power harvesting system includes a six-stage voltage rectifier, a low dropout voltage regulator, and a Power Management Unit (PMU).

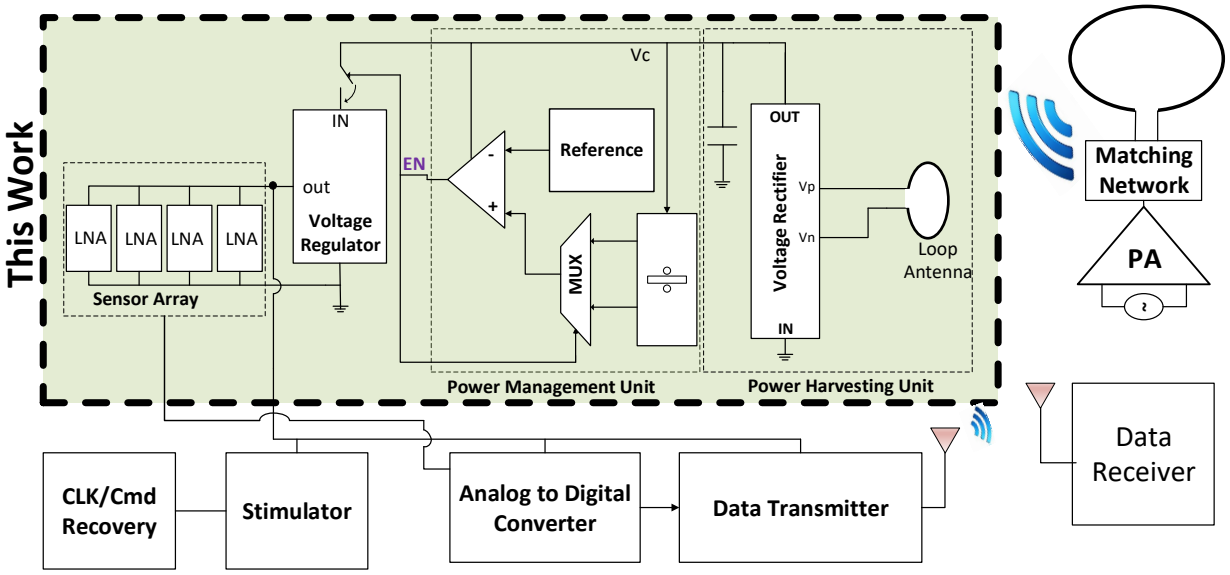

Figure 2.14. System architecture of the proposed power harvesting system.

The main core of the proposed power harvesting system is the PMU, which determines the power delivery mode and sets the activation time of power-demanding blocks of an IMD. If the power consumption of a load that is connected to the voltage regulator is less than the harvested power by the system, the PMU sets the power delivery to continuous mode. In this case, the EN signal is always high and the regulator delivers a constant DC voltage to the load continuously. Otherwise, the PMU disables the voltage regulator and the voltage rectifier charges the storage capacitor and increases the voltage level (V_C). The voltage across the storage capacitor is monitored by the PMU. Once the V_C reaches a predefined high threshold value (V_H), the PMU activates the power-demanding blocks of the IMD. Upon the activation of the entire system, the stored energy is dissipated rapidly and the storage

capacitor discharges in a very short time. It is essential to always keep the V_C higher than a low-threshold value (V_L) to ensure the PMU always remains active. Therefore, the PMU prevents the storage capacitor to be completely discharged and does not allow the V_C to be less than the V_L. After the V_C reaches V_L, the PMU disables the operation of the IMD and the power harvesting unit recharges the storage capacitor.

The operation of the PMU in the duty-cycled mode resembles a hysteresis comparator with two different threshold values. As it is shown in Fig. 3.7, the PMU is realized using a differential voltage comparator, voltage reference generator, a voltage divider, and a multiplexer (MUX). The voltage divider down converts the V_C with two different division ratio , DR_1 and DR_2 ($DR_2 > DR_1$). During charging mode, the EN signal ,which is also the select signal of the MUX, is low and the MUX feeds $DR_1 \times V_C$ to the non-inverting node of the comparator. As the storage capacitor charges to higher voltage levels, the non-inverting nodes exceeds the reference voltage and the EN signal goes high. At the same time, the voltage level on non-inverting node of the voltage comparator changes to $DR_2 \times V_C$ and C_S discharging begins. The rapid jump of non-inverting voltage level causes the EN signal to stay high till $V_{ref} = DR_2 \times V_C$ and forms the hysteresis behavior of the PMU.

The circuit schematics of all PMU parts are shown in Fig. 2.15. It is extremely important to minimize the power consumption of all constituent blocks in the PMU to improve the sensitivity of the power harvesting unit. To do so, all constituent blocks in the PMU are designed to operate in the deep sub-threshold region and the bias current of the comparator is reduced as much as possible. In order to reduce the voltage level of the signal that is fed to the comparator, a chain of eleven diode-connected transistors with the same dimensions is used to realize the voltage divider. The MUX is implemented with an NMOS and a PMOS transistors that are connected to the voltage divider as it is shown in the schematic. One of the most important blocks of the PMU is the reference generator. It provides a constant voltage to be compared with the output of the MUX and the accuracy of the generated

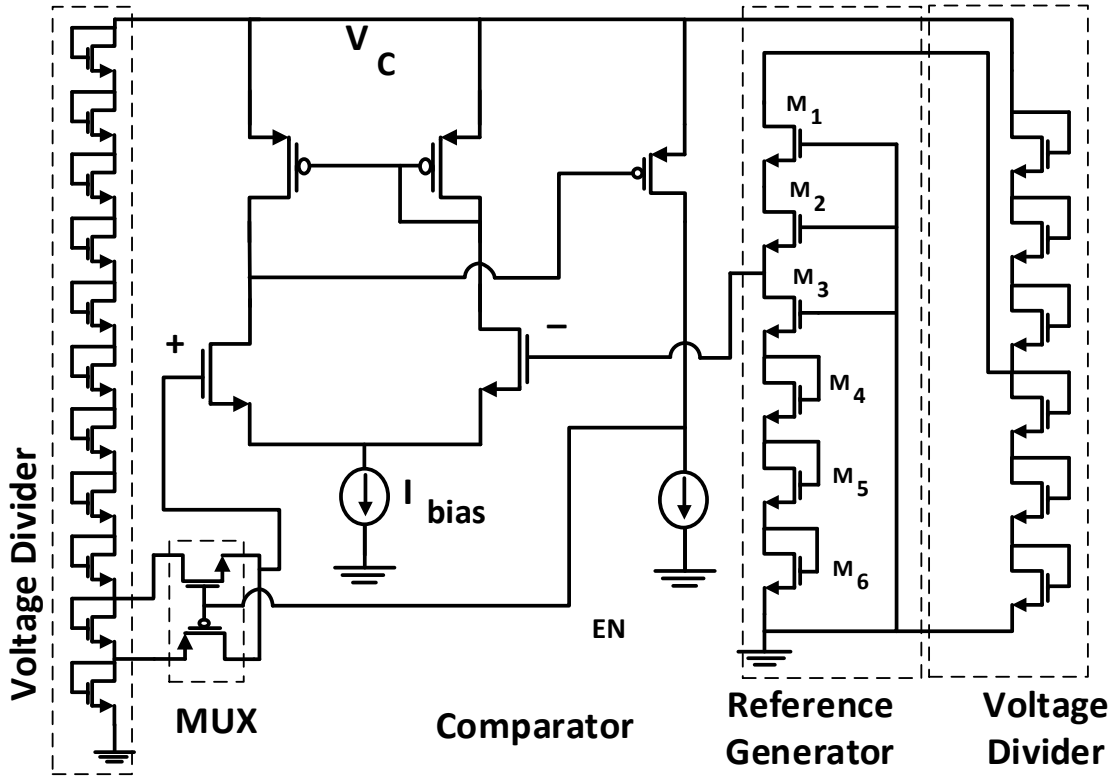

Figure 2.15. Circuit schematic of the PMU.

voltage controls the V_H and V_L values. Since the V_C is has a large fluctuation in the duty-cycled operation, it is halved by a voltage divider before being used as the supply voltage for the reference generator. The basic principle of the operation of the voltage reference is based on the threshold voltage difference of double-gate and single-gate CMOS transistors [55]. This structure provides a low Line Sensitivity (LS) while consuming a negligible amount of power. In this design, two single-gate NMOS transistors and four double-gate transistors are stacked to increase the voltage level and achieve the desired reference voltage.

The discharging time of the storage capacitor is mainly determined by the load current and size of the storage capacitor, which is shown in (4.6).

$$\frac{\Delta V}{\Delta T} = \frac{I_{load}}{C_S} \tag{2.13}$$

The discharge rate should be kept less than the slew-rate of the voltage comparator in the PMU to ensure that the EN signal tracks the V_C during activation time of the regulator load. According to (4.6), discharging rate can be reduced by either increasing the size of storage capacitor or reducing the load. Transient response of the power harvesting system in discharging mode is limited by the slew-rate of voltage comparator in the PMU which is 10 mV/μs. Therefore, to ensure the power harvesting system properly operates, discharging rate of the storage capacitor should be less than the slew-rate of the comparator.

2.3.3 Voltage Regulator

The power-demanding blocks that are activated during discharging mode cannot directly be powered up using the V_C. Hence, an on-chip low-dropout (LDO) voltage regulator is included in the design in order to provide a constant voltage for operation of those blocks. The voltage regulator is implemented with a circuit schematic that is shown in Fig. 2.16. It includes an error amplifier that changes the impedance of a PMOS transistor and maintains a constant voltage at the output node. The output voltage is sampled using two diode-connected single-gate transistors (M_{f1} and M_{f2}) and is compared with a 504 mV voltage that is generated by the reference generator that is shown in Fig. 2.16. Since the V_C has a large fluctuation in the duty-cycled mode, one of the most important design parameters for the voltage regulator is the Line Regulation (LR) that is defined as the ratio of the regulated voltage variation over the supply voltage as expressed in (2.14).

$$LR(\%) = \frac{\Delta V_{reg}}{\Delta V_C} \times 100 \tag{2.14}$$

A 100 pF on-chip capacitor ($C_R = 100$ pF) is used as a decoupling capacitor at the output node of the regulator to improve the line regulation of the LDO and stabilize the output signal. In addition, a Miller compensation technique with a nulling resistor is implemented

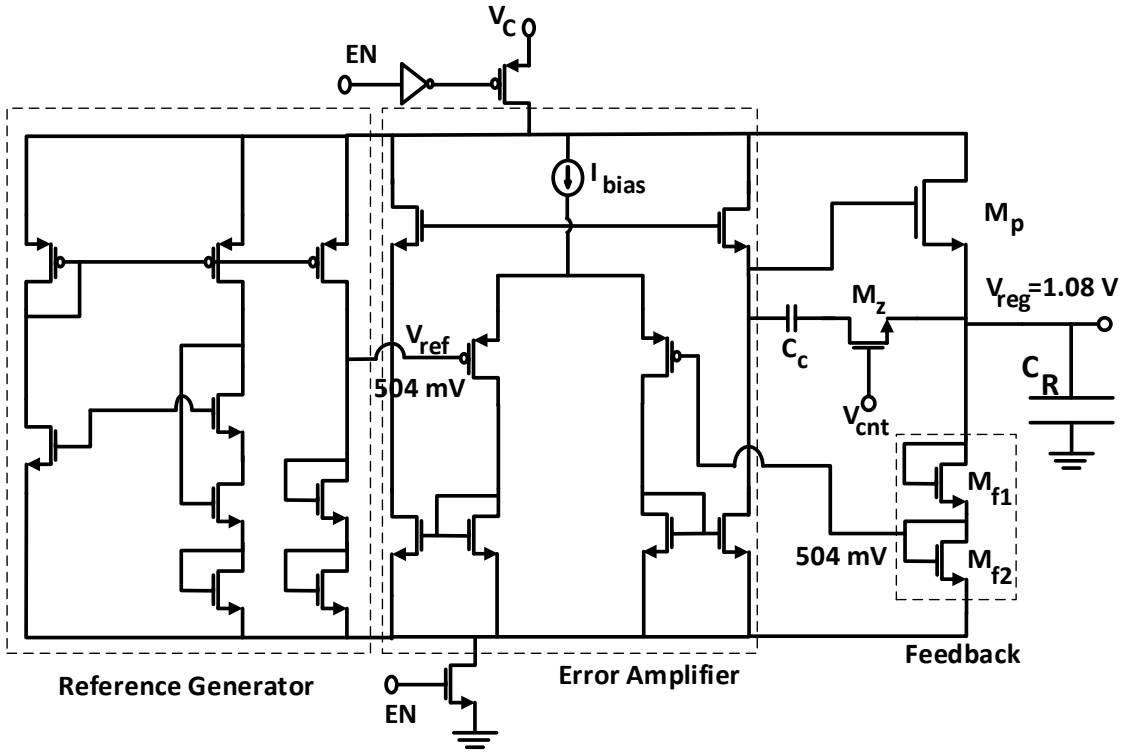

Figure 2.16. Circuit schematic of the voltage regulator.

with a capacitor (C_c = 10 pF) and a 10 kΩ resistor to eliminate right half plane (RHP) zero and improve the stability of the LDO. Simulation results show that the frequency compensated feedback loop has a loop gain of 16.45 dB and a phase margin of 84 degrees at 322 kHz. Transient response of the voltage comparator is faster than the discharging time of the storage capacitor. Therefore, the voltage regulator can fulfill the requirements of the power harvesting system with a quiescent current (I_Q) consumption as low as 10 μA.

The conversion efficiency of a voltage regulator (η_{reg}) is another contributing term in total power transfer efficiency as it is shown in 2.1. Unlike voltage rectifier, the conversion efficiency of a regulator is not a function of operating frequency and can be defined as:

$$\eta_{reg} = \frac{V_{reg} \times I_l}{(I_Q + I_l) \times V_C} \tag{2.15}$$

Where I_l is the output current of the regulator that flows into a load connected to V_{reg} and

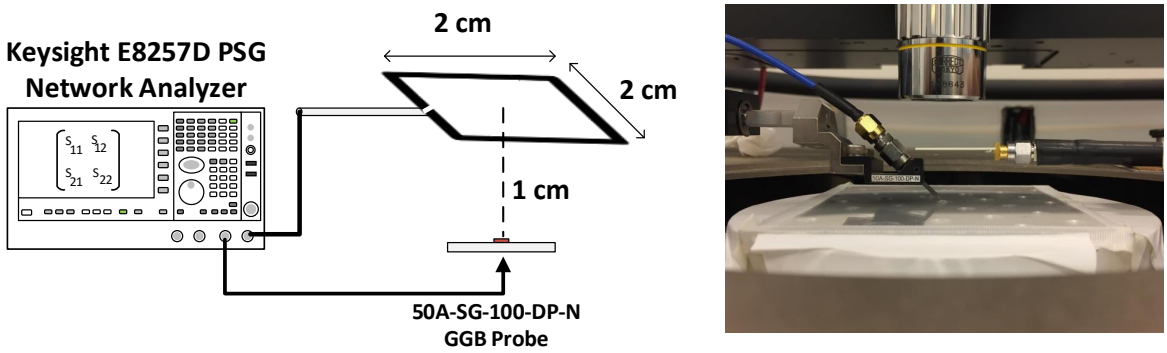

Figure 2.17. Measurement setup for characterizing power transfer efficiency of the wireless link when the Tx and Rx coils are coupled through 10 mm of air.

V_C is the input voltage to the LDO that is connected to the storage capacitor. To maximize the η_{reg}, the difference between V_C and V_{reg} should be as low as possible. However, reducing the level of V_C results in less energy storage across the storage capacitor during charging phase.

2.4 Measurement Results

2.4.1 Wireless Link Characterization

The chip is fabricated in GlobalFoundries 7RFSOI 180-nm technology with an active area of 2.56 mm^2. The on-chip receiving coil is implemented with two turns in the top metal layer of the process with a trace width of 100 μm to achieve small series resistance and a high quality factor.

The η_{link} and the characteristics of the on-chip coil are measured by obtaining the S-parameters between the Tx loop and the fabricated chip. Measurement setup for acquiring S-parameters is shown in Fig. 2.17. In this measurement, a Keysight E8257D network analyzer is used to extract the S-parameters of the system. The Rx coil is connected to the

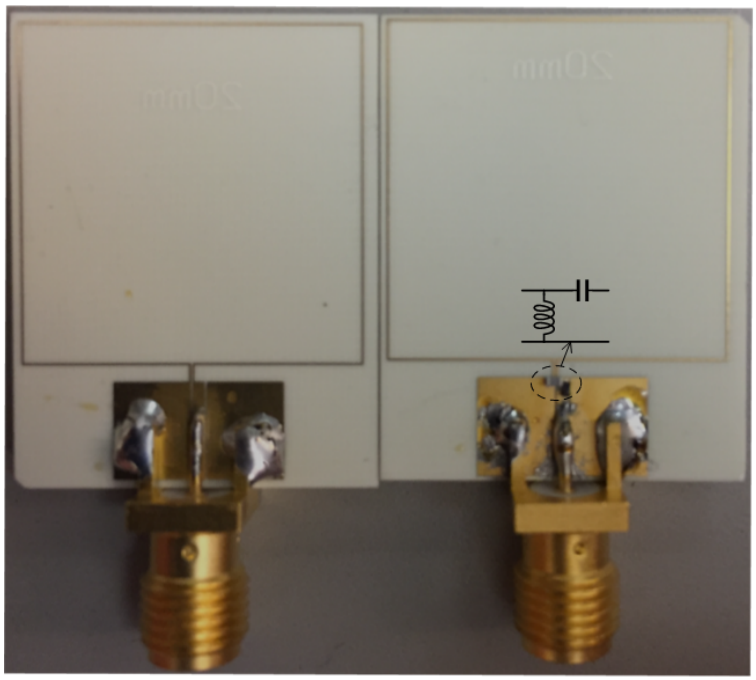

Figure 2.18. Implemented transmitting coil. (a) With no matching component footprint (b) With matching component footprint.

network analyzer using a 50A-SG-100-PD-N GGB probe, which is landed on the bond-pads that are connected to the Rx coil. The chip is mounted on a Plexiglas plate with a thickness of 1 cm to isolate the Rx coil from the conductive chuck of the probe station. The power level of each port in the network analyzer is set to -8 dBm. Considering the value of η_{link}, the power level that is induced at the Rx side is small enough to assume that the voltage rectifier is completely off and does not affect the acquired S-parameters.

The purpose of wireless characterization is detecting the f_{opt}, η_{2port}, η_{link}, and the impedance of Tx and Rx coils for a particular intervening medium between the Tx and Rx coils. First, we have used the transmitter shown in Fig. 2.18(a) in the measurement setup of Fig. 2.17 to obtain the S-parameter of the two-port network. Post processing the acquired S-parameter and using (2.4)-(2.6) leads to detecting f_{opt} and $max(\eta_{2port})$. For

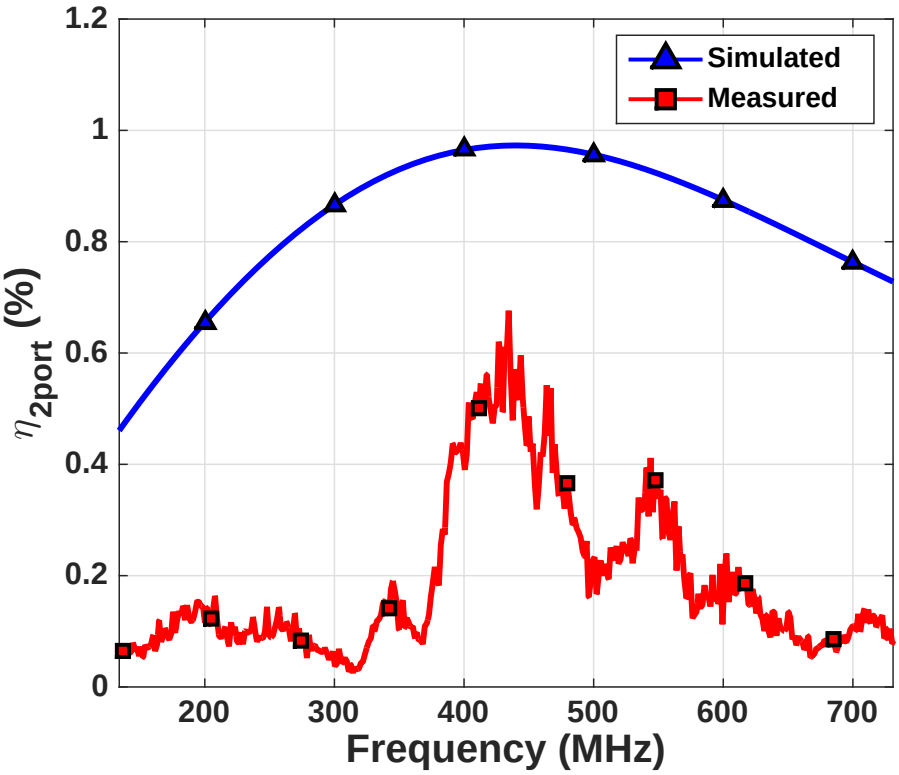

Figure 2.19. Two-port network power efficiency (η_{2port}) of the wireless link at 10 mm separation through air.

instance, the η_{2port} of the two-port network is plotted based on simulated and measured S-parameters in Fig. 2.19 when the Tx and Rx coils are coupled through 10 mm of air. According to the depicted plots, the optimum frequency for power transmission is 434 MHz and the peak value of η_{2port} reaches to -21.7 dB (0.68%). However, simulated peak value of η_{2port} is -20.12 dB (0.97%). This small difference is mainly caused by calibration error and the connecting cables that disturb the electromagnetic fields. The difference between measured and simulated η_{2port} increases as the operating frequency deviates from the optimum frequency. The reason behind this phenomena is that the power level that is sensed at the network analyzer ports becomes smaller for a lower η_{2port}. The contribution of unwanted signals in S-parameter measurement acts as a noise source and causes large

fluctuations in η_{2port} curve. Therefore, the Signal-to-Noise Ratio (SNR) of the signal picked up by the network analyzer is higher around optimum frequency and measured results have a higher accuracy.

In order to evaluate the impact of intervening medium on η_{2port}, we repeated this experiment with two different types of biological tissues. To ensure that the probe is not damaged during the measurement, the tissue is attached to the Tx loop and is placed 2 mm above the chip. Since using the actual human tissue in the measurement process was not possible by the time that the experiment was conducted. Instead, thick layers of chicken breast and bovine muscle are used as intervening biological medium to show the sensitivity of the wireless link to tissue type variation. It should be noted that power absorption of a tissue increases as its water content increases. Considering that both chicken breast and bovine muscle have a high water content, they result in more power attenuation compared with the case that the chip is implanted in the human head or chest with equal implantation depth. Therefore, the link efficiency that is resulted in this experiment is representing the worst condition for an IMD in case of link efficiency. The optimum frequency and the maximum value of η_{2port} for each tissue are reported in Table 2.2. As expected, presence of biological tissues decreases the optimum frequency and degrades η_{2port}.

In the next step, we have used the Tx coil in Fig 2.18(b) to measure η_{link}. The feed line to the transmitter is a Coplanar Waveguide without any ground plane. In order to set the characteristic impedance of the feed line to the reference impedance, the Tx coil is implemented on a Roger 4350B substrate with a thickness of 30 mil. The presence of the gap makes it possible to place different discrete components on the board and match the Tx coil to the source at the desired frequency. It should be noted in the frequency range of interest, the length of matching components is considerably smaller than the wavelength

Table 2.2

PERFORMANCE SUMMARY OF THE WIRELESS LINK WITH DIFFERENT INTERVENING MEDIA

Intervening Medium	f_{opt}(MHz)	$max(\eta_{2port})$ (%)
10mm Air	434	0.97
12mm Air	452	0.5
2mm Air +10 mm Chicken Breast	241	0.56
2mm Air +10 mm Bovine Muscle	237	0.026

of the generated signal by the source. Once the optimum frequency is detected, matching networks are used to maximize the η_{link} at the f_{opt}. A low-pass LC network is implemented to match the Tx coil to the source as is shown in Fig. 2.18(b). The Tx coil with proper matching components is used in measurement setup of Fig. 2.17 and the S-parameters of the two-port network are recorded again. Assuming that the available power level at the receiving coil is 0 dBm, the simulated input impedance of the voltage rectifier is considered as the load of the Rx coil. The impedance mismatch between the Rx coil and voltage rectifier is inserted in post-processing. The η_{link} based on simulated and measured S-parameters of the wireless link are plotted in Fig. 2.20. As it is evident from this plot, the simulation and measurement values are in good agreement and the η_{link} of the wireless link can reach up to -22.57 dB (0.55%).

The characteristics of the on-chip Rx coil is also obtained using the measured S-parameters. Measurement results reveal that when the transmitter and the chip are separated by 10 mm of air, the quality factor of the on-chip coil reaches 14.18 at 434 MHz and the inductance of the coil is 7.30 nH.

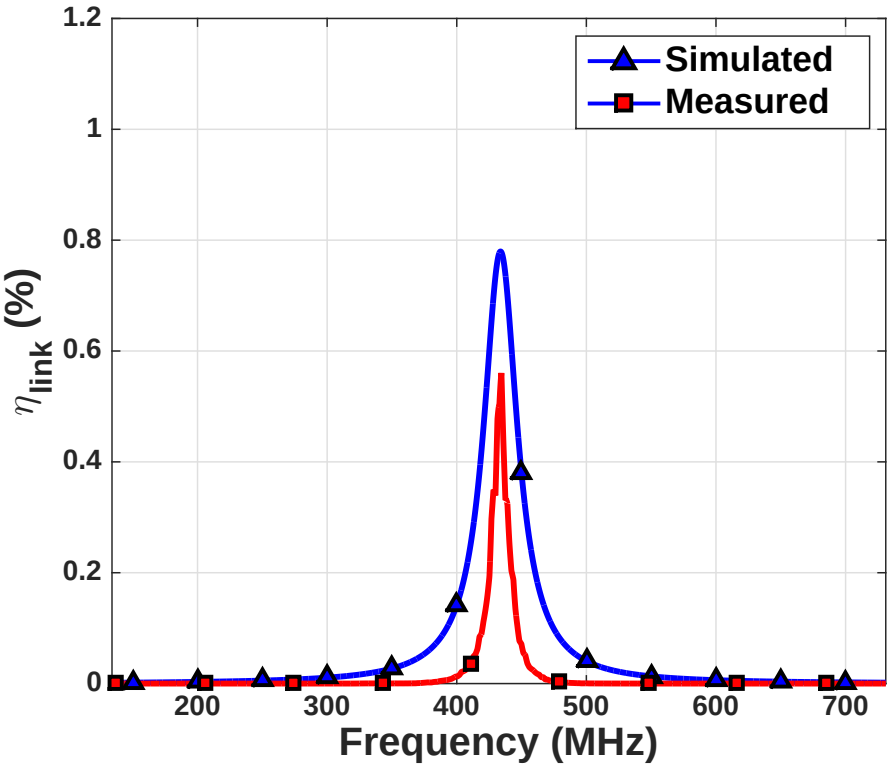

Figure 2.20. Link efficiency (η_{link}) of the wireless link at 10 mm separation through air.

2.4.2 Power Harvesting System Evaluation

In this section, we have evaluated the performance of the entire power harvesting system. Measurement setup for circuitry test is shown in Fig. 2.21 where the chip is mounted on a PCB and the bond pads are connected to PCB traces by bond wires. The main purpose of this experiment is to evaluate the performance of the designed circuitry based on the link characterization that was described in part A. Using a different intervening medium between the coils only affects the performance of the wireless link and changes the available power at the Rx side. As it was explained, a proper matching network can be utilized Tx side eliminate power reflection between the Tx coil and power source. In addition, an off-chip shunt capacitor is placed between the on-chip terminals, which are available via two bond pads, to set the resonance frequency to f_{opt}. The performance of the designed circuitry is

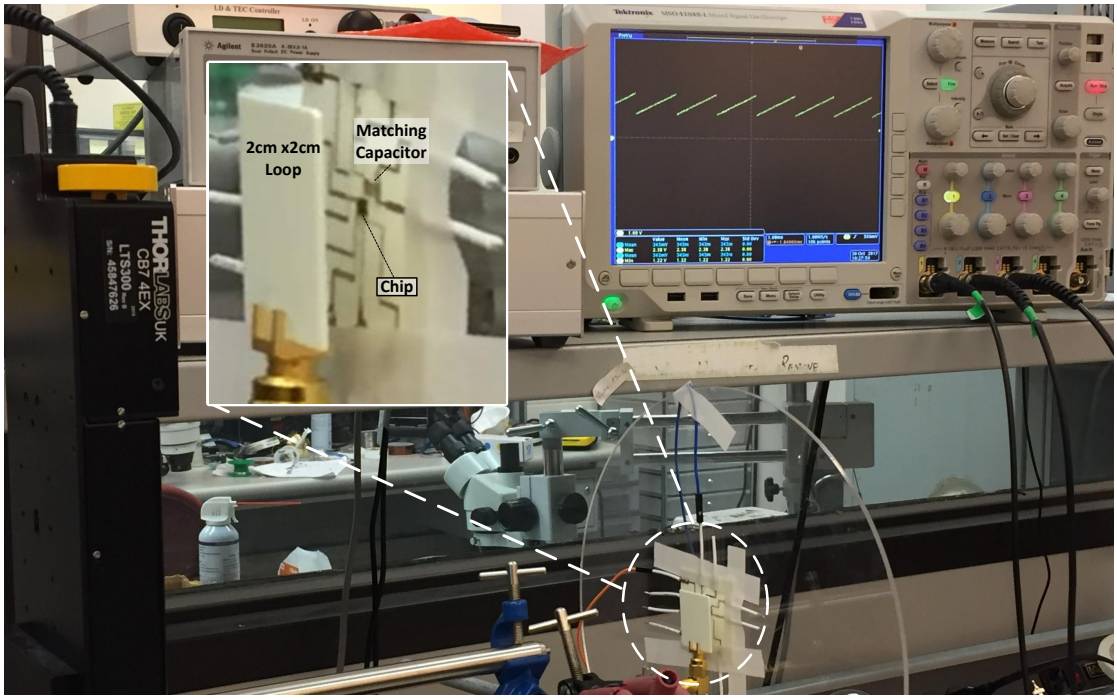

Figure 2.21. Measurement setup for evaluating the performance of the wireless power harvesting system.

evaluated for different loads and transmitted power levels.

In order to evaluate the conversion efficiency of the voltage rectifier (η_{rec}), the power transfer efficiency from the transmitter to the output of the voltage rectifier is measured for different loads. Since a 1.2 nF on-chip capacitor is used at the output of the rectifier, the V_C can be directly used for continuous power delivery to the loads that are constant or have negligible variation. In this measurement, the transmitter is connected to a Keysight PGAE50AB signal generator that operates at 434 MHz and the output voltage is recorded with a mixed-signal oscilloscope that has an impedance of 1 MΩ ‖13 pF. Fig. 2.22 shows the measured power transfer efficiency from the 2×2 cm^2 transmitter to the output of the voltage rectifier ($\eta_{link} \times \eta_{rec}$). The measurement is done for 20 mW (13 dBm) and 50 mW (17 dBm) of source power level (P_G). At each level, the resistive load that is connected to the V_C is swept and the dc voltage across the load is recorded. The voltage regulator is disabled during

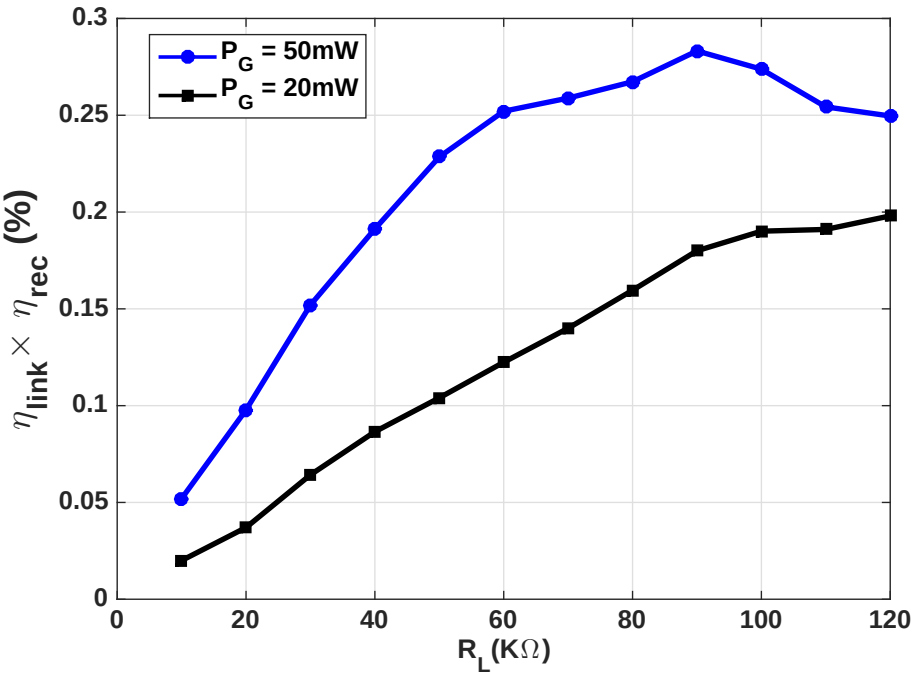

Figure 2.22. Measured power transfer efficiency at 434 MHz from a 2×2 cm^2 loop to a resistive load connected to the voltage rectifier.

the measurements. Therefore, the voltage level of the V_C can exceed the V_H. To ensure that there is no damage to the transistors, the input power level is not increased more than 17 dBm. Knowing the value of the η_{link}, the η_{rec} can be extracted from this measurement by de-embedding the power attenuation that is caused by the two-port network and matching networks.

The performance of the PMU and the voltage regulator are also evaluated for different transmitted power levels and loads. Measurement results show that when the generated power of an RF source is limited to 24 dBm, the power harvesting system can continuously provide a constant 1.08V dc voltage for resistive loads that are larger than 20 kΩ. It worth mentioning that the transmitted power level is under FCC regulation ($1.6W/Kg$). According to Fig .2.10, the maximum allowable transmitted power from the Tx coil for the simulated head model is 30.7 dBm.

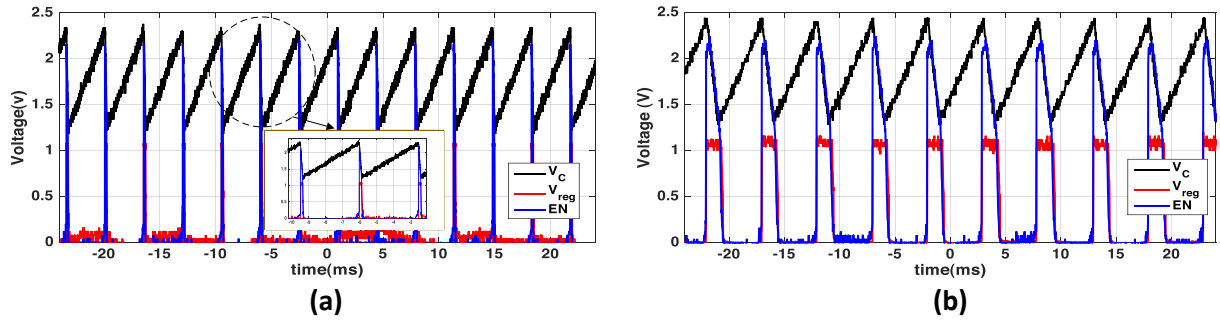

Figure 2.23. Recorded waveform from the power harvesting system when $P_G = 15$ dBm and $C_S = 101.2$ nF (a) Regulator load: 1 kΩ (b) Regulator load: 8 kΩ

The overall power transfer efficiency of the system is strongly dependent on the available power level at the Rx coil and the load size since the conversion efficiency and impedance of the rectifier are greatly affected by both of these parameters. The power harvesting system can be optimized for a specific load and transmitted power to improve the power transfer efficiency. However, in a real-case scenario, these parameters cannot be controlled.

For a given transmitted power from the Tx coil, the available power at the Rx side can be reduced significantly by tissue variation, coil misalignment, or deviation of operating frequency from f_{opt}. In addition, the load size of the system also may change. As a result, the available power at the Rx coil may not be sufficient for driving the load continuously. In this situation, the system changes the power delivery to duty-cycled mode. Fig. 2.23 shows the operation of voltage regulator and the PMU in the duty-cycled mode while the V_C is periodically charges and discharges. In order to limit the discharging rate of the storage capacitor, an external 100 nF capacitor is used in parallel with the on-chip capacitor. The plotted waveform in Fig. 2.23 indicates that the voltage regulator can successfully provide 1.08 V for the 1 kΩ load during discharging mode. The recorded waveform shows that the voltage regulator achieves an LR value of 3%, which imply that the regulated voltage has very small variation while the V_C is highly fluctuated and changes from 1.24 V to 2.44 V. For this amount of voltage fluctuation across storage capacitor, η_{reg} changes from 87% to 45% when a 1 kΩ load is connected to the regulator. The power harvesting system can deliver

TABLE III

PERFORMANCE COMPARISON OF WIRELESS POWER HARVESTING SYSTEMS

	This Work	JSSC'17 [13]	TBCS'16 [18]	TBCS'15 [12,19]	JSSC' 15 [16]	ISSCC'09 [10]
Process	**0.18μm SOI CMOS**	0.18μm SOI CMOS	65 nm CMOS	0.13μm CMOS	65 nm CMOS	0.13μm CMOS
Rx Coil Area (mm^2)	**1.6x1.6**	3x3	2x2	2x2.18	6.5x6.5	2x2
Coil Inductance (nH)	**7.3**	23.7	N/A	130	32	N/A
On-chip Coil	**Yes**	Yes	No	Yes	No	No
Power Delivery Mode	**Continuous/ Duty-cycled**	Continuous	Continuous	Continuous	Continuous	Continuous
Frequency (MHz)	**434**	144	1320	160	300	915/1000
Maximum η_{link} (%)	**0.68**	2.75	0.02	1.42	2.24*	-0.08
Intervening medium	**10mm Air**	10mm Air	35mm Porcine Heart	10 mm Air	12.5 mm Intracranial	15mm Bovine Muscle
On-chip storage	**Yes****	No	No	No	No	No
Regulation Method	**LDO**	Regulating Rectifier	LDO	LDO	LDO	LDO
V_{out}	**1.1**	0.8	0.7	3.1	0.5	1.2
Line Regulation (%)	**3**	N/A	N/A	N/A	N/A	N/A
Decoupling Cap (pF)	**100**	1000	1.4	20	4000	N/A
FOM	**165.1**	102	84.9	156.2	15.92	33.51

*: Simulated

**: Only in continuous mode

up to 1.17 mW of power during discharging phase. It is worthwhile to mention that the delivered power in discharging mode can be increased by using a larger storage capacitor that limits the discharging rate. In addition, the duty cycle of the power delivery can be controlled by adjusting the level of transmitted power or changing the load of the voltage regulator.

The key performance parameters of the power harvesting system are compared with state-of-the-art mm-sized power harvesting systems in Table 2.3. It should be noted that increasing the size of on-chip coil and decreasing the separation distance improve the η_{link}. In order to compare the performance of the chip with other tabulated designs, we have used a Figure of Merit (FOM) that is proposed by Zargham and Gulka in [19]. The proposed FOM is proportional to the cube of the distance between transmitter and receiver, which is

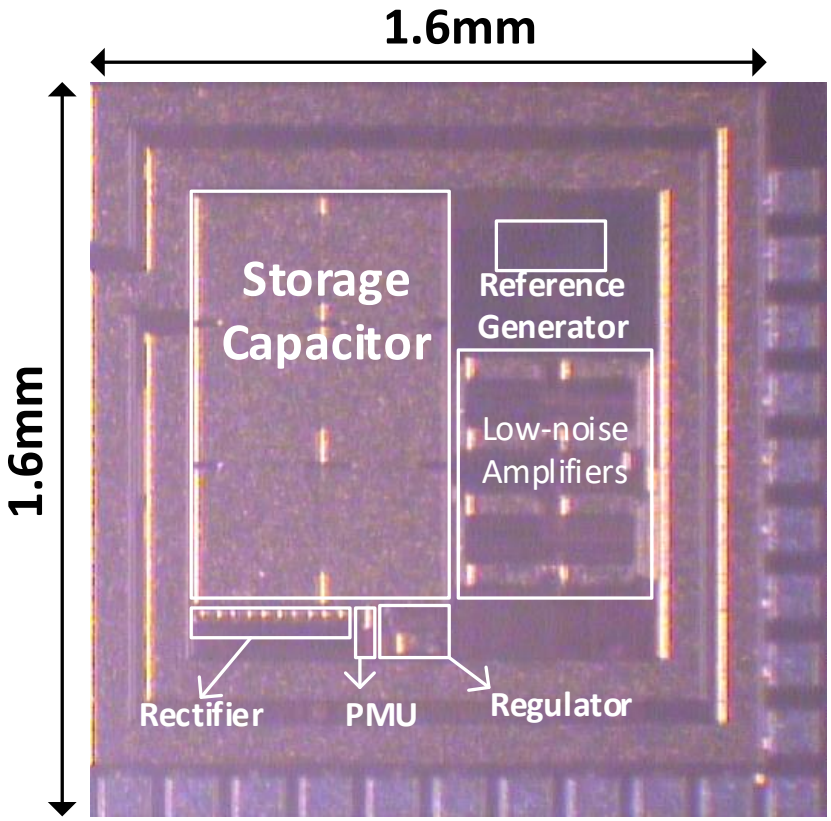

Figure 2.24. The chip micrograph of the power harvesting system fabricated in 0.18μm SOI CMOS technology

expressed as:

$$FOM = \frac{\eta_{link}(\%) \times d^3}{A^{3/2}} \tag{2.16}$$

Where d is the distance between the antennas and A is the area of the on-chip coil. However, the type of tissue that impacts the η_{link} is not included in this FOM. The designed power harvesting system can achieve a FOM of 165.1 and has the smallest area among the tabulated works.

2.5 Conclusion

This Chapter presented a 1.6×1.6 mm^2 dual-mode wireless power harvesting platform with an on-chip coil for mm-sized biomedical implants. The system is fabricated in 180-nm SOI CMOS process and the chip micrograph is depicted in Fig. 2.24. The design introduces a power management technique that makes the power harvesting system immune to the variations of wireless link efficiency that can be caused by tissue type variation, misalignment, and movement of Tx and Rx coils. Depending on the available RF power at the Rx and the power consumption of the load, the PMU sets the power delivery state to continuous or duty-cycled mode, which enables the system to drive implants with a wide range of power consumption. Measurement results show that the designed system achieves a wireless link efficiency of 0.68% and a FOM of 165.1. The fabricated chip adaptively sets the power delivery mode is capable of delivering up to 1.17 mW in the duty-cycled mode while the amount of transmitted power is 15 dBm.

CHAPTER 3

RF-Powered Fully Integrated Radios for Supporting High-Throughput Communication

3.1 Introduction

Emerging applications of biomedical devices have shown an ever-increasing demand for data acquisition with higher bandwidth and a higher resolution. For instance, research on the anatomical, physiological, and computational bases of human cognitive and motor functions has made important strides in recent years but has been limited by a glaring lack of information on the dynamics of processes. This is a methodological limitation related to the low spatial and temporal resolution of widely available tools such as fMRI, EEG, behavioral, and stroke lesion-based approaches [8, 9]. Today, neural interface implantable systems are becoming increasingly popular as they have demonstrated great potentials in novel diagnostic and treatment methods. They are used in a variety of applications such as Brain-Machine Interface (BMI) systems, cochlear implants, and retinal prosthesis [23, 56–58]. To address clinical constraints and alleviate infection risks, wireless operation is a necessity for human implantable systems. Therefore, commercial implants utilize either batteries or inductive coupling through a pair of coils for powering the internal electronics. Also, bidirectional data transmission is conducted through a wireless link that utilizes electromagnetic (EM) antennas. Recent advances in semiconductor technology have resulted in a significant integration capability and size reduction of electronics. However, the overall size of an implant is not scaled with the same rate since it

is dominantly controlled by the size of required components for powering and data communication. Battery-powered devices cannot be made smaller than a few centimeters since the power density of state-of-the-art batteries fail to address the demands of long-term miniaturized implants. On the other hand, the power transfer efficiency of inductively coupled coils is proportional to coil dimensions; thus miniaturizing the power coils beyond a certain limit is not possible [14, 15, 17].

Miniaturizing the size of an implant is the key step for fulfilling the needs of next-generation implantable systems since it results in a higher sensor density and also enables signal recording at an ultra-small structural scale. A conceptual neural prosthetic system is illustrated in Fig. 3.1 to highlight the importance of miniaturization for future neural interface implants. Neural activity is sensed by a network of distributed multi-site sensors and transmitted to an external processor. The processed data is used for decoding the brain signal in a patient who is suffering from spinal cord injury. After interpretation, proper stimulation commands are transmitted to the arm muscles to enable the patient to move their hand in the desired direction. For a real-time human brain monitoring, it is desired to increase the number of recording sites as much as possible. Recent neural recording systems have reported up to 4096 recording electrodes [59]. On the other hand, various recording methods such as ECoG or spike recording demand different sampling rates that may reach as high as 10 KSps per channel. Hence, the overall communication bandwidth may exceed tens of Mbps.

A practical data transceiver (TRX) should support the demanded bandwidth and be compatible with all of the system-level requirements of miniaturized implants. Achieving such a high data rate is extremely difficult due to severe power budget constraints and poor performance of *electrically small antennas* [60] used for power harvesting and data communication. When the transmitted power level to a mm-sized power receiver is limited by safety regulations, it has been shown that the maximum harvested power is about a few hundreds of micro-Watts [19, 61–63]. Moreover, the wavelength of EM waves at the

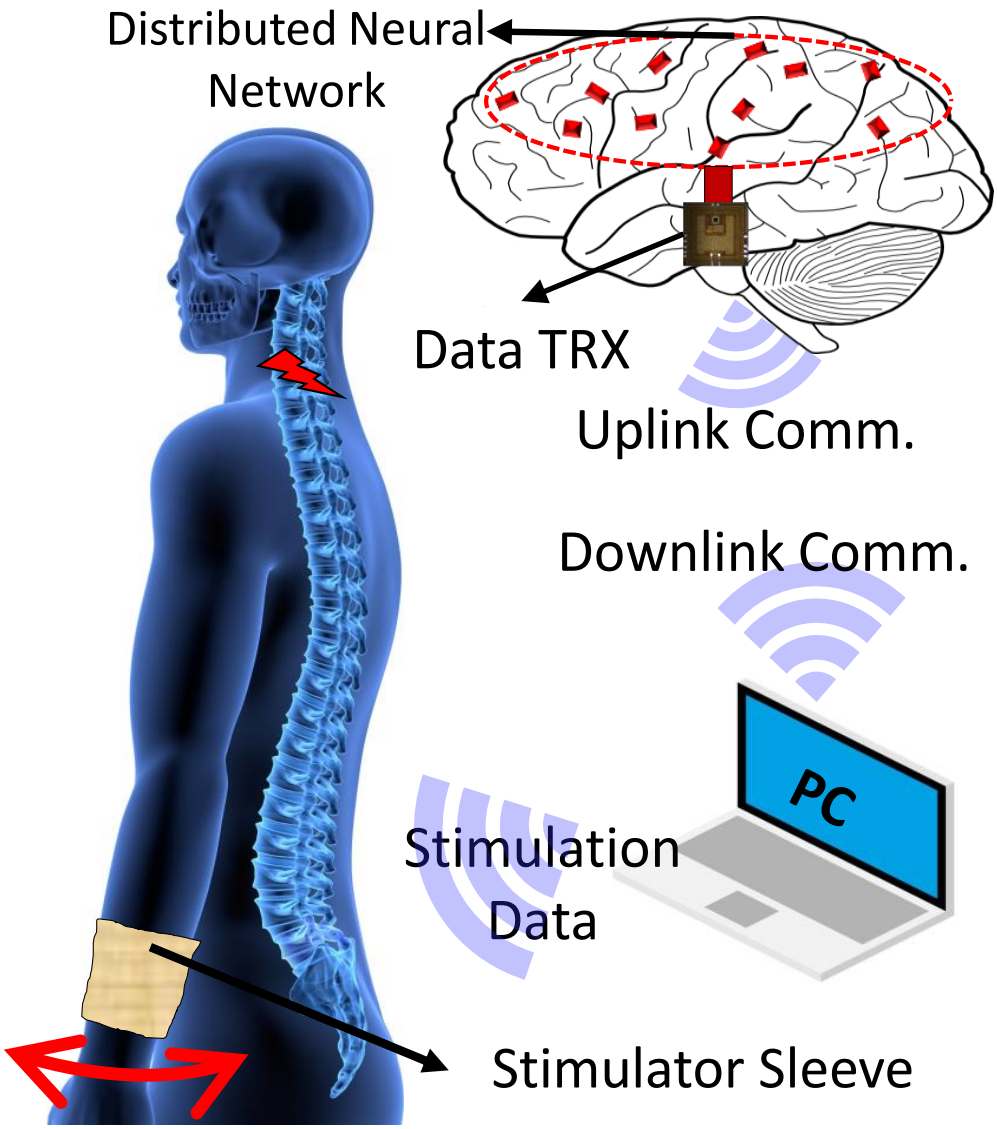

Figure 3.1. Conceptual view of a closed-loop neural recording and stimulation system for next-generation neural prostheses.

frequencies that data communication is typically conducted ranges from tens to hundreds of centimeters. A mm-sized antenna is often much smaller than the wavelength and has a poor radiation efficiency. Therefore, an ideal TRX for mm-sized implants should achieve a very high energy efficiency to support high data rates.

Backscattering is a widely adopted technique for telemetry in implantable applications

since it results in extremely low power consumption. The transmitted data pattern is used for Load Shift Keying (LSK) modulation of the power coil which alters the reflected signal to an external reader. Despite achieving a superior energy efficiency compared with active communication, backscattering radios fail to address the main requirements of mm-sized implants. Due to the small size of the power coil and a strong power carrier, that acts as a blocker, detection of the reflected signal on the reader side may be difficult or even impossible [64, 65]. In addition, modulating the power coil disrupts the power flow into the system and degrade power transfer efficiency. Furthermore, the communication bandwidth of backscattering radios is often very low due to the high quality factor (Q) of the power coil that limits the data rate, consequently [66].

Active TRXs do not face the fundamental challenges of their backscattering counterparts and can potentially achieve high data rates at the expense of higher power consumptions [67–70]. Considering the stringent power budget in implantable applications, the main design goal is achieving the highest possible energy efficiency; and proper modulation schemes should be chosen. It is well known that there is a trade-off between energy efficiency and spectral efficiency in communication systems [71]. Narrow-band modulation schemes demand a relatively complex architecture to generate an accurate frequency whereas wide-band modulation schemes such as On-Off Keying (OOK) have often less complexity and result in a higher energy efficiency.

This Chapter presents the design, implementation, and verification of a fully integrated and RF-powered wireless data TRX. The proposed radio achieves the state-of-the-art energy efficiency and the smallest form-factor compared with prior art mm-sized wirelessly powered active radios [1]. The system is implemented on a single CMOS silicon chip and all required components for power delivery, energy storage, and data communication, including an on-chip coil and a dipole antenna, are implemented on the same chip. The TRX is designed to enable simultaneous power delivery and data communication through two distinguished wireless links separated in the frequency domain. The design supports data rates of up to 2.5

Mbps in the receiver and data rates of up to 150 Mbps in the transmitter chain, respectively. The implemented system occupies a total area of 2.4×2.2 ×0.3 mm^3 without any substrate thinning and features a fully on-chip integration that potentially results in cost reduction, elimination of any post-fabrication process, and reliability improvement.

The rest of this Chapter is organized as follows. In Section 2, I provide an overview of the proposed TRX and describe the high-level system operation. Section 3, explains wireless link design and frequency selection considerations for power delivery and data communication. In Section 4, I focus on design details of incorporated circuitry in the power harvesting system, receiver, and transmitter. Section 5 presents experimental results and Section 6 concludes this Chapter.

3.2 System-Level Description

The high-level block diagram of the proposed wirelessly powered TRX is shown in Fig. 3.2. The TRX is powered through a Radio Frequency (RF) link operating at 250 MHz. The system incorporates a power harvesting system, composed of a rectenna and a power management unit (PMU), a data receiver (RX), and a reconfigurable data transmitter (TX). Besides, two antennas are integrated on the same chip to enable simultaneous power delivery and data communication. An on-chip coil is shared between the power harvesting system and the RX while the TX utilizes a dipole antenna for wireless transmission. In this design, the main goal is to achieve an energy-efficient data communication in both RX and TX chains to enable high-data-rate wireless communication under severely restricted power budgets rendered by a mm-sized power harvesting system. We have adopted extensive optimization and power reduction techniques in the design of the wireless link and incorporated circuitry. Besides, data modulation schemes and TRX architecture are carefully chosen to minimize circuit complexity and overall power consumption.

The robust operation is enabled by the following techniques:

1. Co-optimizing the power receiving coil and the wireless link with voltage rectifier to maximize power transfer efficiency.

2. Employing a PMU to set the operating mode and biasing condition of different blocks depending on their power consumption and the total available power budget.

3. Utilizing a dual-antenna architecture to minimize the interference between power link and the TX.

4. Exploiting amplitude-based modulation schemes in the TRX for maximizing energy efficiency and utilizing an architecture based on a power oscillator (PO) in the TX block to achieve the highest possible energy efficiency.

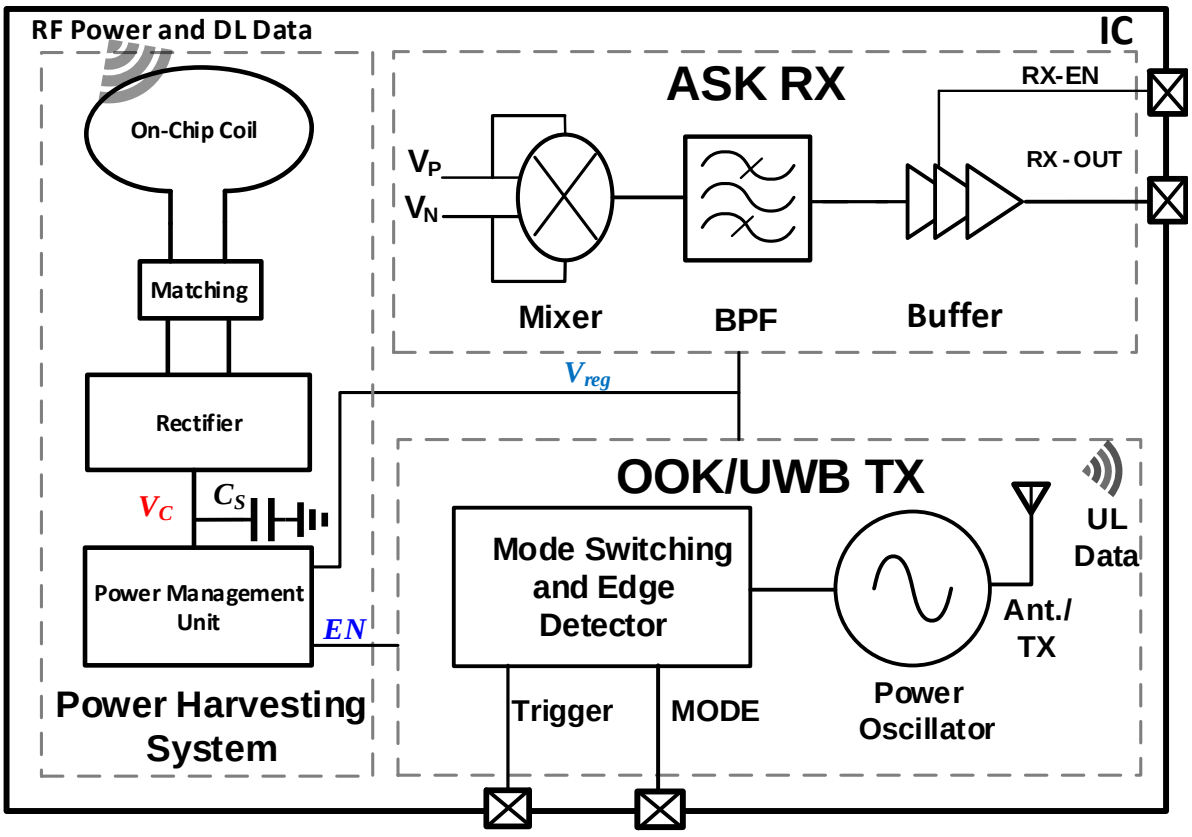

Figure 3.2. Block diagram of the wirelessly powered FDD radio.

The required data rate of TX and RX paths in medical implants vary considerably and thus the communication is asymmetric [72–74]. The wireless link from an external reader to the RX, hereinafter reffed to as downlink (DL) demands a data rate that does not exceed a few Mbps. On the other hand, the wireless link from the TX to an external reader, hereinafter referred to as uplink (UL), requires a large bandwidth to support data rates up to hundreds of Mbps. In this design, the DL data is incorporated into the power link with an Amplitude Shift Keying (ASK) modulation scheme. The RX block is directly powered by the power harvesting system and is active during the entire operation of the system. Hence it is imperative to minimize the overall power consumption of the RX. To enable simultaneous UL and DL communication, we have exploited the Frequency Division Duplexing (FDD) technique and set the center frequency of the UL in the GHz region. Such a high center frequency alleviates the undesired effects of the strong power link on the TX communication and minimizes the interference of UL and DL. Besides, the efficiency of a mm-sized antenna improves as the frequency increases to the GHz region. The UL communication incorporates amplitude-based modulation schemes due to their superior energy efficiency and less sensitivity to supply variation as opposed to frequency-based modulation schemes. The TX block can be configured to transmit UL data with either OOK or Ultra-Wideband (UWB) modulation.

The PMU converts the unregulated output voltage of the rectifier to a constant dc voltage and adjusts the power consumption of the entire system. The maximum harvested power in mm-sized implants is often less than the power consumption of a power-hungry block such as a data TX. A common technique to tackle this problem is duty-cycling the operation of power-demanding blocks and lowering the overall power consumption of the system [47, 61, 75]. Depending on the power consumption of each block, PMU sets its power delivery scheme to either continuous or duty-cycled. A storage capacitor (C_S) is used for storing the converted energy by the rectifier and a voltage limiter is included in the PMU to prevent any voltage breakdown. The most power-demanding block of the proposed system is the data TX. Therefore, the PMU monitors the voltage level across C_S and establishes active and

sleep modes for the TX operation. The waveforms of the internal nodes of the PMU in a duty-cycled power delivery scheme are illustrated in Fig. 3.3(a). If the harvested power falls below TX power consumption, the TX block is periodically deactivated by the EN signal to allow the PMU to maintain V_C higher than a minimum threshold amount (V_L) that is required for continuous operation of the RX block and internal circuitry of the PMU. For the entire duration of the sleep mode ($t_{charging}$), the rectifier charges the C_S and V_C rises until it reaches a predefined threshold (V_H). If the harvested power is sufficient for continuous operation, EN stays low and V_C settles at a voltage level between V_H and V_L as shown in Fig. 3.3(b).

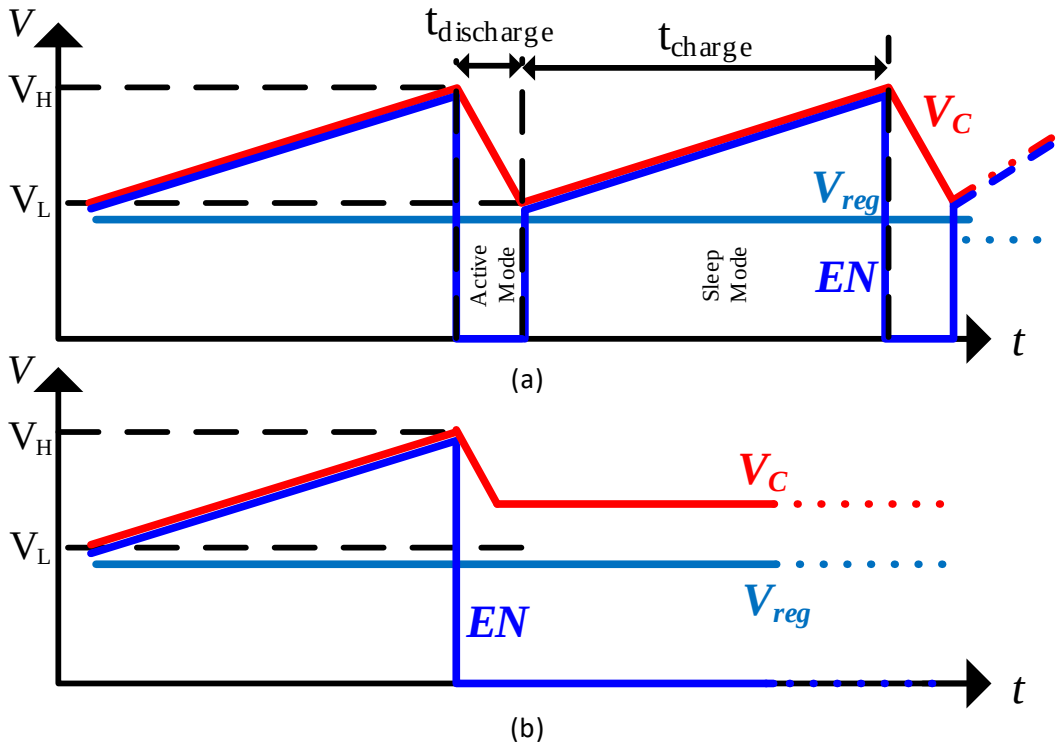

Figure 3.3. Timing diagram of PMU internal nodes in different power delivery schemes. (a) Duty-cycled. (b) Continuous.

3.3 Wireless Link Implementation

The wireless link in this design includes two distinct antennas that are used in DL and UL paths. In this design, we have implemented both antennas with a planar low-profile shapes to comply with the on-chip integration considerations and achieve a mm-sized form-factor. To enhance the harvested power for the system operation and maximize the data rate in the UL path, it is imperative to optimize the antenna dimensions and operating frequency.

Wireless power harvesting systems for small implants have been reported in the literature where link optimization, optimum operating frequency, the effect of intervening biological tissues, safety considerations, and rectifier design are discussed extensively [16, 35, 61]. The wireless link is often modeled as a two-port network and the link optimization is conducted through an iterative algorithm that aims to maximize the power transfer efficiency. The two-port network model for a wireless link is a general approach and can be applied to any wireless link operating at near-field or far-field electromagnetic region with different link composition surrounding the antennas. Therefore, we have used the same approach for optimizing the TX antenna and the uplink. On the other hand, since power delivery and UL communication are conducted at two frequencies that are largely distanced from each other, the optimization procedure of DL and UL can be decoupled and done separately. After applying the design constraints imposed by the application requirements such as the available area and operating distance, we have adopted the same optimization algorithm as in [61]. The DL antenna that is used for power harvesting is implemented as a two-turn square-shaped on-chip coil (OCC) and the UL antenna is realized as a dipole antenna. The optimal dimension of both antennas and their relative location on the chip is illustrated in Fig. 3.4.

To decide the DL operating frequency the power transfer link is modeled and simulated with Ansys High-frequency Structure Simulator (HFSS). The simulation configuration of the wireless link is illustrated in Fig. 3.5(a) where the external power transmitter is implemented

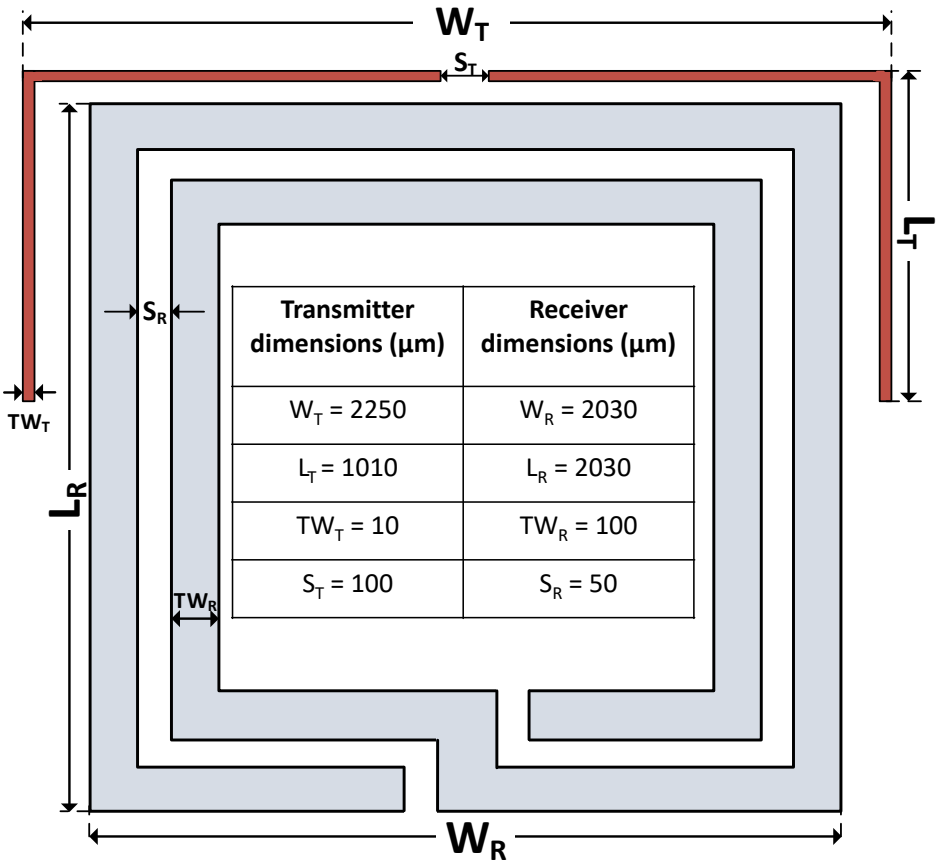

Figure 3.4. Detailed view of the on-chip coil and the on-chip dipole antenna.

as a 2cm × 2cm two-turn square-shaped coil and is separated from the OCC through a 1-cm air gap. To increase simulation accuracy and capture the effect of parasitics, the layer map of the design kit is imported into HFSS. A complete model of the OCC on a silicon substrate is shown in Fig. 3.5(b). Simulation results show that the implemented OCC has an inductance value of 13.6 nH and achieves an unloaded Q-factor of 14.3 at 250 MHz. The maximum power transfer efficiency of the link, which occurs for conjugate impedance matching, is plotted in Fig. 3.5(c). The simulated results reveal that under perfect impedance matching condition, the optimum frequency for power transmission is about 298 MHz. However, throughout the measurement process, we realized that power transmission at 298 MHz interferes with the TX block due to injection pulling phenomena. Hence, we have chosen 250 MHz for power

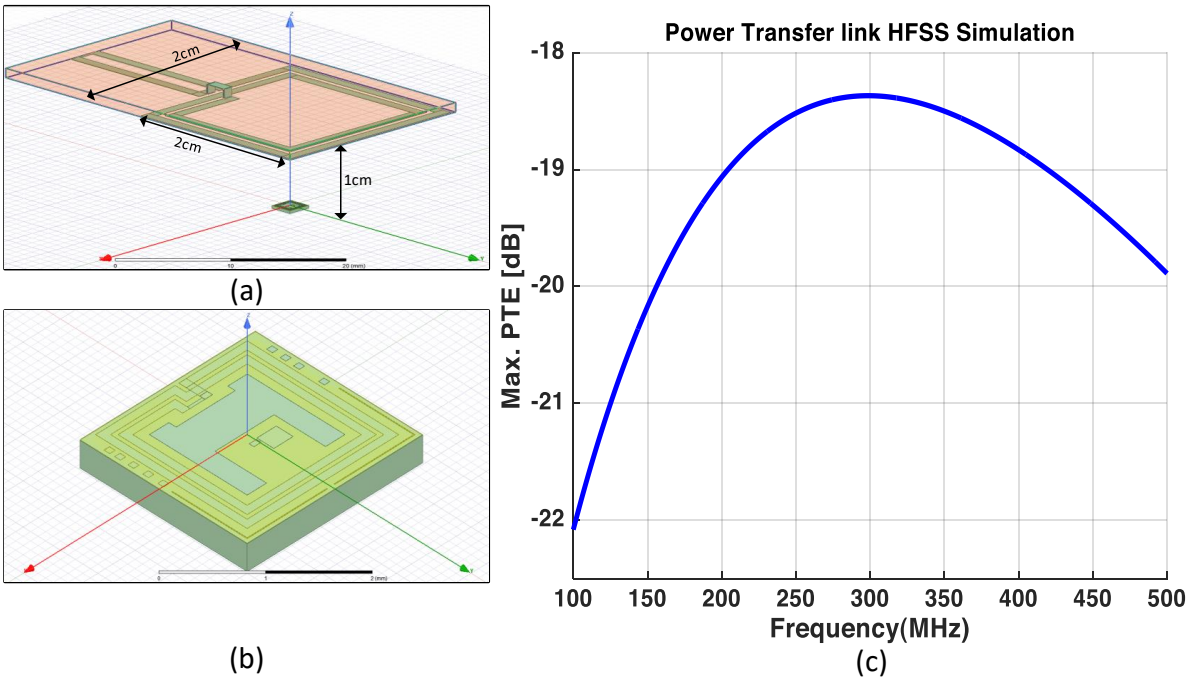

Figure 3.5. (a) HFSS configuration for simulating power link. (b) Complete model of the OCC on a silicon substrate including the effect of parasitics and isolation layers. (c) Simulated maximum PTE of the wireless link.

transmission to ensure reliable operation for the TX block. Further details on this issue are described later in this paper. Taking the impedance mismatch effect into account, the power transfer efficiency degrades to -22.6 dB at 250 MHz.

The link efficiency and optimal operating frequency for UL path are also acquired from HFSS simulations with a configuration shown in Fig. 3.6(a). A wideband monopole antenna forms a two-port network with the on-chip dipole antenna at various distances. The orientation of the monopole antenna is aligned to match the polarization of the dipole antenna, which is shown in Fig. 3.6 (b). The power gain of the two-port network at various distances is calculated based on the simulated S-parameters and reported in Fig. 3.6(c). It is evident that the UL path shows a relatively flat power gain within the frequency range of 3.5 GHz to 4.5 GHz for various distances between the antennas. Therefore, the center

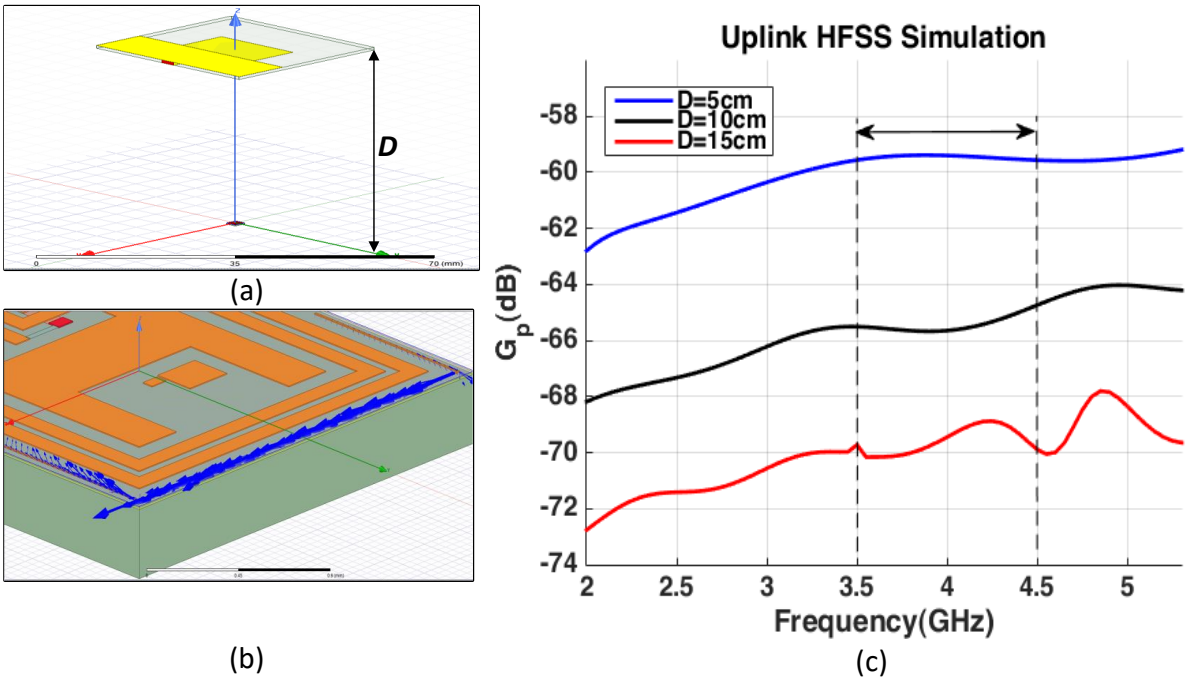

Figure 3.6. (a) HFSS configuration for simulating uplink wireless efficiency. (b) Current density vector of the on-chip dipole antenna. (c) Simulated power gain of the UL configuration.

frequency of the TX block is chosen to be in the middle of this range. The power gain of the UL path at 4 GHz varies from −59.6 dB to −69.8 dB for distances from 5 cm to 15 cm, respectively.

3.4 Circuit Implementation

3.4.1 Power Management Unit

A detailed diagram of the power harvesting system is shown in Fig. 3.7. The rectenna is implemented with a four-stage full-wave rectifier to ensure V_C reaches the required voltage level for the proper operation of the PMU when the transmitted power the external coil is kept below safety limits. To maximize rectifier RF-dc conversion efficiency, transistors

dimensions are optimized. Moreover, deep N-Well NMOS transistors are used to allow a direct connection between bulk and source terminals. Connecting bulk to source eliminates body effect and prevents increments of the threshold voltage of NMOS devices that ultimately improves RF-dc conversion efficiency. An equivalent circuit model for the OCC is illustrated in Fig. 3.7 where the OCC is modeled as a source with an open circuit voltage of V_{OC} and an internal resistance of R_P. A first-order matching circuit is realized using a shunt capacitor that resonates with the OCC at the operating frequency. The simulated conversion efficiency for an available power level of 0 dBm at 250 MHz varies between $30\% - 65\%$ as the rectifier load changes from 235 μW to 420 μW.

The behavior of the PMU in the duty-cycled mode resembles a hysterics comparator that is realized using a voltage divider, a multi-level reference generator, a MUX, and a voltage comparator as shown in Fig. 3.7. The voltage reference block is realized with a supply independent proportional-to-absolute-temperature (PTAT) architecture to generate two reference voltages. The voltage divider, MUX, and the comparator are designed with a similar circuit schematic described in [61]. Once the TX block is activated, C_S discharges and V_C drops rapidly. The $t_{discharge}$ is proportional to the value of C_S. Therefore, it is desired to maximize the capacitance value of C_S to extend the active mode. To achieve the highest capacitance value with area constrains of an on-chip design, we have stacked MIM capacitors over MOSCAP devices with a density of $2fF/\mu m^2$ and $5.5fF/\mu m^2$, respectively to realize a 5 nF capacitor.

A low-dropout (LDO) voltage regulator is incorporated into the PMU to provide a constant 1.3 V dc voltage for operation of the TX and RX blocks. During charging mode, the total current consumed by the LDO is 10 μA. It is ensured that the LDO is stable for all values of V_C during sleep mode. Simulation results show that the minimum phase margin of the LDO is 88° and the gain margin always remain above 20.5 dB. The transition from sleep mode to active mode represents a significant load variation for the LDO. The small quiescent current consumption of the LDO limits the transient response of

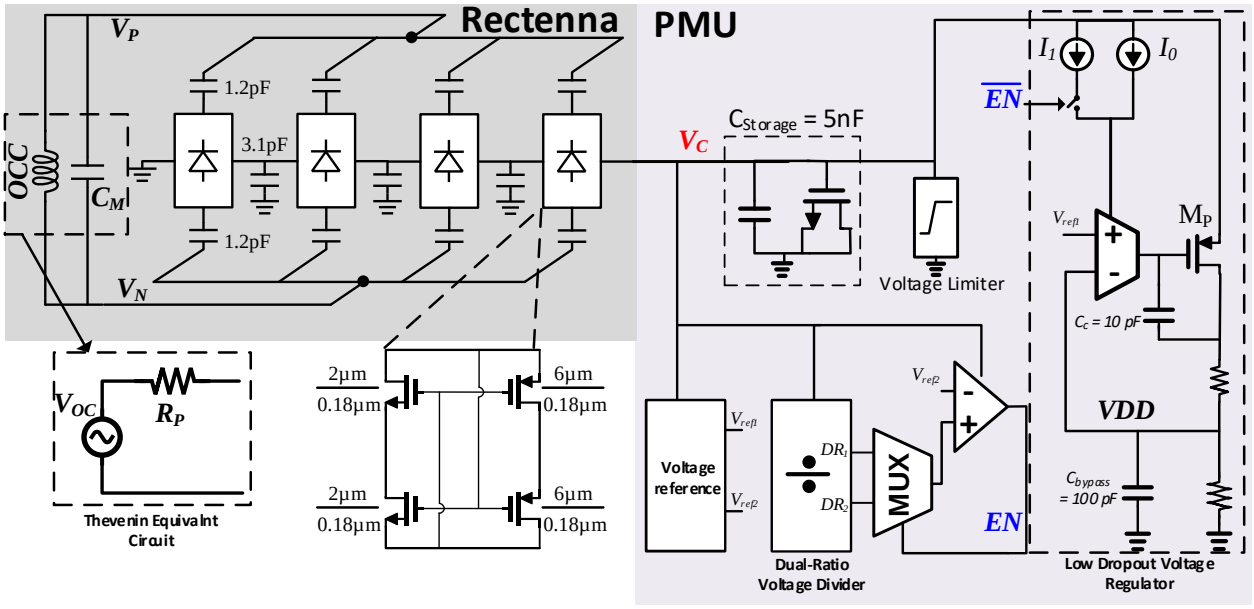

Figure 3.7. Circuit schematic of the power harvesting system.

the LDO. Hence, the abrupt variation of the load leads to a large voltage variation at the output of the LDO. The maximum instantaneous current drawn by the TX block is 4.5 mA which results in a maximum transient voltage variation of 175 mV. Various techniques for enhancing the transient response of an LDO is presented in the literature that require an accurate clock signal to be implemented [76, 77]. To avoid using an external crystal oscillator and to ensure that the LDO remains functional in the active mode, the bandwidth of the error amplifier is increased at the onset of active mode. The PMU adaptively increases the bias current of the error amplifier by 100 μA which enables the LDO to maintain the voltage variation below 12 mV.

3.4.2 Data Receiver Circuit Implementation

The circuit schematic and the timing diagram of the data RX are demonstrated in Fig. 3.8. The RX is implemented based on a self-mixing architecture. The power carrier is modulated with an ASK modulation scheme to carry the DL data stream to the chip. The

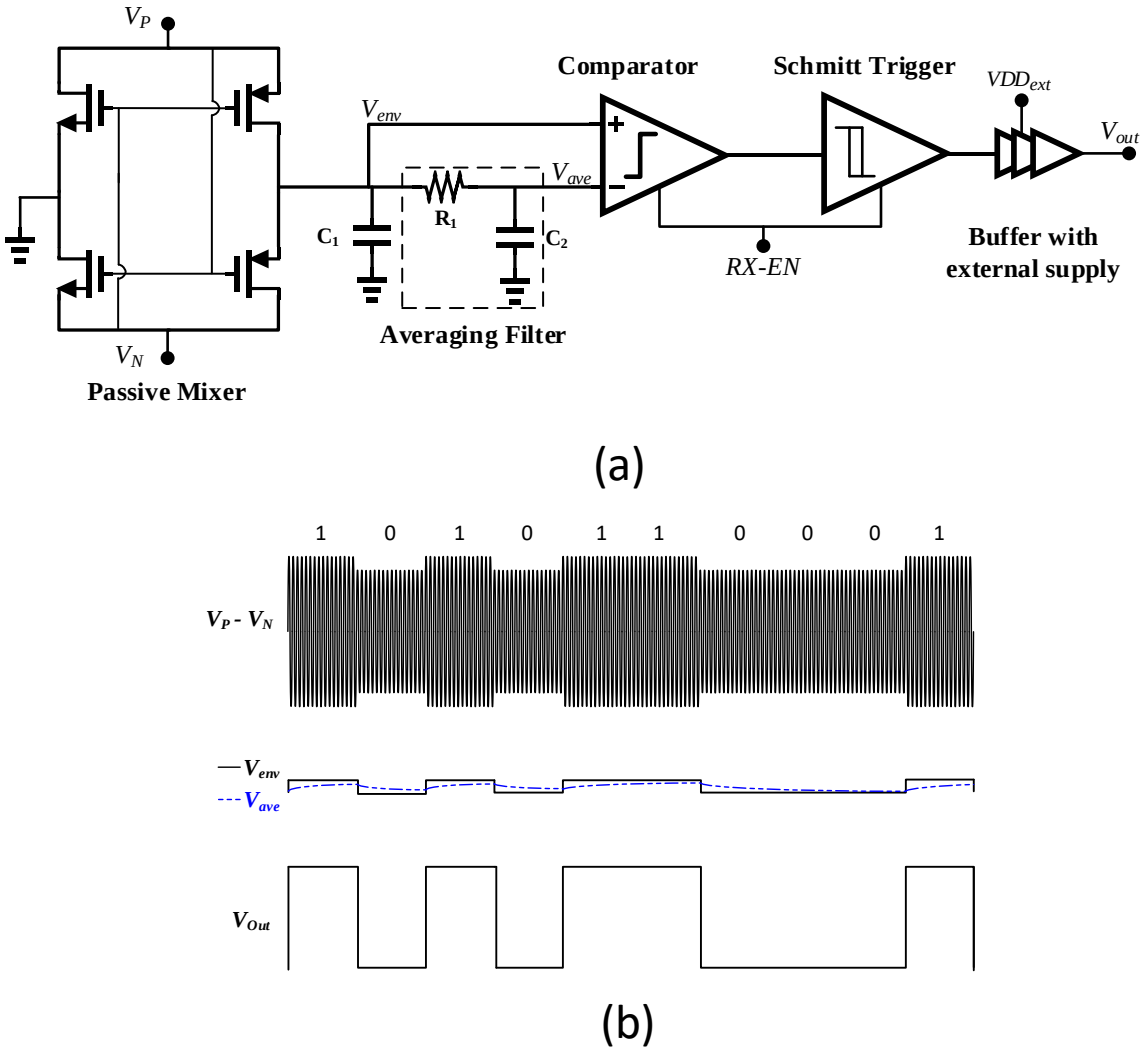

Figure 3.8. (a) Circuit schematic and (b) timing diagram of the ASK data receiver block.

received RF signal by the OCC can be formulated as in (3.1).

$$V_{RF}(t) = V_P(t) - V_N(t) = Acos(2\pi f_{RF} t)[1 + mx(t)] \tag{3.1}$$

Where $x(t)$ and m represent DL data and modulation index, respectively. Data modulation should have a minimal impact on power flow to the chip. Hence, the RX should be able to detect the DL signal with a very small modulation index. A passive mixer is implemented using the same circuitry as a single rectifier stage to minimize the

power consumption of the RX. Inspecting the switching status of the transistors in positive and negative cycles of V_{RF}, shown in Fig. 3.9, reveals that a single rectifier stage can act as a self-mixer. The behavior of the self-mixer can be approximated as the multiplication of a square wave with a frequency of f_{RF} with V_{RF}. Considering only the first harmonic of the square wave, the output of the mixer can be approximated as:

$$\begin{aligned} V_{out} &= V_{RF} \times \frac{4}{\pi} cos(2\pi f_{RF} t) \\ &= \frac{2A}{\pi}[1 + mx(t)](1 + cos(4\pi f_{RF} t)) \end{aligned} \tag{3.2}$$

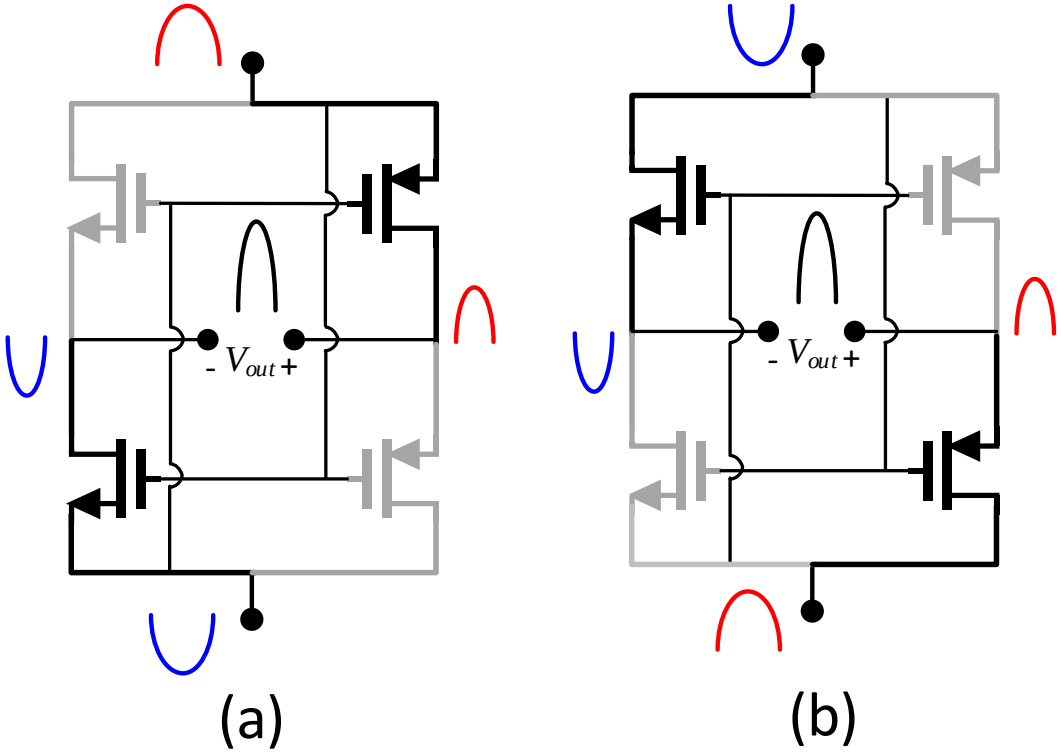

Figure 3.9. Switching status of the passive mixer in (a) Positive and (b) Negative cycles of the input RF signal.

Required data rate for DL communication usually is a few Mbps. Hence, the frequency of $x(t)$ is considerably lower than f_{RF}. In order to extract DL data, the output of the mixer should be passed from a band-pass filter (BPF) to remove frequency components at

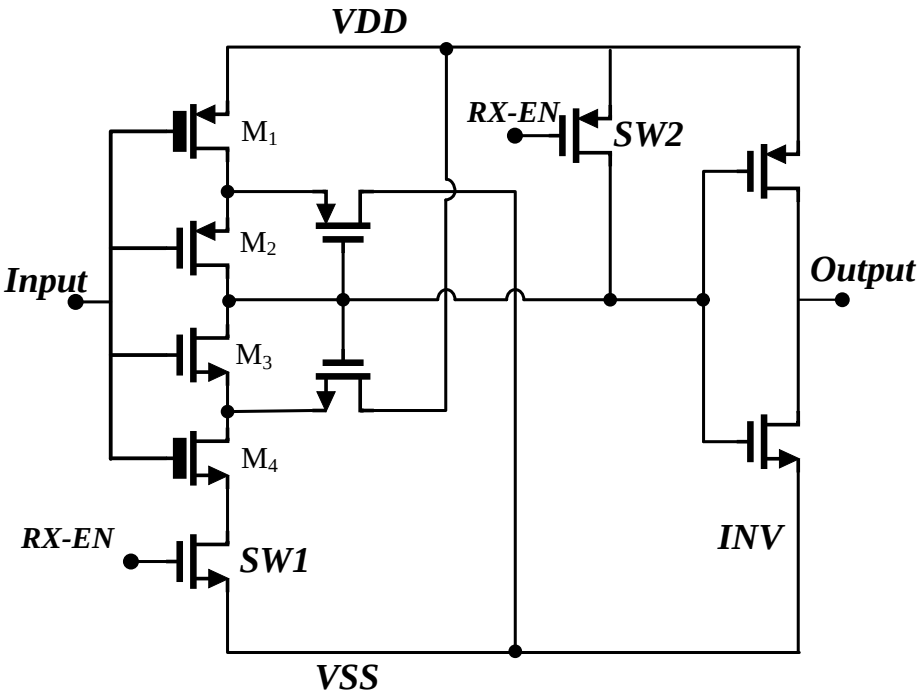

Figure 3.10. Circuit schematic of the Schmitt Trigger in the RX.

dc and $2f_{RF}$ whereabouts. It worth noting that the minimum required voltage amplitude for activating the voltage rectifier in the PMU is 650 mV. Hence, V_{RF} can be directly passed to the mixer with no pre-amplification. Considering the frequency of the DL data, realizing a BPF with on-chip components is not realistic. Hence, the BPF is implemented in three steps using low-pass filters (LPF) and a voltage comparator. The output node of the mixer in Fig. 3.8(a) is connected to a 10 pF shunt capacitor, which forms an LPF with the output resistance of the mixer. The LPF extracts the envelope of V_{RF} that consists of a dc term and $x(t)$, according to (3.1). Next, V_{env} is passed through an LPF that has a cut-off frequency of 160 Hz. Due to the large time constant of the LPF, it acts as an averaging filter and the transition time of V_{ave} is considerably larger than V_{env}. To remove the dc component and retrieve $x(t)$, V_{env} and V_{ave} are passed to the voltage comparator. The simulated small-signal gain of the comparator is 51 dB with a 3-dB bandwidth of 3.8 MHz and a current consumption of 280 nA. As evident in the timing diagram shown in Fig. 3.8(b), if $x(t)$ does

not toggle for multiple consecutive periods, V_{ave} becomes closer to V_{env}. As a result, the comparator will be prone to meta-stability. To ensure that the fidelity of the recovered data is preserved, the comparator is followed by a Schmitt trigger that introduces a hysteresis effect. Hence, V_{out} becomes insensitive to the voltage variation of the comparator in the meta-stable mode. The hysteresis effect also reduces the noise sensitivity of the RX block. The circuit schematic of the Schmitt trigger is demonstrated in Fig. 3.10. Transistors are sized properly to achieve a hysteresis window from 385 mV to 935 mV. The output of the Schmitt trimmer is passed to an on-chip buffer that is powered with an external supply in order to enable a direct connection to a voltage oscilloscope for measurement purposes.

3.4.3 Data Transmitter Design Implementation

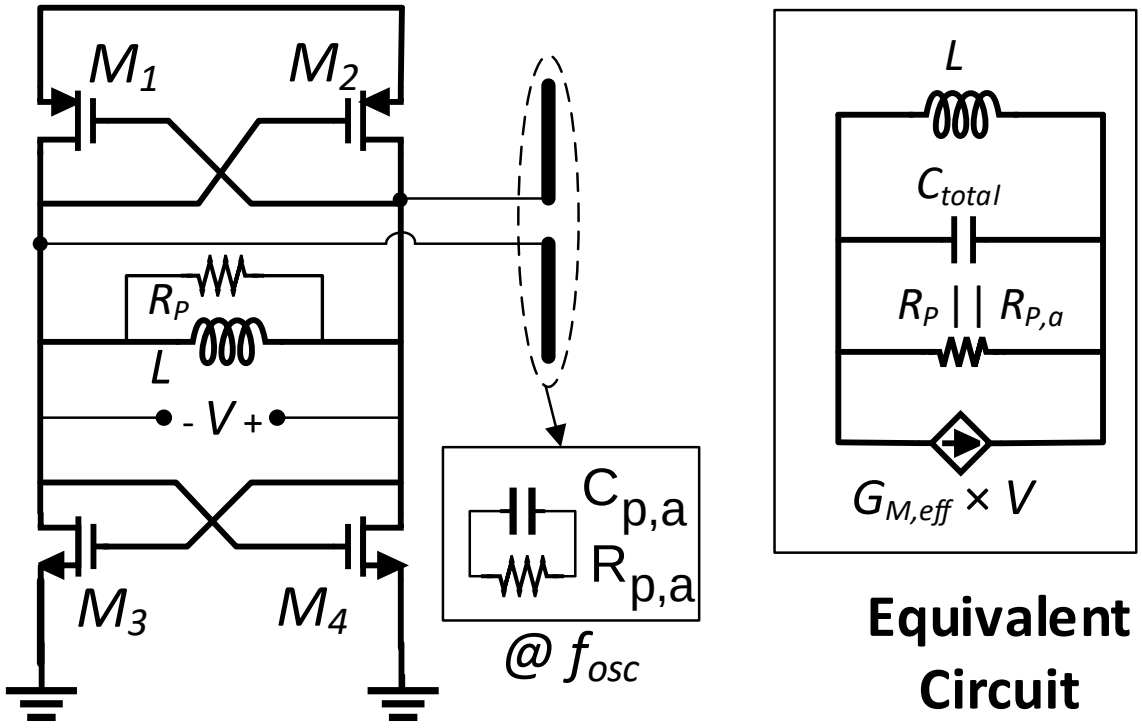

Figure 3.11. Circuit schematic of the power oscillator alongside an equivalent circuit model.

Data communication is the most power-consuming task in the proposed system. Hence,

the TX block is realized with minimal complexity to reduce the overall power consumption. The core of the TX is a power oscillator circuit that is directly connected to an on-chip dipole antenna. At the resonance frequency, the antenna can be modeled by a parallel resistor ($R_{P,a}$) and a shunt capacitor ($C_{P,a}$). An equivalent model for the PO is demonstrated alongside its circuit schematic in Fig. 3.11. The PO is realized with a class-D topology where the tail transistor is removed which results in the elimination of the overhead voltage. Unlike conventional oscillators, transistors in class-D operate as close-to-ideal switches and thus M_1-M_4 are sized properly to guarantee a small on-resistance. Becauase of the high oscillation amplitude, this structure is popular for low-phase-noise and low-power applications [78, 79]. The product of current through MOS switches and the supply voltage is negligible across the oscillation period and the class-D achieves an energy efficiency of 90% [78]. To guarantee reliable startup for the oscillator, the effective transconductance of the complementary switches should overcome the losses of the inductor and the dipole antenna. The startup condition of the oscillator is expressed in (3.3).

$$G_{M,eff} > \frac{1}{R_P} + \frac{1}{R_{P,a}} \tag{3.3}$$

Transistors are sized properly to ensure the startup condition holds up across all technology corners. We have incorporated a complementary pair of NMOS and PMOS switches in the oscillator to reduce the minimum required current for a reliable startup condition through a current reusing technique.

Assuming that the chip is encapsulated by a 200-μm-thick medical grade encapsulation, the dipole antenna is covered by various types of biological tissues with a thickness of 1 cm. The electromagnetic simulation data is used in the circuit model of Fig. 3.11 to evaluate the frequency shift caused by tissue variation. Table 3.1 shows the resonance frequency of the PO exposed to various types of tissues. The oscillator is simulated with a 1.3-V supply voltage assuming all components are in the typical technology corner. The simulation results

suggest a negligible frequency shift.

Table 3.1
CENTER FREQUENCY OF THE POWER OSCILLATOR FOR VARIOUS SURROUNDING MEDIUMS

Medium Type	Air	Skin	Fat	Muscle	Skull
Frequency (MHz)	4248	4218	4232	4226	4223

Thanks to the amplitude-based modulation scheme, the UL communication is not affected by the center frequency shift. Moreover, amplitude-based modulation eliminates the need for an accurate frequency and relaxes the phase-noise requirements to a great extent. Therefore, the PO can be used in the free-running mode, which considerably reduces the circuit complexity and renders additional power saving. The TX block can be configured to conduct the UL communication with either OOK or UWB modulation scheme. The circuit schematic of the reconfigurable TX and the corresponding waveforms in both operating modes are depicted in Fig. 3.12. The trigger signal for enabling the PO is shaped and fed to the TX block according to the modulation type. When operating in OOK mode, the trigger signal replicates the data pattern whereas, in UWB mode, it is shaped as a Return-to-Zero (RZ) waveform for symbol "1" as shown in Fig. 3.12(b). The operating mode of the TX is controlled by an external mode selection signal that alters the signal path from the trigger to the PO.

For OOK mode, the trigger signal is passed to the PO through a pair of transmission gates to control two switches that connect the NMOS cross-coupled pair to the ground. The switches are realized with NMOS transistors and are sized $\times 8$ larger than the NMOS cross-coupled pair. As depicted in Fig. 3.12(a), during transmission of a "1" symbol, the

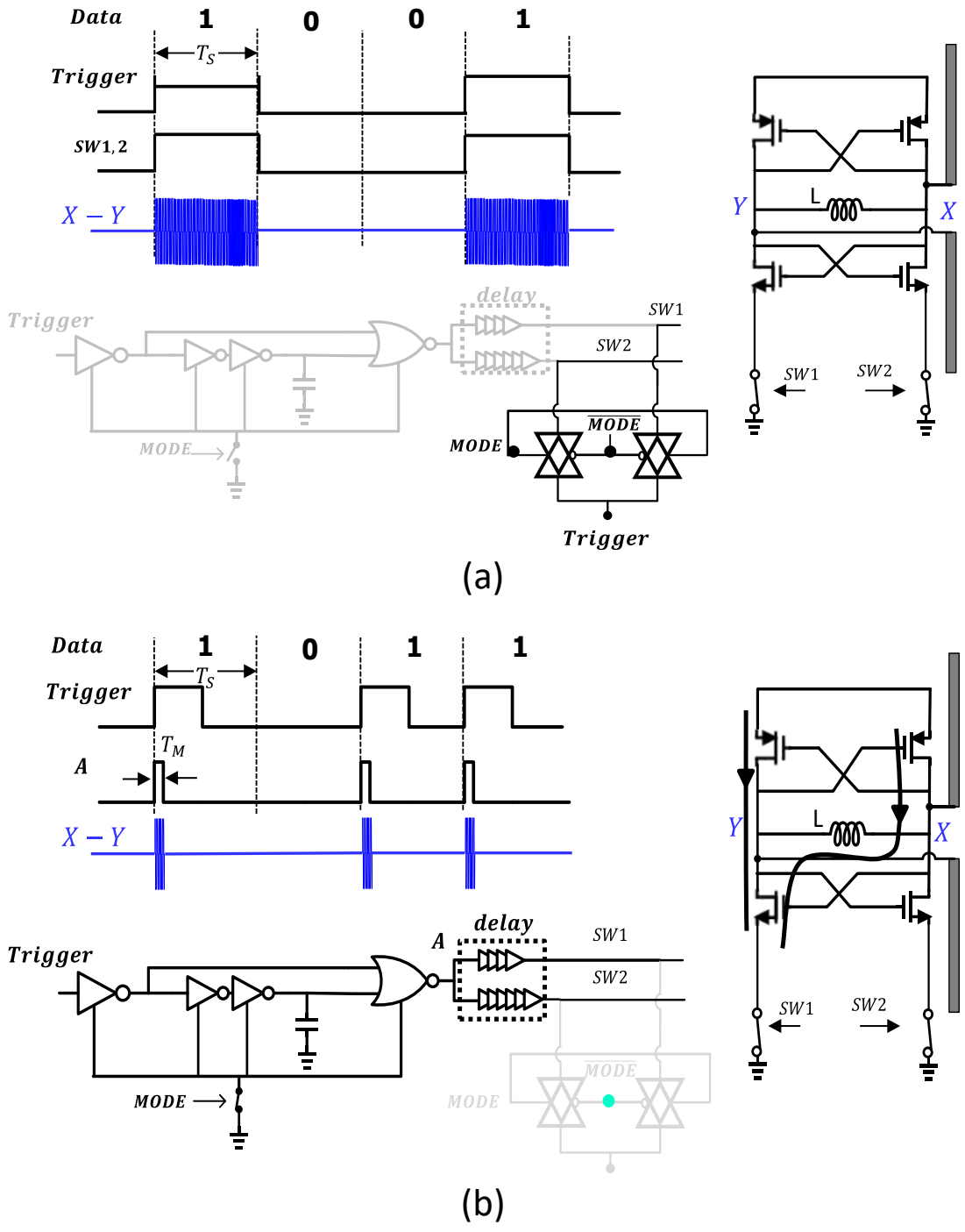

Figure 3.12. Circuit schematic of the power oscillator alongside an equivalent circuit model.

PO is active for the entire symbol period (T_S), which results in smooth switching transitions. Consequently, the transmitted signal from the PO occupies less bandwidth and can be detected with a simpler receiver. However, the average power consumption of the TX block in OOK mode is independent of the data rate and is merely determined by the instantaneous power consumption of the PO. On the other hand, the TX block can achieve a significantly lower average power consumption in UWB modes at the expense of a larger occupied bandwidth. In UWB mode, the trigger signal is first passed through a digital circuitry that generates a 20 ns short impulse upon the detection of a rising edge in the trigger waveform. Due to the small impulse duration, it is imperative to ensure that the PO can reliably startup. Asymmetric driving of an oscillator is a known technique to achieve a fast startup [80, 81]. Therefore generated impulse is delayed by to inverter chain delay lines that connect SW2 slightly after SW1. The current flow during the startup time window through the PO, shown with arrow lines in Fig. 3.12(b), creates an initial voltage difference across node X and Y that results is a startup time of ∼200 ps.

3.5 Measurement Results

The proposed wirelessly powered radio is fabricated in a 180-nm CMOS technology. The annotated micrograph of the chip is shown in Fig. 3.13 and it is evident that the majority of the area is occupied by the antennas and the storage capacitor. The thickness of the die is about 300 μm and the total volume of the design is 2.4 $\times$ 2.2 $\times$ 0.3 mm ^{3}. It worth mentioning that the volume could be further reduced by grinding the substrate of the chip that improves the performance of antennas as well.

The on-chip coil is characterized using a measurement setup shown in Fig. 3.14(a). The resonance frequency of the on-chip coil and a 27 pF on-chip shunt capacitor (C_M) is measured as 278 MHz as shown in Fig. 3.14. However, throughout the measurement, we realized that conducting power transmission at 278 MHz interferes with the performance

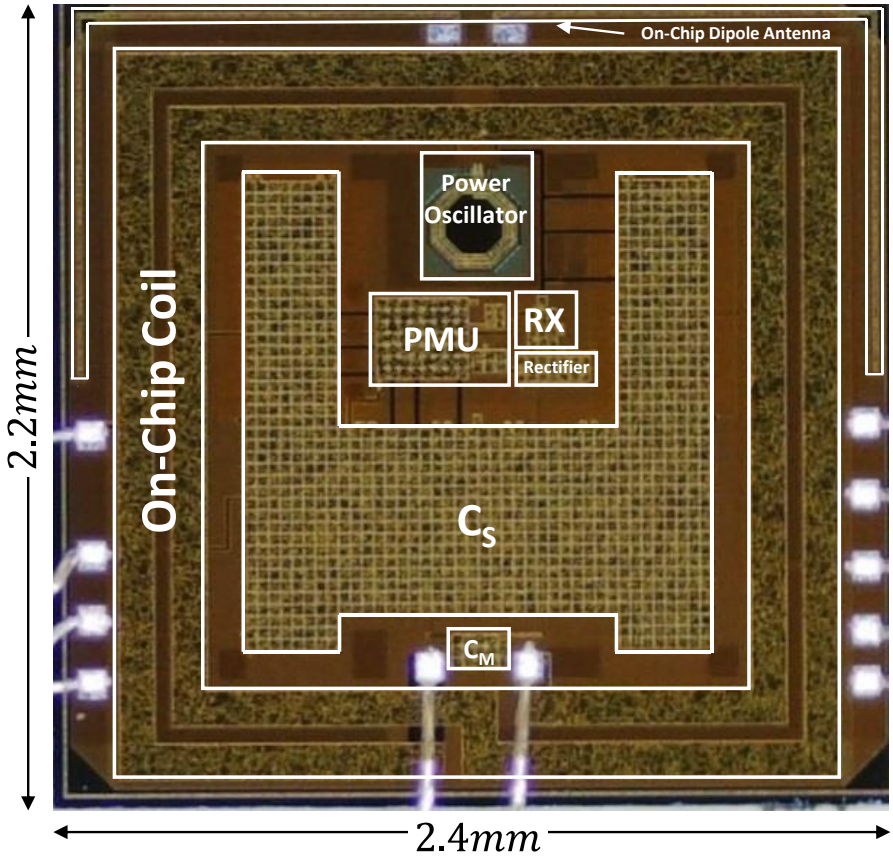

Figure 3.13. Die Micrograph. Die thickness is 0.3 mm.

of the TX block through injection pulling phenomena. The center frequency of the power oscillator is measured as 4116 MHz that is very close to the 15th harmonic of a 278-MHz power carrier. Hence, we decided to lower the power carrier frequency to avoid injection pulling. The carrier frequency is chosen as 250 MHz and the resonance frequency of the OCC is reduced using an external capacitor in addition to the C_M. The required additional capacitor is simulated based on the measured S_{11} as shown in Fig. 3.14(b).

The performance of the wirelessly powered radio is characterized using the measurement setup shown in Fig. 3.15. The power link is mixed with the DL data stream using a coaxial frequency mixer (Mini-Circuits ZX05-1LHW+) and is radiated towards the chip with a custom-built loop antenna that is matched to a 50-Ω source at 250 MHz. The modulation

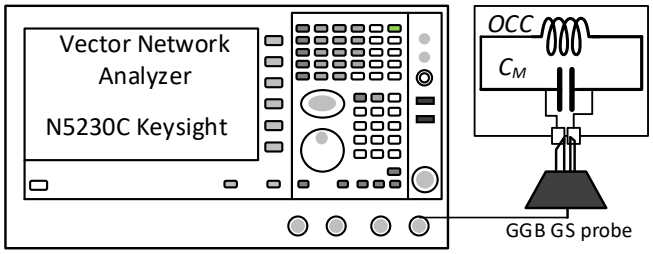

(a)

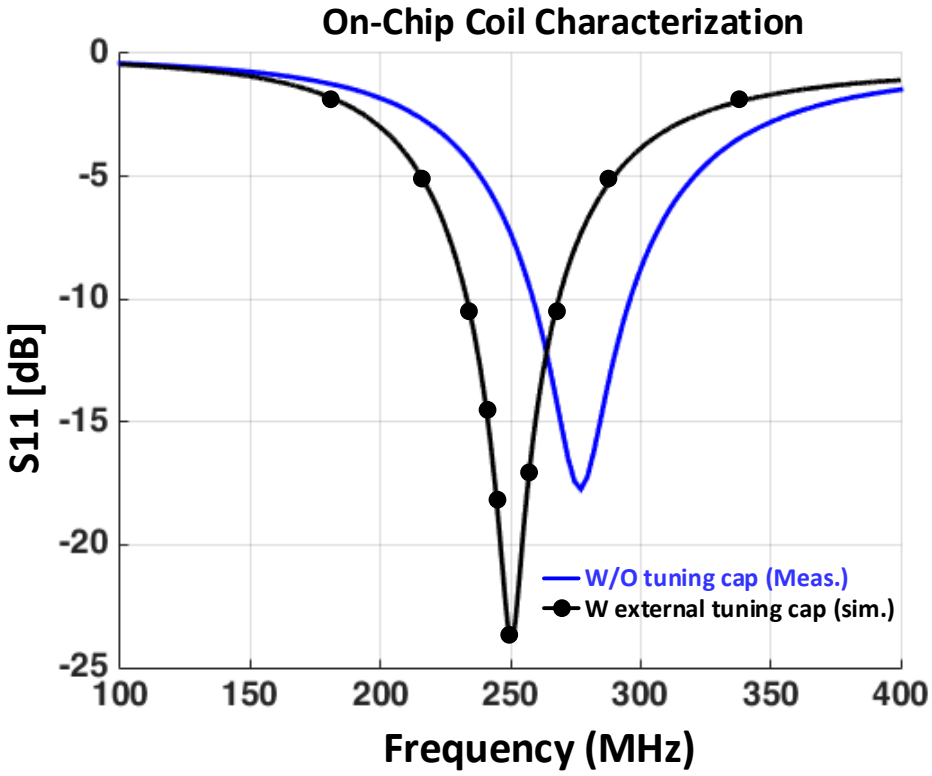

(b)

Figure 3.14. (a) On-chip coil characterization setup. (b) S_{11} before and after tuning.

index is controlled by adjusting the high-level and low-level of the *IF* port of the mixer. The *RF* port of the mixer is passed through an attenuator to ensure the input power level to the following power amplifier (PA) remains lower than the maximum ratings of the PA.

The performance of the RX block is evaluated for various DL data rates. The average transmitted power level from the external loop antenna (P_{TX}) is set to 25 dBm and the

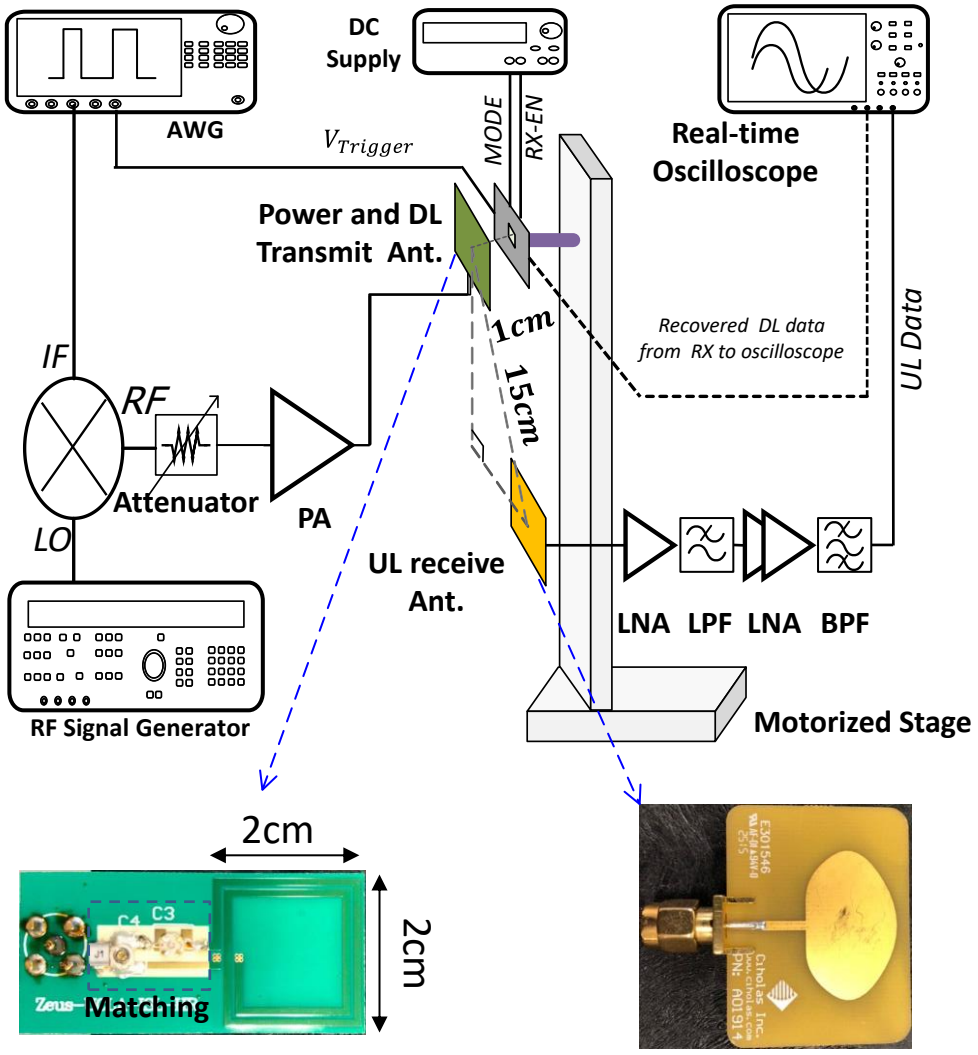

Figure 3.15. Measurement setup for characterizing the wirelessly powered FDD radio.

recovered DL data is shown for data rate values of 1 Mbps and 2.5 Mbps in Fig. 3.16. As the data rate increases, the modulation index should also increase to guarantee reliable data recovery. Measurement results show that the RX block can support a DL data rate of up to 2.5 Mbps at a modulation index of 20%. Also, the power consumption of the RX at 2.5 Mbps is measured as 2.6 μW. Therefore, the RX achieves an energy efficiency of 1.04 pJ/b.

The UL data is received by a monopole broadband antenna with a peak gain of 3.6 dBi (CHICOLAS ANT110). The received signal is then amplified by 52 dB to boost the

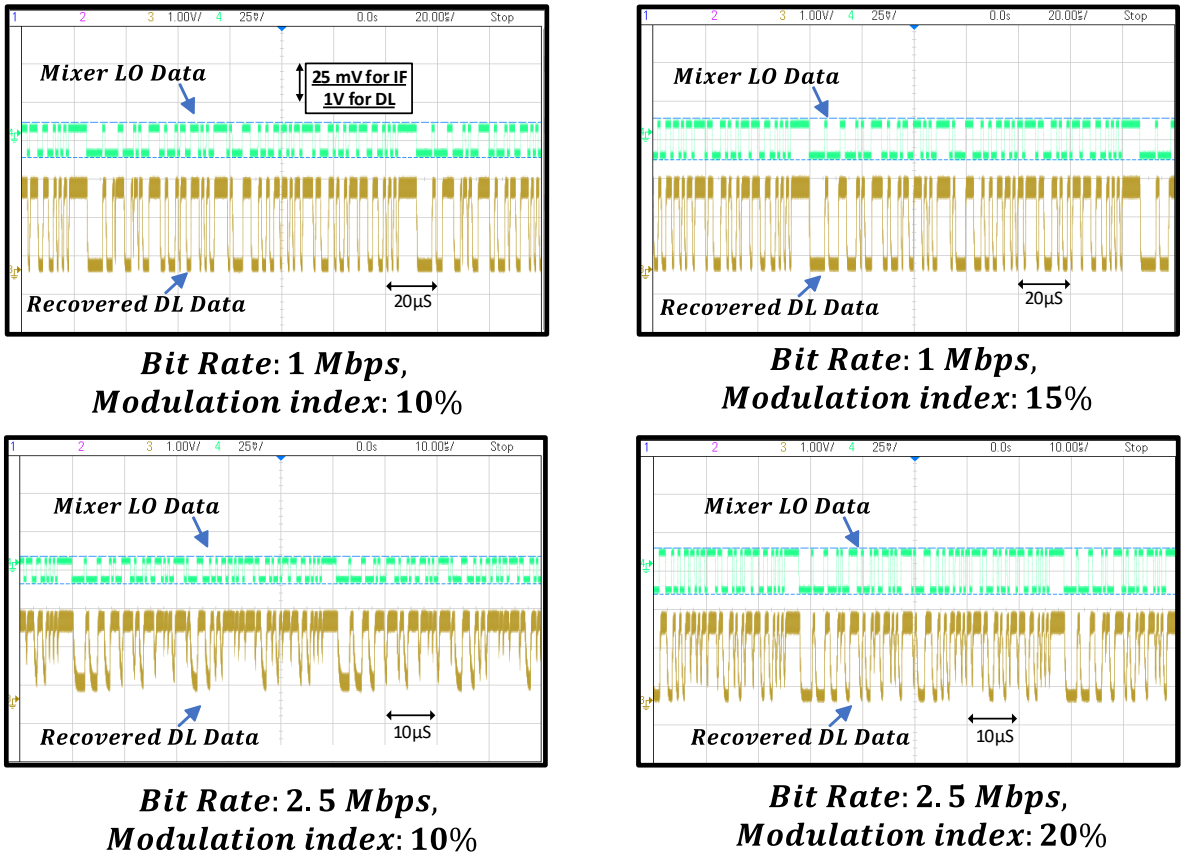

Figure 3.16. Measured transient waveforms of the RX block for various bit rates and modulation indices.

signal level and to enable signal detection with a 50-Ω real-time voltage oscilloscope. Also, external filters are utilized to limit the detection bandwidth and enhance sensitivity. Fig. 3.17 shows the measured spectrum of the received signal by the broadband antenna after the signal is passed through the low-Noise Amplifiers (LNA) and filters (*UL Data*). During this experiment, the power oscillator is powered using a 1.3 V supply voltage to measure the center frequency and the received power level. The power consumption of the PO is measured as 3.73 mW. Besides, simulation results show that the radiated power from the on-chip dipole antenna is about 21% of the total power consumption of the PO. Hence, based on the power gain simulation results in Section III, at a 15 cm distance, it is expected

to receive the UL data with a peak power of −70 dBm. Excluding the additional gain of the components following the monopole antenna, the measured spectrum reveals that the received signal has a peak power of −69.6 dB, which is in a good agreement with the expected value. Also, assuming a 1-GHz detection bandwidth, a minimum SNR of 3 dB, and a noise figure of 3 dB for the LNA, the sensitivity of the UL receiver can be expressed as in (3.4).

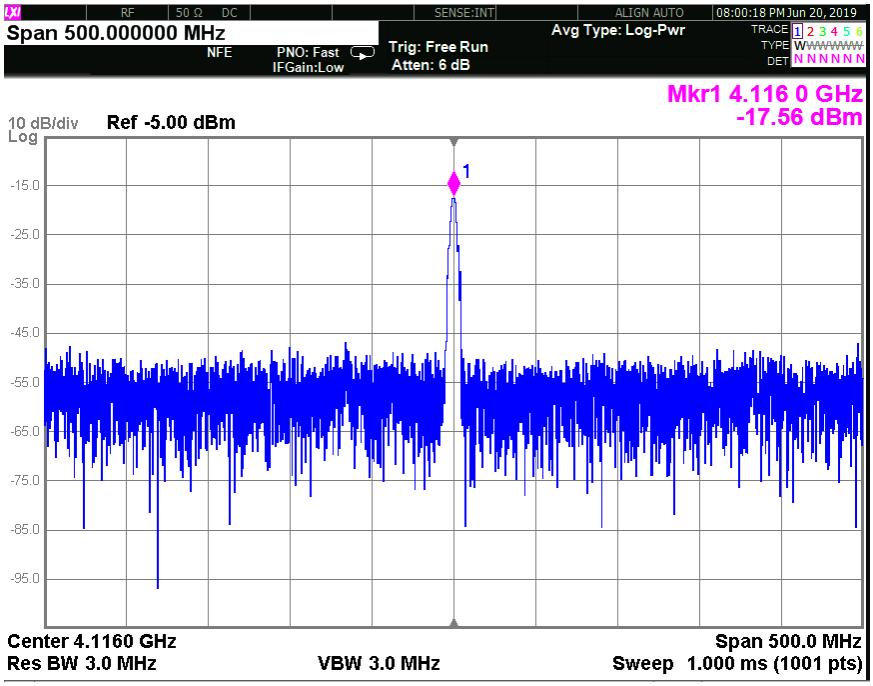

Figure 3.17. Measured spectrum of the amplified PO signal at a distance of 15 cm.

$$UL_{Sensitivity} = -174\,dBm + SNR_{min} + NF + 10 \times log(BW) = -78\,dBm \tag{3.4}$$

To evaluate the performance of the TX block and validate UL communication with wireless power delivery to the chip, the TX block is tested in both OOK and UWB. Measured results indicate that the TX achieves a maximum data rate of 100 Mbps and 150 Mbps in OOK and UWB mode, respectively. Fig. 3.18(a) shows the received UL data with OOK modulation scheme and a data rate of 100 Mbps. The recovered UL data is plotted for P_{TX} levels from 23 dBm to 25 dBm to show the effect of P_{TX} on the performance of the

TX. The same experiment is repeated in UWB mode for a data rate of 100 Mbps and the results are plotted in Fig. 3.18(b). It is evident that for the same P_{TX} level, the charging time of the PMU is almost constant in both OOK and UWB mode. Also, as expected, the TX block consumes less power in UWB mode; and thus the discharge time of the PMU is larger compared with OOK mode. Inspecting the results in Fig. 3.18(a) and Fig. 3.18(b) reveals that the proposed wirelessly powered radio is resilient to available power variation and is able to maintain the UL communication by adjusting the duty cycle of the TX activation. Fig. 3.18(c) shows the recovered UL data in UWB mode for various data rates. The P_{TX} is fixed at 25 dBm and the data rate is swept from 150 Mbps down to 40 Mbps. Since the power consumption of TX in UWB is proportional to the data rate, it is expected that increasing the bit period results in a longer $t_{discharge}$. This fact is reflected in Fig. 3.18(c) and as evident, the TX achieves a continuous operation when the data rate is below 40 Mbps.

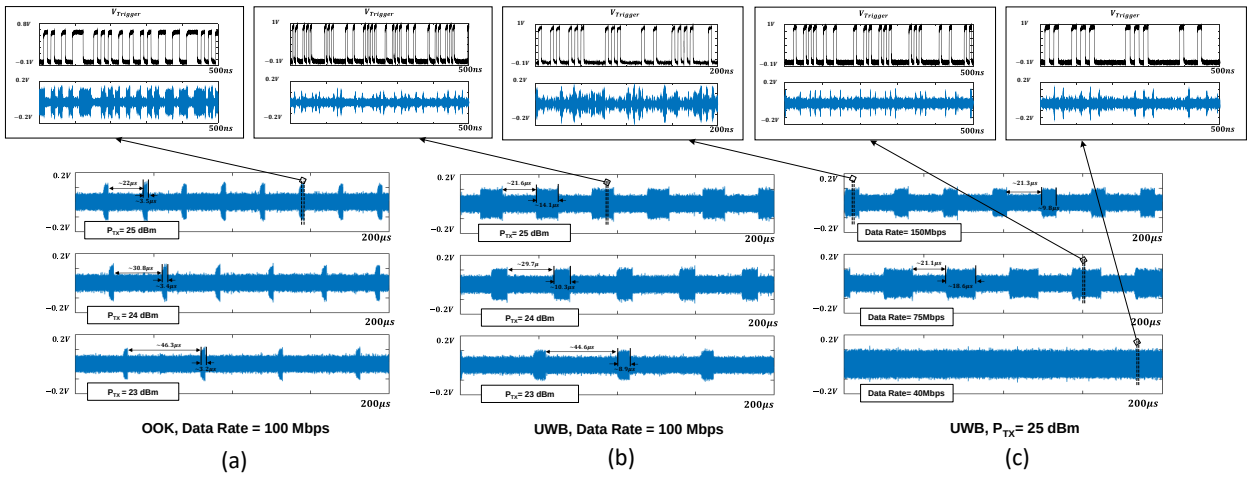

Figure 3.18. Measured recovered uplink data with different TX modulation schemes. (a) OOK, variant P_{TX}. (b) UWB, variant P_{TX}. (c) UWB, variant data rate.

The power contributions of individual blocks are measured for both operating modes of the TX and reported in Fig. 3.19. As expected, the power consumption is dominated by the TX block in both operating modes.

The performance of the proposed wirelessly powered FDD radios is summarized in Table 3.2 and compared with state-of-the-art area-constrained TRXs for medical applications. The proposed radio achieves an UL energy efficiency of 4.7 pJ/b and a DL energy efficiency of 1 pJ/b, respectively. Compared with TRXs that utilize any type of antenna for communication, this work shows a $\times 2.3$ improvement in UL and a $\times 50$ improvement in DL energy efficiency values. Also, this design is the first active radio that is fully integrated and does not require any post-processing or off-chip components, which has resulted in a substantial volume reduction.

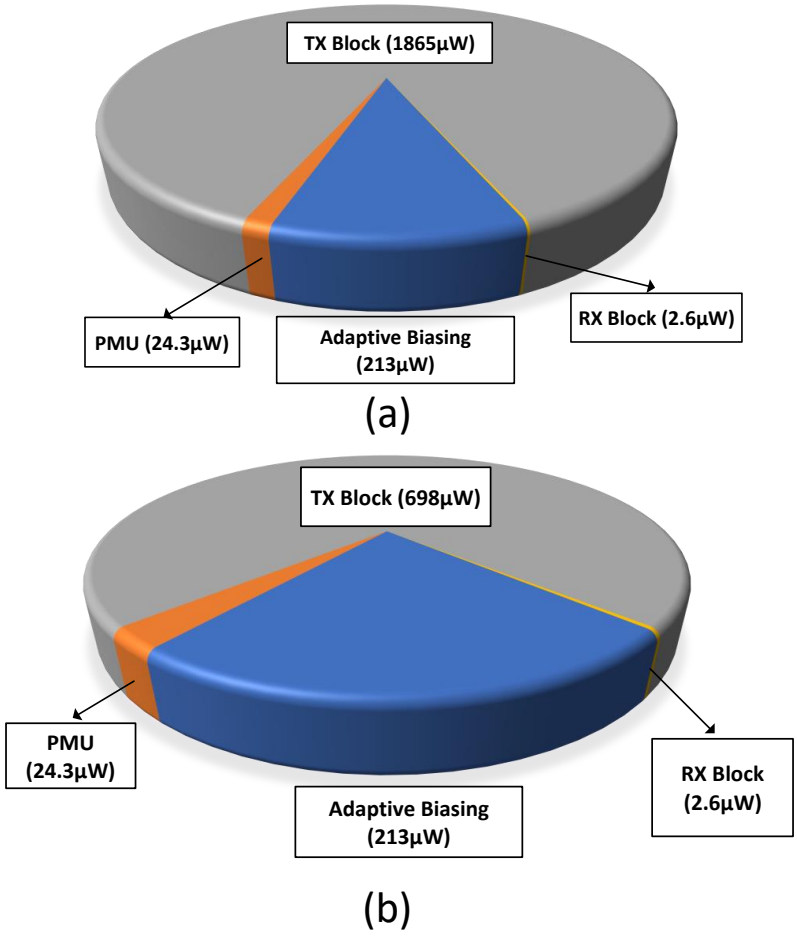

Figure 3.19. Power consumption breakdown of the integrated circuit. (a) TX in OOK mode, data rate = 100 Mbps. (b) TX in UWB mode, data rate = 150 Mbps.

TABLE II
PERFORMANCE SUMMARY AND COMPARISON WITH STATE-OF-THE-ART AREA-CONSTRAINED TRANSCEIVERS

		This Work	CICC '20 [17]	ISSCC '17 [21]	JSSC '17 [22]	JSSC '16 [19]	TBioCAS '16 [20]
Technology		**180nm CMOS**	180nm SOI CMOS	65nm CMOS	40nm CMOS	180nm CMOS	180 nm CMOS
Radio Type		**Active FDD**	Backscatter TDD	Active FDD	Active FDD	Active FDD	Active FDD
Powering Method		**Wireless/ RF @ 250MHz**	Wireless/ RF @ 27 MHz	Wireless/ Ultrasound @ 1MHz	Probed/ RF @ 1.85 GHz	Battery	Wireless/ RF @ 13.56 MHz
TX	**Frequency (GHz)**	**4.12**	0.700	0.0025	1.75	0.112	3.1-7
	Modulation type	**UWB**	LSK	OOK	RZ-OOK	PPM	OOK
		OOK					OOK, BPSK
	Max. data rate (Mbps)	**150**	27	0.1	58	2	500
	Comm. distance (cm)	**15**	0.1-0.25	6	5†	50	1.5
	Power cons. (mW)	**UWB: 0. 698 @150 Mbps**	<2.7	< 0.177	0.093	< 13.6	OOK: 3.5
		OOK: 1.87					OOK-BPSK: 5.4
	Max. energy eff. (pJ/b)	**4.7**	103	NA	1.6	NA	10.8
RX	**Frequency (MHz)**	**250**	700	1	1850	49.86	2400
	Modulation type	**ASK**	ASK	OOK	ASK	OOK	OOK
	Max. data rate (Mbps)	**2.5**	0.00066	0.025	2.5	0.1	100
	Power cons. (µW)	**2.6**	<2.7	NA	7.2	36	5000
	Max. energy eff. (pJ/b)	**1.0**	NA	NA	2.9	360	50
	Comm. distance (cm)	**1**	0.1-2.5	6	5†	20	1.5
Off-Chip Components		**No***	No	US transducer ×2, cap.	Duplexer	Battery, magnetic antenna	Coils ×3, Ant., match. cap.
Volume (mm × mm × mm)		**2.4×2.2×0.3**	2.5×2×0.015**	2.6×6.5×1.8	2×1.6×0.6	10×1×1	30×10×1#

*:Off-chip tuning cap is due to the deviation of implemented OCC from simulation results and can be embedded into C_M in a revised prototype.
**: Thickness is reduced after post-processing and thinning the substrate.
†: Computed based on the transmitted power level and estimated link efficiency.
** Height is estimated based on figures.

3.6 Conclusion

I have presented a wirelessly powered FDD radio with a total volume of 1.6 mm^3, fabricated in TSMC 180-nm CMOS technology. The design enables bidirectional data communication under stringent power budgets of a wirelessly powered medical implant. The IC is entirely powered through a wireless RF link and supports data rates of up to 150 Mbps in the uplink and 2.5 Mbps in the DL paths. Compared with prior-art TRXs that utilize any type of antenna for data communications, the proposed IC advances the energy efficiency for the RX by ×50, and for the TX by ×2.3. Thanks to the power management technique, the proposed design can operate for various data rates and P_{TX} levels. The high

data rate, small form-factor of the IC, and fully-on chip integration of the proposed TRX potentially enables wireless communication for next-generation multi-site neural implants with a large number of recording channels and simulators.

CHAPTER 4

Integrated Wirelessly Powered Chips for IoT and Localization

4.1 Coherent Power Combining with Injection-Locked Synchronized Sensors Nodes

4.1.1 Introduction

Internet of Things (IoT) and its emerging applications have revolutionized wireless sensor networks in recent years. A robust sensor network can be formed by an array of battery-less sensing nodes that harvest energy from the environment. These self-powered nodes provide unprecedented opportunities in many applications such as environmental sensing and medical implants [21, 82, 83]. These sensors will not require battery placement and can operate for a long time in harsh environments. In many applications, the nodes need to be millimeter-sized while capable of carrying complex functions under severe power budgets. They need to be able to perform energy harvesting, low-power sensing, and wireless communication. Radio Frequency Identification (RFID) systems have shown great potentials for addressing the main requirements of a sensing node and are widely adopted in Wireless Sensor Network (WSN) systems. [84, 85]. However, traditional battery-less sensor nodes such as RFID tags utilize large antennas and harvest energy through either a near-field or a far-field wireless link [40, 86, 87]. They also rely on backscattering techniques for data communication [88, 89].

Miniaturization is an imperative step towards future ubiquitous sensor nodes which

imposes serious challenges on power delivery and data communication. With recent advances in semiconductor technology, incorporated electronic parts of an RFID tag can be integrated with a compact form-factor and the overall dimension of the sensing node is dominated by the size of energy storage components and antennas. As the size of the power harvesting antenna is reduced, the power transfer efficiency degrades, and the harvested power decreases. Hence, a stronger power carrier is required to activate wirelessly powered sensor nodes. On the other hand, backscattering communication relies on load modulation of the power harvesting antenna. In mm-sized RFID tags, load modulation results in a reflected signal at a frequency very close to the power carrier. Also, due to the small size of the antenna, load modulation fails to establish a distinguishable difference in the reflected pattern [90]. Hence, detecting the reflected signal at the presence of a large power carrier demands very large isolation and imposes stringent linearity requirements on the RFID reader, which is not often realistic. Active communication techniques, on the other hand, address the sensitivity issue of backscattering tags since the frequency of power carrier and communication links can be sufficiently separated from each other. However, similar to backscattering techniques, miniaturization degrades the power transfer efficiency and affects the performance of data communication antennas. Therefore, research trends in mm-sized sensor nodes have been focused on the design of ultra-low-power and energy-efficient data transceivers to address the requirements of future IoT devices. [1, 68] .

The development of millimeter-scale microchips will benefit many applications and industries. For instance, battery-less mm-sized system-on-chip (SoC) devices can revolutionize the US energy industry by enabling novel mapping and localization techniques. Currently, in the US, a large number of hydraulic fracturing is performed to extract oil and gas from tight reservoirs. Many of these expensive fracturing jobs result in no improvement in production efficiency due to the lack of techniques to monitor the fractures and image their geometry. The development of a mm-sized SoC sensing node enables a robust WSN system since it significantly reduces the overall cost and improves

sensor density rendering high-resolution mapping [19, 32, 63]. In recent work, we demonstrated that low-cost integrated microchips that are millimeter-scale and wirelessly powered can be used in large quantities to provide a map of fractures. [91, 92]. The microchips can be mixed with propellants and sent to fractures during hydraulic fracturing. This concept is illustrated in Fig. 4.1, where a downhole tool is used to provide wireless power to the miniaturized chips and receives the reflected data back from the chips. By moving the downhole tool in a wellbore and repeating the measurement, it is possible to calculate the location of the microchips and perform fracture mapping by adopting proper localization algorithms [93, 94]. One of the parameters that determine the localization accuracy is the Signal-to-Noise (SNR) ratio of the received signals. On the other hand, the signal radiated from a single microchip is weak, which limits the operating distance of a microchip and the efficacy of localization algorithms, consequently.

The main contribution of this chapter is proposing a novel coherent power combination technique through injection-locked distributed sensor nodes. The localization algorithm that can be built on the proposed platform is open to the user's choice. Generally, the achievable end-to-end resolution is an artifact of the capability of individual sensor nodes as well as the algorithm in use. The later falls beyond the scope of this work. In this section, we present a novel method to increase the operating range by forming a synchronized array of microchips that collectively produce strong coherent radiation back to an RF receiver. This section is based on my recent paper that is published in IEEE Sensors Journal [95]. I demonstrate a proof-of-concept by a coherent array of 2×2 nodes fabricated in 180-nm CMOS SOI technology. The rest of the section is organized in the following manner. In subsection 2, we review the bases of the Multiple Signal Classification (MUSIC) localization algorithm as a well-known localization algorithm based on the detection of Direction of Arrival (DoA). The effect of received SNR on the performance of MUSIC algorithm is demonstrated to highlight the importance of high SNR in a distributed sensor network for localization purposes. In subsection 3, we provide an overview of the proposed distributed system and discuss the

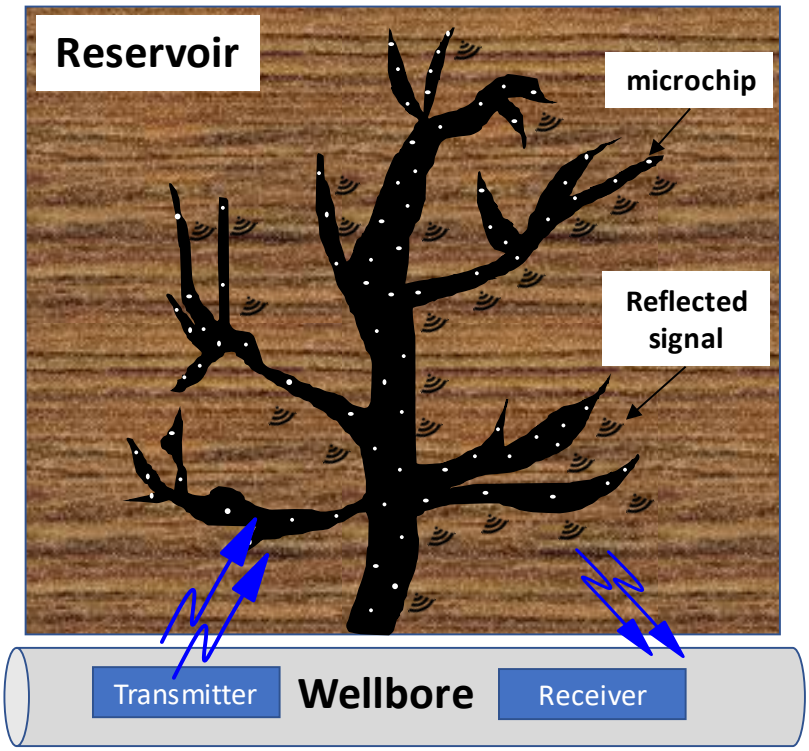

Figure 4.1. Fracture mapping: an exemplary application enabled by distributed miniaturized sensing nodes.

operating principles. Subsection 4 focuses on the design details and architecture of the integrated SoC for each sensing node. Experimental results are explained in subsection 5 and finally, the section is concluded in subsection 6.

4.1.2 Discussion on Localization Algorithms

Estimating the location of distributed sensors is essential in WSNs. Localization techniques based on the detection of DoA, Time of Flight (TOF), or Received Signal Strength (RSS) have been adopted to estimate the position of sensors in a distributed WSN system [96]. Specifically, MUSIC is a popular algorithm for estimating the DoA and is a powerful tool for processing the received signals radiated from different signal sources in order to extract the intended signal in the presence of interference and noise [97, 98]. In

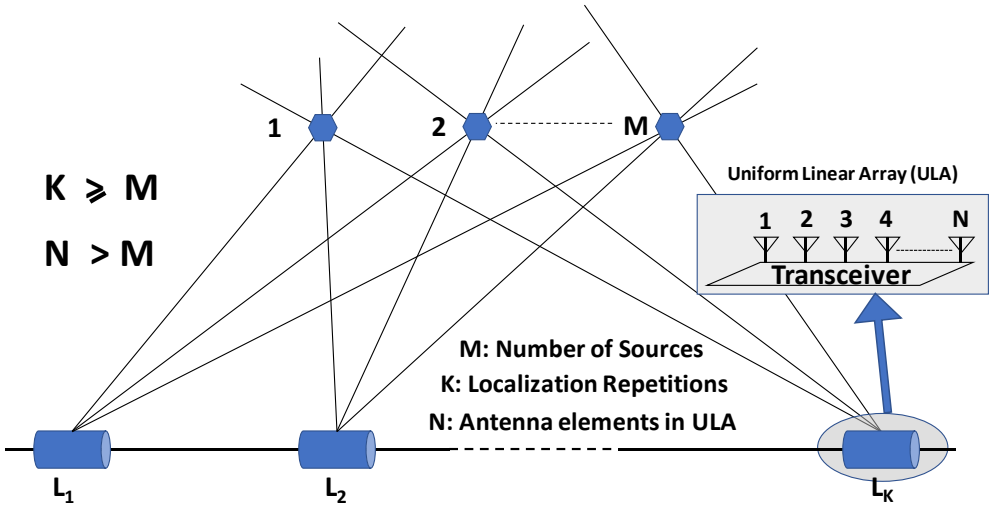

Figure 4.2. Illustration of the MUSIC localization algorithm through multiple repetitions of DoA estimation.

principle, MUSIC relies on the received phase over an array of antennas to detect the DoA. Thus, the detection resolution depends on the number of elements in the antenna array. Besides, the positioning accuracy of phase-based localization techniques can be enhanced by repeating the experiment at multiple frequencies to alleviate the effect of multi-path reflection. The operating frequency alters the path loss and antenna efficiency. Hence, an optimal selection of the frequency results in the maximum received SNR and enhances the accuracy, consequently.

In MUSIC algorithm, we consider the measured signal by an N-element antenna array as a vector in N-dimensional space. The N-element vector is used to form a correlation matrix to estimate the spatial spectrum of the received signals. The MUSIC algorithm is capable of detecting M independent signal sources ($M < N$) by applying an eigendecomposition technique on the correlation matrix to estimate the spatial spectrum. The spatial spectrum represents the distribution of signal sources in every direction in the space. Hence, it can result in DoA estimation. The MUSIC algorithm also fits very well with fracture mapping applications as the antenna array can be swept along the wellbore

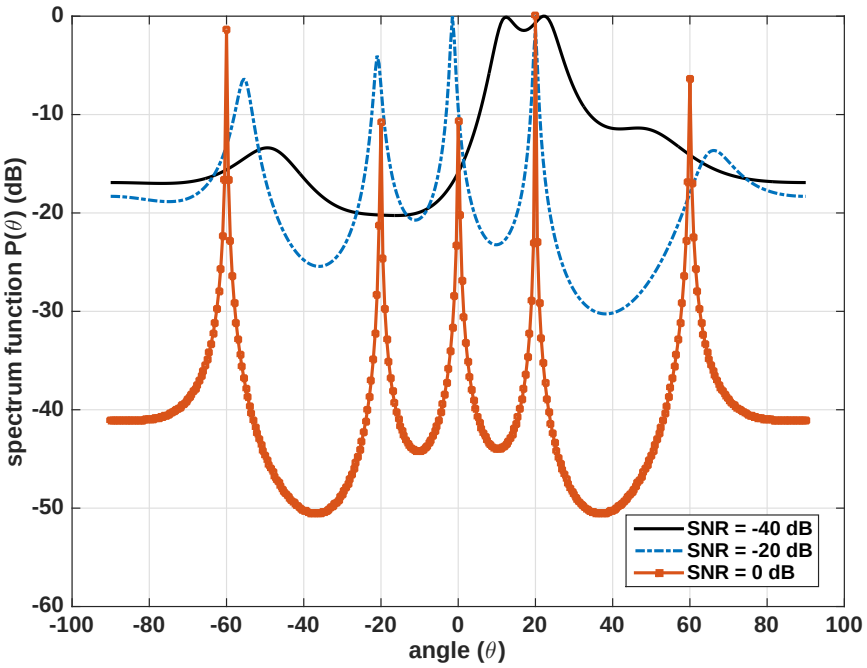

Figure 4.3. Effect of SNR of the received signal on the performance of the MUSIC localization algorithm. Five independent sources are localized by a six-element antenna array.

to repeat the DoA estimation. Besides, the Uniform Linear Array (ULA) of antennas can be implemented as a Synthetic Aperture Radar (SAR) with only two physical antennas [99]. Utilizing a SAR architecture for antenna array significantly reduces the complexity of the transmitter in the wellbore. It should be noted that the main drawback associated with the MUSIC algorithm is the large computation power which is not a significant concern in fracture mapping applications.

It can be proven that M independent signal sources can be uniquely positioned by repeating the DoA estimation M times and intersecting the connecting line from the center of the antenna array as shown in Fig. 4.2. Each hexagonal shape in Fig. 4.2 represents an independent signal source which is composed of several microchips forming a unified cluster. Aside from localization purposes, the microchips can also be equipped with

additional circuitry to enable environmental parameter sensing which is an interesting topic for future WSN sensing nodes. The maximum distance of microchips within a specific cluster is formulated in Section III. Since the ULA is located at different distances to the clusters, the received signal from each cluster arrives with a different phase and thus the clusters can be considered as independent signal sources. It is worth mentioning that multiple modified MUSIC algorithms are proposed to alleviate the challenges of correlated signal sources [100, 101]. Also, it is often assumed that the propagation medium is homogeneous. The challenges of MUSIC localization in an inhomogeneous medium and the potential solutions are discussed in detail in [102, 103]. Technical details and problem formulation of the MUSIC algorithm can be found in [97, 104]. It has been shown that the resolution and the accuracy of the MUSIC algorithm are highly impacted by the SNR ratio of the received signals. I have adopted the same procedure as [104] and have plotted the estimated DoA for a six-element array when five nodes are uniformly distributed within a range of -60° to -80° range with a step size of 20°. The plotted results in Fig. 4.3 reveal the importance of SNR in MUSIC-based localization. Achieving an acceptable SNR value from a single wirelessly powered microchip is not feasible. Therefore, we have proposed a coherent power combination technique to address this problem.

4.1.3 System Overview

The proposed system incorporates multiple mm-sized microchips as sensing nodes, fabricated in a 180-nm CMOS SOI process. The microchip design and implementation were previously reported in [105]. Each microchip is equipped with a wireless power harvesting system and an on-chip oscillator. The concept of the distributed system is shown in Fig. 4.4 where multiple microchips are used as individual nodes to form a distributed sensor network. The proposed network can be used for localization purposes by detecting the microchips that are placed on the sensing premises. In this localization technique, the reader is placed in the operating region of a sensor node and activates the

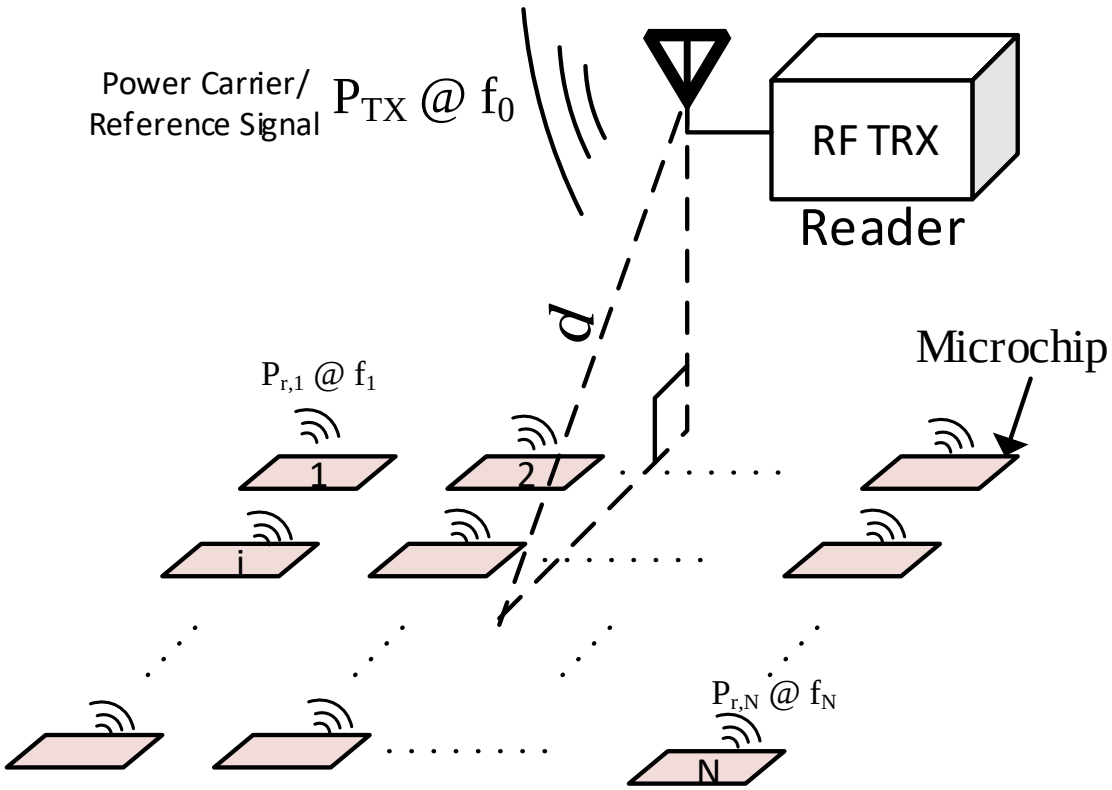

Figure 4.4. The proposed concept of a distributed WSN based on mm-sized wirelessly powered microchips.

node in its proximity. The transmitted power from the reader (P_{TX}) serves two important goals in this system. First, it is the main source of power to activate the microchips. Second, it can be used as a reference signal to synchronize the reflected tones from all microchips. Upon activation, each node reflects another RF signal to the reader. The reader scans the premises and detects placement pattern by receiving signals from the nodes at different spots. The total received signal at the reader is the combination of each signal reflected from individual nodes and can be formulated as:

$$V_{RX}(t) = \sum_{i=1}^{i=N} A_i cos(2\pi f_{r,i} t + \phi_i) \tag{4.1}$$

Where A_i, $f_{r,i}$, and ϕ_i represent amplitude, frequency, and phase of the reflected signal

from i-th element, respectively; and N is the total number of microchips. In our previous work, we have demonstrated that the frequency of the RF tone radiated back from the microchip can be precisely set to half of the power carrier frequency (f_0) [105]. Therefore, we can assume the frequency of radiated signals from the microchip is set to $f_0/2$ in the presence of a power carrier at f_0. A group of adjacent nodes that are approximately at an equal distance from the reader is considered as a unified cluster. Hence, the received signals from all sensor nodes within a cluster arrive at the reader with the same phase. When a large number of microchips are placed in a cluster, they are aligned randomly and the received signal from each microchip at the reader depends on the microchip alignment. For simplifying the analysis and without loss of generality, we assumed that all the microchips are aligned with the reader antenna. Under these assumptions, the radiated signals from microchips with the same cluster will add up coherently and the received signal can be re-written as:

$$V_{RX}(t) = N \times Acos(2\pi f_r t + \phi) \tag{4.2}$$

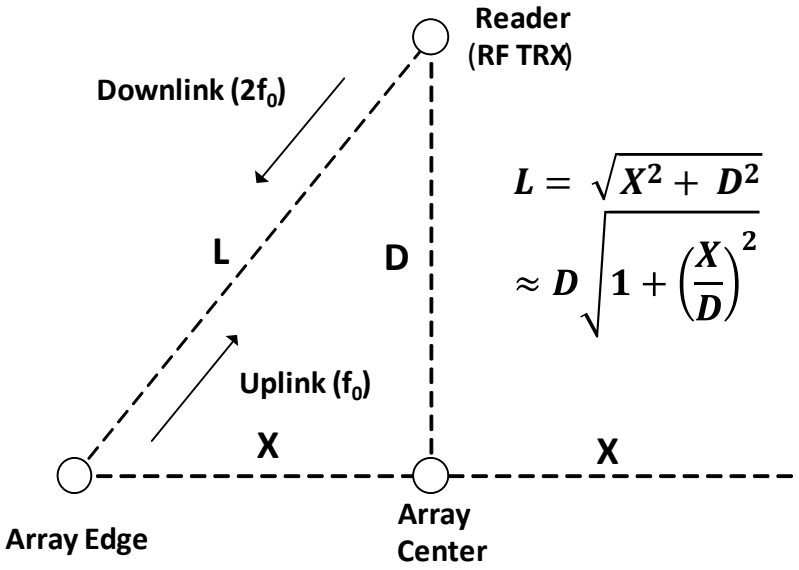

Figure 4.5. Linear sensor array configuration.

Eq. 4.2 implies that if all received signals are in-phase and have the same frequency and they all add up constructively. As a result, the amplitude will be amplified by a factor of N and the received power is multiplied by N^2, consequently. Therefore, a distributed sensor network can resemble the behavior of a phased-array antenna [106]. Radiated power form an individual element is usually is less than a milliwatt. This weak radiated signal experiences a relatively large attenuation due to the path loss. As Eq. 4.2 suggests, the received power can be amplified by increasing the number of elements in the distributed sensor network if all nodes reflect an RF signal with the same frequency and phase. For example, if we use 1000 coherent nodes, the received power at the reader will be amplified by a factor of 1,000000.

To ensure the negligible phase shift assumption between the sensor nodes within a cluster, the maximum span of the array should be limited. To calculate the maximum array span, we define the maximum allowable phase shift in a linear array as the phase shift that results in a 3 dB power loss in the combined power from the sensor at the center of the array and the sensor at the edge. A similar approach can be used for 2D and 3D arrays as well to calculate the maximum span. The configuration of a linear array is illustrated in Fig. 4.5. With the defined metric, the maximum phase shift is calculated as 90° according to the following equation:

$$\frac{\sqrt{A^2 + A^2 + 2A^2 cos(\phi_{max})}}{2A} = \frac{\sqrt{2}}{2} \tag{4.3}$$

Considering that the reference signal experiences the same path difference in downlink at a frequency twice as the uplink, the maximum allowable phase difference should be limited to 30° to satisfy (4.3).

The maximum array span ($2 \times X$) can be computed for a given wavelength (λ), maximum phase shift (ϕ_{max}), and reader to array center spacing (D) according to the following equation:

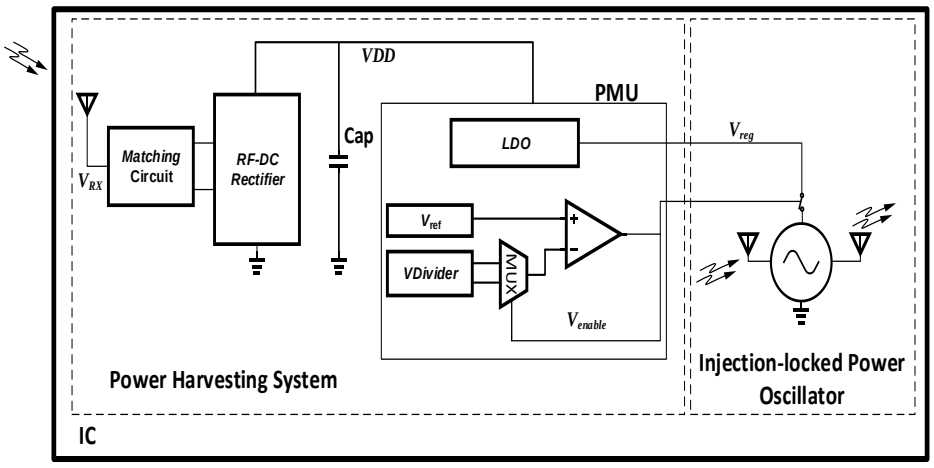

Figure 4.6. Block diagram of the integrated microchip used as an individual node in the proposed distributed sensor network.

$$X \leq \sqrt{\frac{\phi_{max} \times \lambda \times D}{180}} \tag{4.4}$$

4.1.4 Microchip Design and Implementation

To address the practical challenges of a WSN system, we have implemented a microchip that is compatible with the power budget requirements of a wirelessly powered system. The block diagram of the proposed microchip is illustrated in Fig. 4.6. Three on-chip dipole antennas are incorporated in this design. One antenna is used for receiving RF energy from an external reader. The incoming RF wave is also fed to another antenna to enable sub-harmonic injection locking that is described later in this paper. The third antenna is used to transmit the reflected signal from the microchip to the reader. The microchip includes a power harvesting system to enable wireless power transfer and battery-less operation. Harvested power is often less than the instantaneous power consumption of the incorporated circuity in the microchip. To address this problem, a power management unit is included in the power harvesting system to duty-cycle the operation of communication circuits to lower the overall power consumption [47, 61]. The transient voltages of the PMU that are

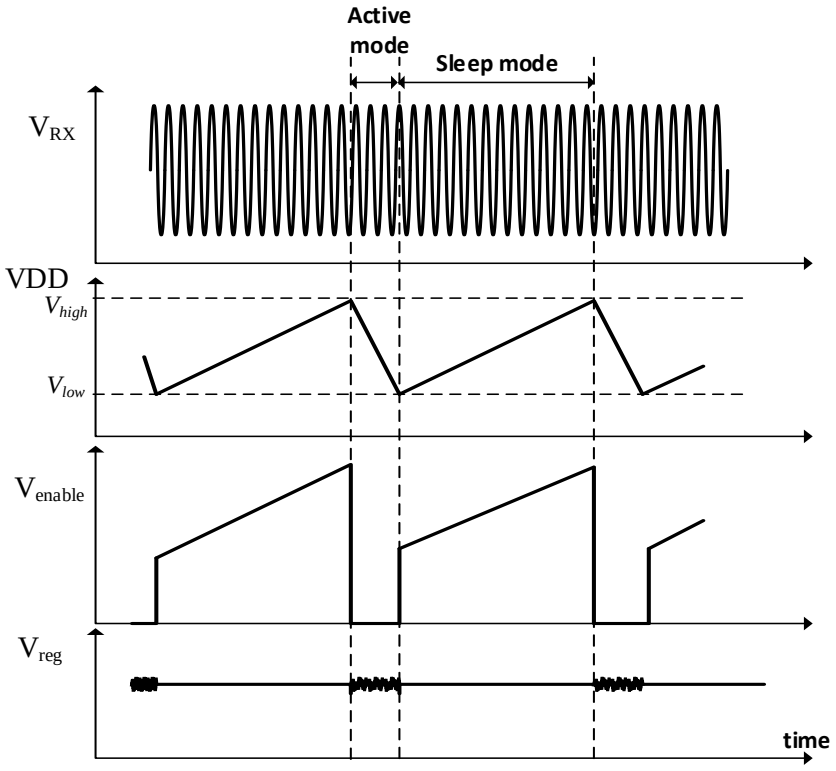

Figure 4.7. Transient timing diagram of the internal nodes in the power harvesting system during active and sleep modes.

demonstrated in Fig. 4.7 indicates how the operation is divided into sleep mode and active mode.

The antenna for power delivery is modeled with the silicon substrate and simulated in IE3D software [41]. The received power by the microchip can be formulated according to the Friis equation and is expressed as (4.5). Simulated results show that for a 1W EIRP transmitted power level and spacing of 5 cm, about 800 μW is received by the on-chip dipole antenna at 8 GHz. Hence, operating frequency for power transmission is chosen to be around 8 GHz to maximize the link efficiency.

$$P_{RX} = \frac{P_{TX} \times G_{TX} \times G_{RX} \times \lambda^2}{(4\pi d)^2} \tag{4.5}$$

The on-chip dipole antenna is matched using a 3.4 nH inductor that resonates with its impedance. A multi-stage voltage rectifier follows the antenna to convert sinusoidal signals to a dc voltage as shown in Fig. 4.8. The minimum power required for the voltage rectifier to generate a 1 V output dc voltage across the 1.1 nF MIM capacitor is −16.1 dBm [107]. The rectifier output voltage has many high-frequency ripples and varies with different loads. Hence, a low-dropout voltage regulator (LDO) follows the rectifier to generate a stable dc voltage for the data communication circuitry.

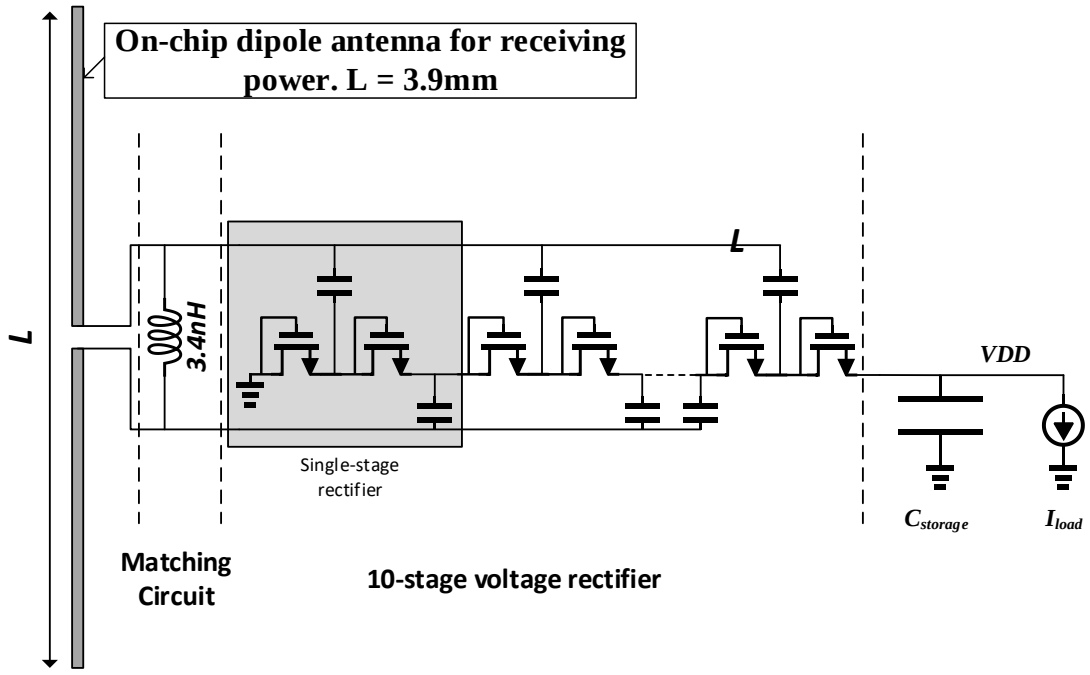

Figure 4.8. Circuit schematic of the 10-stage voltage rectifier connected to the on-chip dipole antenna with a matching circuit.

Signal reflection is carried by a transmitter block which is implemented based on a power oscillator (PO) architecture where a voltage-controlled oscillator (VCO) is directly connected to the antenna [1]. A PO-based transmitter does not require additional power-hungry circuitry such as a power amplifier or a buffer and results in minimal power consumption. The circuit schematic of the injection-locked VCO is illustrated in Fig. 4.9.

The VCO is implemented using a cross-coupled pair of NMOS devices and the operating frequency is determined by the resonance frequency of the LC tank. However, due to process and temperature variation, the operating frequency may drift. In addition, the phase of the output signal is ambiguous. Therefore, reflected signals from the microchips have different phase and frequency and do not add up constructively. The remedy to this artifact is to stabilize the operating frequency of the VCO. A conventional method for achieving an accurate frequency is to place the VCO in a phased-lock loop (PLL) [108]. This method is not a practical solution for our system for the following reasons: 1- PLL-based frequency stabilization requires an accurate frequency reference that is often provided by a crystal oscillator. The idea of using an off-chip large component contradicts our initial goals of cost reduction and form-factor miniaturization. 2- Although a PLL-based approach results in an accurate frequency, it does not guarantee that all the VCOs are operating with the same phase since the reference frequency, provided by the crystal oscillator, could have different phases. 3- Generally, PLLs are power-hungry and do not fit well with the available power budget of an energy harvesting microchip.

Sub-harmonic injection locking is a promising solution for achieving synchronized reflected signals and is even practical for pulse-based high-frequency systems [105, 109]. In this method, the transmitted power form the reader is utilized as a reference signal for injection-locking. The reference signal is picked up by another dipole antenna and is fed to the tail current source of the VCO as shown in Fig. 4.9. Feeding the signal to the tail current source sets the operating frequency of the VCO to half of the injection frequency (f_0). The locking range of the VCO depends on the input power level of the fed signal and the quality factor (Q) of the inductor. As the Q-factor increases, the locking range becomes smaller; and a higher input power level expands the locking range. The injection-locked VCOs have been shown as useful building blocks in imaging and spectroscopy applications [105]. However, a wide locking range is needed for a practical spectroscopy system which often demands a very strong reference signal present at the input of the

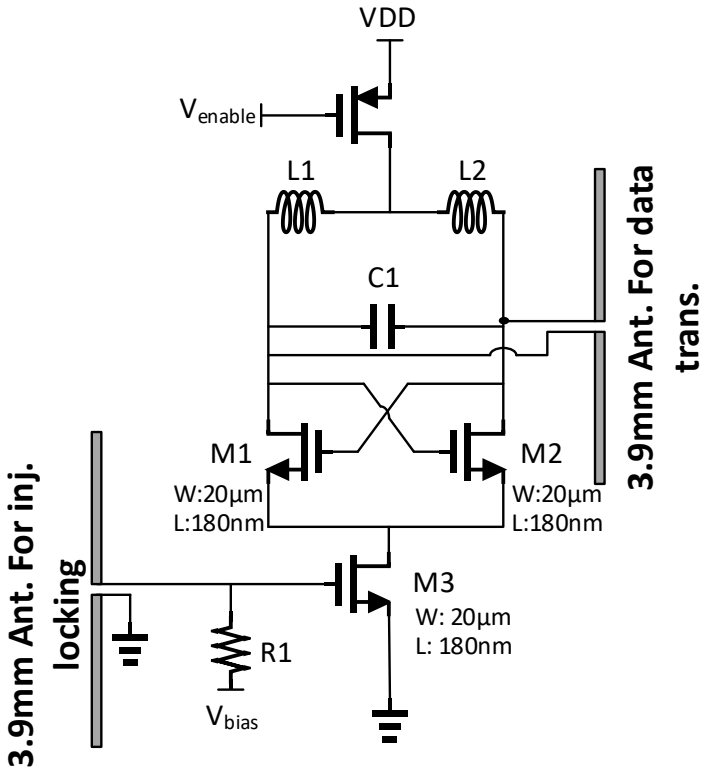

Figure 4.9. Circuit schematic of the injection-locked VCO.

VCO. For instance, to achieve a 1 GHz locking range with a center frequency of 4.5 GHz, a power level of 8 dBm should be present at the input of a VCO [105].

4.1.5 Experimental Results

The idea of coherent power combining in a distributed WSN system is evaluated using a 2 $\times$ 2 array of microchips that are arranged with a configuration shown in Fig. 3.15. The total area of each microchip, fabricated in 180-nm CMOS SOI process, is 3.9 $\times$ 0.7 mm^2 including three on-chip antennas that are used for power delivery, injection locking, and transmission of a reflected RF tone, respectively. An annotated micrograph is included at the bottom of Fig. 4.10 that shows different parts of the integrated systems. An E8257D Keysight signal generator is used as the source to generate an RF signal at the desired frequency. To extend

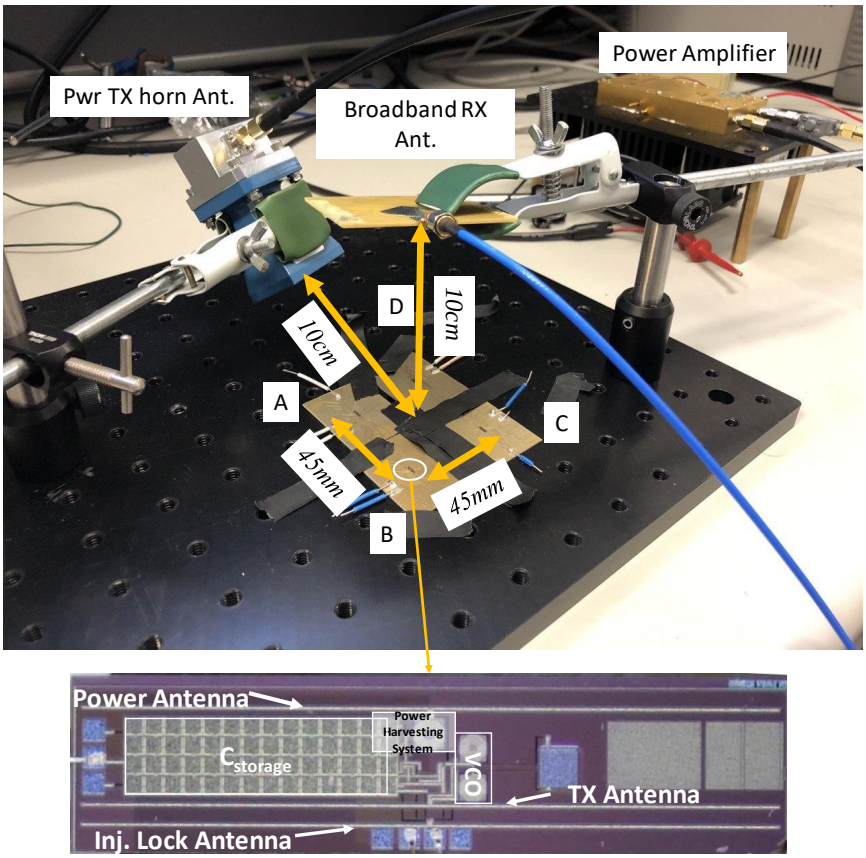

Figure 4.10. (top) Measurement setup for evaluating the performance of the proposed distributed sensor network. (bottom). The micrograph of a single microchip.

the operating range, the RF signal is passed through a power amplifier (RF-Lambda 0218G5) and is followed by a horn antenna with directivity of 10 dBi. The horn antenna radiates a focused beam that is used for power delivery and synchronizing the reflected RF tones from all the microchips. In this section, we describe the measured results for the wireless power harvesting system and demonstrate that the distributed sensor network successfully achieves a constructive power addition form all the four chips in the array.

4.1.5.1 Wireless Power Transmission Test

The performance of the wireless power harvesting system is evaluated for different values of transmitted power levels (P_{TX}) from the horn antenna. The measured voltage waveform at the VDD node of a single microchip without any external component is plotted in Fig. 4.11(a). The horn antenna is placed 10 cm away from the microchip and transmits a +30 dBm power carrier at 7.68 GHz. The received power by the on-chip dipole antenna for a 30 dBm Equivalent Isotropically Radiated Power (EIRP) source at a 5 cm distance is simulated and reported in [107]. Also, the matching efficiency between the dipole antenna and the voltage rectifier is simulated as 35 % at 8 GHz [107]. Therefore, the received power from the horn antenna with 10 dBi directivity at a 10 cm distance can be estimated as 700 μW. As evident from Fig. 4.11(a), the storage capacitor is charged and discharges with a frequency of 30 kHz and the discharging time lasts only for 10 μS. To extend the active time of the VCO, an external 1 μF shunt capacitor is placed in parallel with the $C_{storage}$. For a given current that is withdrawn (I_0) from the storage capacitor during the discharging phase, the discharging time can be expressed as:

$$t_{discharge} = (V_H - V_L) \times \frac{C_{strorage}}{I_0} \tag{4.6}$$

Repeating the same experiment with a 1 μF shunt capacitor indicates that the charging time and discharging time are scaled proportionally. The measured waveform is shown in Fig. 4.11(b).

4.1.5.2 Coherent Power Combining

In order to provide a proof-of-concept for the proposed sensor network, we have used four microchips that are locked to the frequency of the reference signal. As shown in Fig. 4.10, a custom-designed broadband antenna is placed at 10 cm distance from the center of the array to receive the radiated tones from the microchips. The broadband antenna is implemented

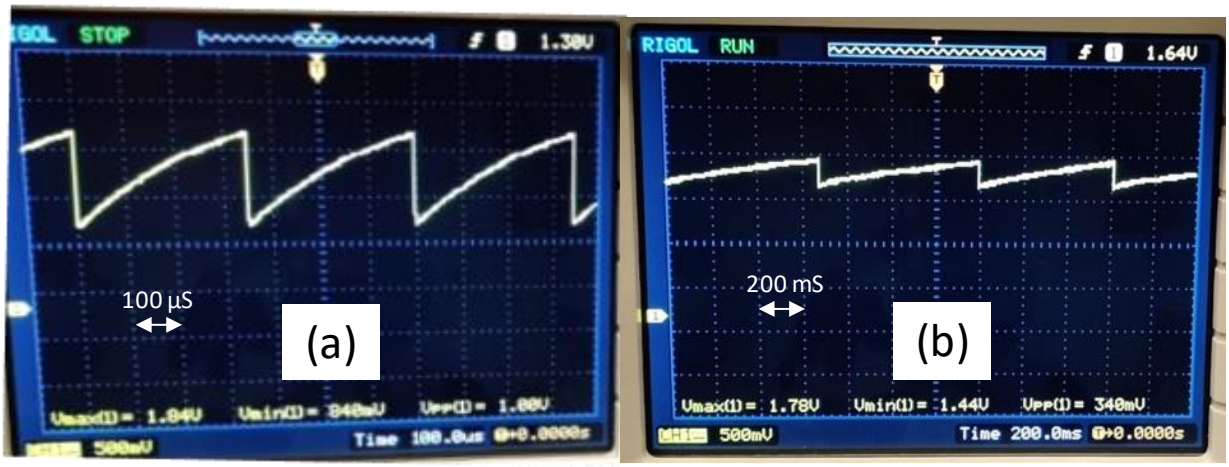

Figure 4.11. Measured waveform from the output node of the voltage rectifier: (a) $C_{storage}$ = 1.1 nF. (b) $C_{storage} = 1\mu$F.

as a Planar Inverted Cone Antenna (PICA) [110] and archives a bandwidth of 3-10 GHz. As shown in the previous section, the chips are capable of being wirelessly powered which results in a duty-cycled operation. When the chips are locked to the same power carrier signal, the reflected signals add up constructively. The constructive power combination of synchronized microchips is characterized in the frequency domain by investigating the frequency spectrum of the received signals. Duty-cycled operation imposes some challenges for detecting the spectrum of the reflected signals. The duty-cycling behavior can be considered as mixing the sinusoidal output of a VCO with a periodic pulse train. Hence, the spectrum of the received signal is a modulated version of the actual transmitted signal. To accurately measure the frequency and strength of the reflected signals, we used a dc power supply (a 1.3 V supply voltage connected to Vreg node of each microchip) to power up the microchips while they operate continuously.

To measure the free-running frequency of the VCOs and to verify synchronization through injection-locking, we have characterized the measurement setup in the frequency domain. Therefore, a Keysight spectrum analyzer (E4440A) is utilized to process the received signal

by the broadband antenna. To observe the effect of injection locking, we have compared the received spectrum in two different scenarios. First, all four microchips are powered and there is no reference signal transmitted from the horn antenna to synchronize the microchips. In this case, the VCOs are operating in free-running mode and it is expected the operating frequency of each VCO will be different for each microchip. The received spectrum is shown in Fig. 4.12 (a) where four different tones with different frequencies and different power levels can be spotted. It worth mentioning that at 4 GHz the delivered power from the VCO to the on-chip dipole antenna at a 1 V supply voltage is -25 dBm and the simulated radiation efficiency of the antenna is 4% [107]. Considering that a 700 μW power is required for activation, the reflection efficiency of one microchip is -38.4 dB. In the second case, a reference signal with a power level of +22 dBm is delivered to the horn antenna at 7.733 GHz. It should be noted that the required power for synchronizing the microchips is lower than the power needed for wireless power delivery. Hence, the minimum transmitted power from the horn antenna is set by power delivery considerations. As evident in Fig. 4.12(b), in the presence of a reference signal, all the VCOs are synchronized and the operating frequency is set to 3.866 GHz, which is half of the carrier frequency. In addition, the received signal strength is boosted to -35.33 dBm which verifies the idea of power amplification through a constructive summation of radiated signals from a distributed sensor network.

As mentioned earlier, the LC tank of the VCOs is deliberately designed with a moderate Q-factor to expand the locking range. To measure the clocking range of each microchip, we used the same measurement setup as shown in Fig. 3.15 and a 22 dBm reference signal is delivered to the horn antenna. The frequency of the reference signal is swept while only one microchip is connected to the supply. After repeating this experiment for all four microchips, the measured results reveal that the locking ranges overlap in 7.72-7.79 GHz frequency span. The received power from individual microchips across the locking range is plotted in Fig. 4.13 and labeled as "A", "B", "C", and "D". The locking range of the microchips can be could be expanded by increasing the transmitted power level or decreasing the distance

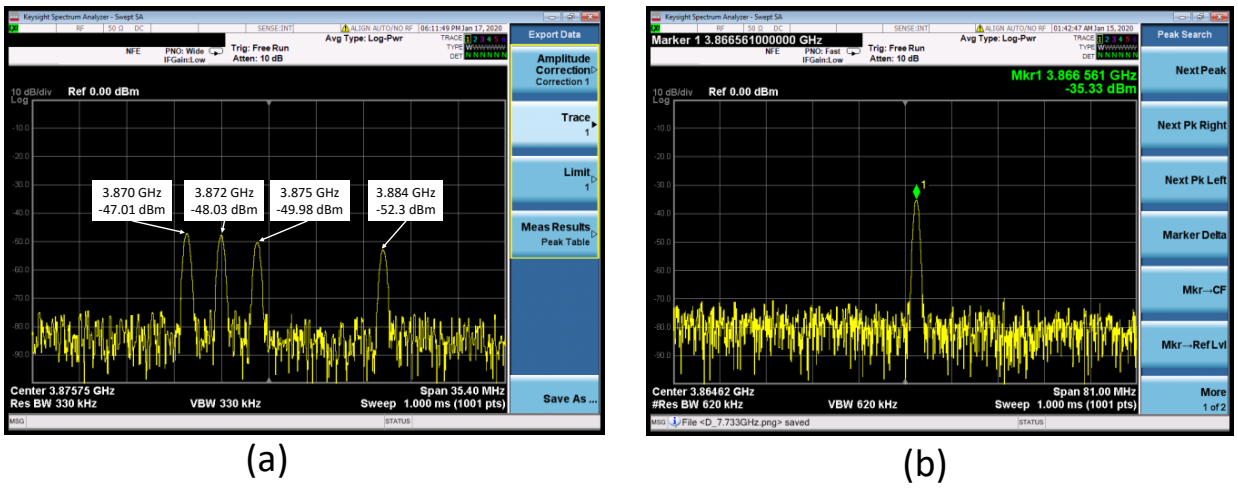

Figure 4.12. Measured spectrum of the radiated signal from four microchips: (a) In absence of the power carrier. (b) In presence of a 7.733 GHz power carrier.

between the horn antenna and the array. As mentioned in previous sections, achieving a 1 GHz locking range with a center frequency of 4.5 GHz requires a power level of 8 dBm at the input of the VCO. Knowing the received power from each microchip across the locking range, we have plotted the summation of all four power levels to compute the maximum achievable power labeled as "Ideal Addition" in Fig. 4.13. Next, we have activated all four chips and swept the reference frequency within the locking range. The received power, in this case, is plotted and labeled as "Coherent Addition". It is evident that the "Coherent Addition" is very close to the "Ideal Addition" and the small difference can be justified by the slight phase mismatch between the array element because of different path lengths to the horn antenna. Speculating the measured plots indicates that the resulted amplitude from coherent injection-locked microchips is satisfyingly close to the algebraic summation of all the amplitudes.

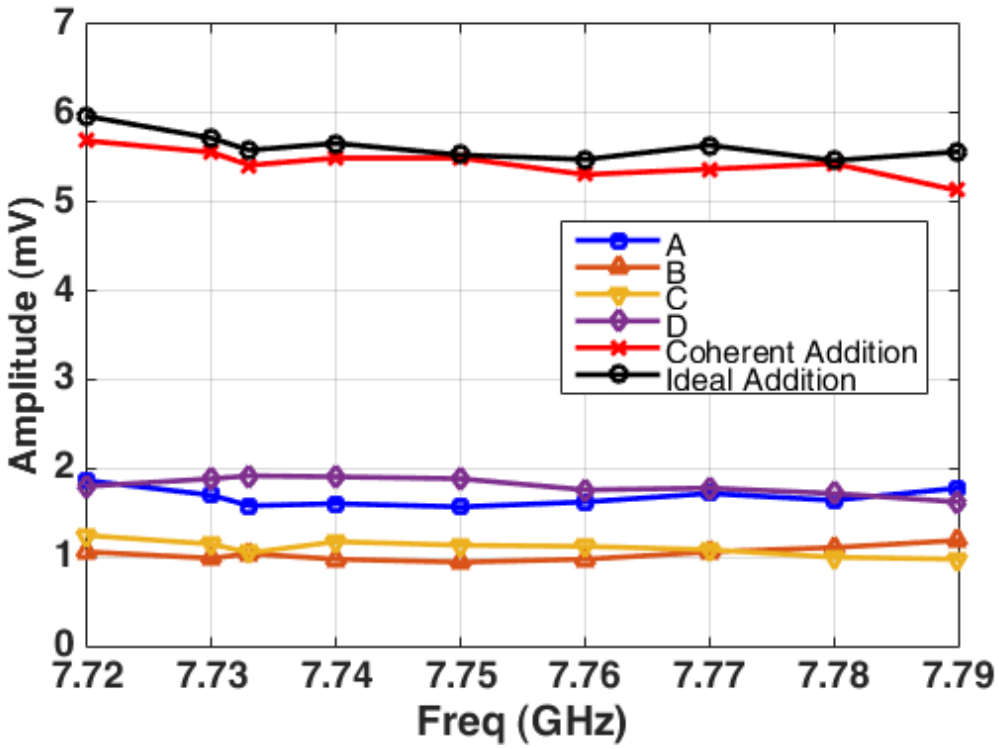

Figure 4.13. Receieved amplitude from the microchip array with different active elements versus frequency.

4.1.6 Conclusion

In this paper, we reported a distributed sensor network system based on mm-sized integrated microchips. Coherent power combining, enabled by injection-locked power oscillators, was introduced as an effective method to overcome the path loss and compensate the limited power level radiated from a single microchip. It was shown that the microchips can receive wireless power through a far-field RF link and the power carrier also serves as a reference signal to synchronize the distributed microchips. Considering the small form-factor of the microchips and their on-chip level integration, the proposed distributed sensing system is a promising solution for low-cost ubiquitous sensing and localization applications.

4.2 An Integrated Battery-Less Wirelessly Powered RFID Tag with Clock Recovery and Data Transmitter for UWB Localization

4.2.1 Introduction

Evolution of future Internet-of-Things applications mainly depends on the development of ubiquitous sensor networks. Radio Frequency Identification (RFID) has been unanimously accepted as a robust solution for enabling low-cost and ubiquitous sensing systems. RFID systems are utilized in various applications such as biomedical sensing, localization, inventory management, and monitoring physical parameters. Backscattering RFID tags have been widely adopted due to their near-zeros power consumption for data communication. However, backscattering systems rely on modulating the impedance of the same coil that is used for power delivery; hence the maximum data rate should be kept far below the link capacity to ensure power recovery is not disturbed by data communication [57, 111, 112]. Also, in backscattering tags, data communication and power delivery are conducted at the same frequency. Therefore, detection of the reflected signal at the reader becomes very challenging in the presence of a large TX signal for power delivery.

Emerging applications of RFID systems require battery-less operation and a small footprint. Therefore, the research trend in RFID tags is focused on low-cost and energy harvesting systems with small antennas that drives the need for a System-on-Chip (SoC) solution [63]. RFID tags with active communication have been reported recently [47, 70, 113]. Although active communication is not as energy efficient as a passive method, tags based on active communication can operate at a different frequency and can achieve higher data rates and communication ranges.

In this section that is based on our recent work [114], we present a fully on-chip wirelessly powered RFID tag with a total area of 2.4×2.3 mm^2 fabricated in 180 nm CMOS technology.

The proposed system includes an on-chip loop antenna for receiving power and clock signal through an inductive link. The design is composed of a rectenna, a power management unit (PMU), a clock recovery system, and a UWB transmitter. System architecture and design details of wireless link implementation are discussed in subsection 2. Performance of the proposed system is evaluated and reported in subsection 3.

4.2.2 Proposed Architecture

A block diagram of the proposed wirelessly powered RFID tag is demonstrated in Fig. 4.14 along with a conceptual diagram of a reader on the left side. The external loop antenna at the reader side is used to transmit RF power to the tag through an inductive link. The proposed tag is equipped with a rectenna, composed of an on-chip loop, matching capacitor, and a four-stage full-wave rectifier. Power carrier couples to the on-chip coil and induces a sinusoidal waveform across its terminal. The voltage rectifier converts RF signals to a dc voltage and accumulates energy into a storage capacitor (C_S). A Power Management Unit (PMU) monitors voltage level across CS and prevents it to go higher than the breakdown voltage [61]. The PMU consists of a low-dropout voltage regulator (LDO) to provide a constant dc voltage for the operation of clock recovery and the UWB transmitter. The LDO in this design provides two stable 1.1 V and 1.3 V voltages for the operation of digital blocks and the data transmitter, respectively while consuming 10 μA quiescent current. In addition, a Power-on-Reset circuitry is included in the PMU to ensure that digital circuity is reset upon activation and to avoid any unwanted state.

Digital circuitry in this design requires a clock signal to be triggered. Therefore, an ultra-low power data receiver (RX) is included to extract a square wave from incoming RF signals. To embed the clock signal into power link the carrier signal is modulated with Amplitude Shift Keying (ASK) scheme. The modulated power link can be formulated as in (4.7), where m stands for modulation index, f_{RF} is the frequency of power carrier, and $x(t)$ represents a square wave with a frequency much lower than f_{RF}.

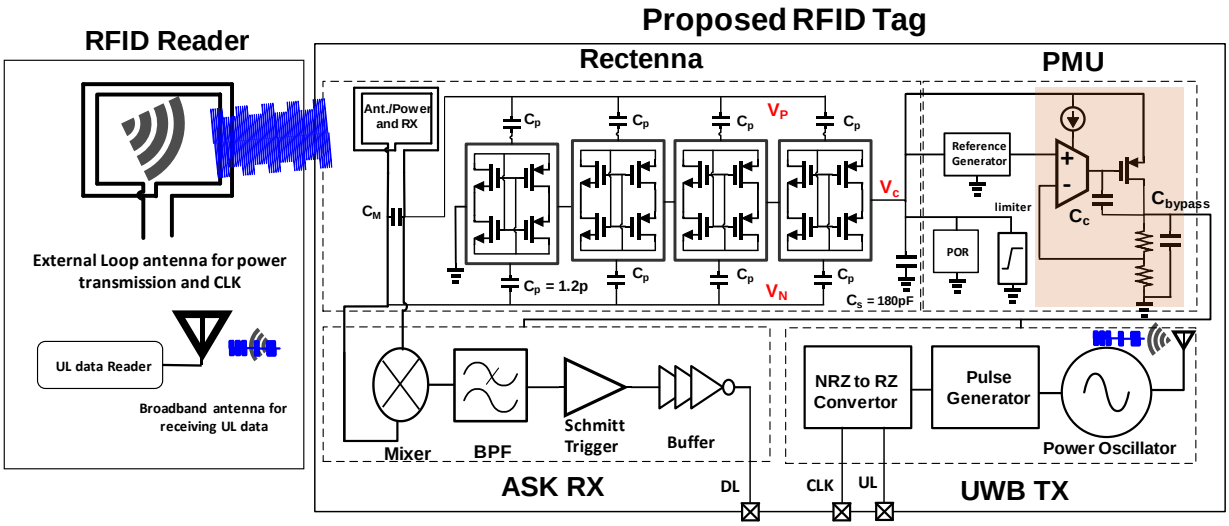

Figure 4.14. Block diagram of the proposed wirelessly powered RFID tag with on-chip antennas (right) along with a conceptual RFID reader (left).

$$V_P(t) - V_N(t) = Acos(2\pi f_{RF} t)[1 + mx(t)] \tag{4.7}$$

A detailed circuit schematic of the RX block is shown in Fig. 4.15. The RX utilizes a self-mixing architecture to extract the envelope of RF signals picked up by the on-chip coil. The output voltage of the mixer is connected to a shunt capacitance which extracts the envelope of the received signal. The envelope signal can be expresses as:

$$V_{env}(t) = \frac{2A}{\pi}[1 + mx(t)] \tag{4.8}$$

To remove the DC component from the envelope signal, $V_{env}(t)$ is passed through a Low-Pass Filter (LPF) and is compared with itself. As a result, the output of the comparator follows $x(t)$. To sharpen the recovered signal a Schmitt trigger is used after the comparator to generate a square wave with fast transition times. The RX is designed to recover square waves with frequencies up to 2 MHz with a power consumption of 1 μW.

Circuit schematic of the UWB transmitter (TX) and a conceptual timing diagram of the

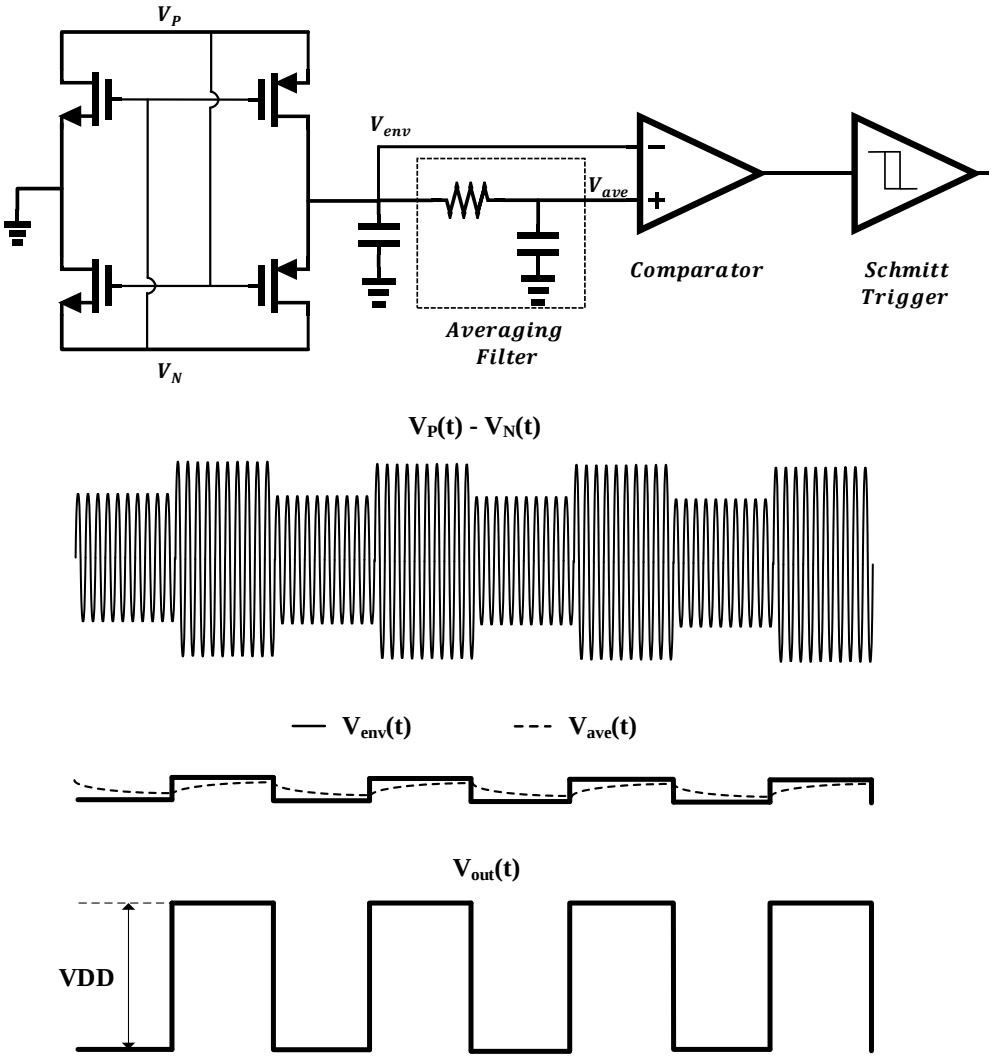

Figure 4.15. Circuit schematic of the data receiver and the timing diagram of the internal nodes.

internal nodes are shown in Fig. 4.16. The TX is based on a power-oscillator architecture which is shown to be very power efficient [1,115]. An on-chip dipole antenna is used directly at the load of the oscillator and radiates RF signals to the reader at the free-running frequency of the oscillator. The data rate of the TX block is determined by the CLK frequency. As shown in Fig. 4.16, the UL data stream is passed through an NRZ to RZ sub-system to enable the edge detection circuitry to generate consecutive short pulses when the UL remains

constant for consecutive periods. The generated pulses are used to connect the oscillator to the ground node and cause an oscillation, consequently. Simulation results show that the width of the generated pulse is about 50 ns for the typical technology corner. Hence, the average power consumption of the oscillator remains low and makes this approach compatible with a low-power RFID system.

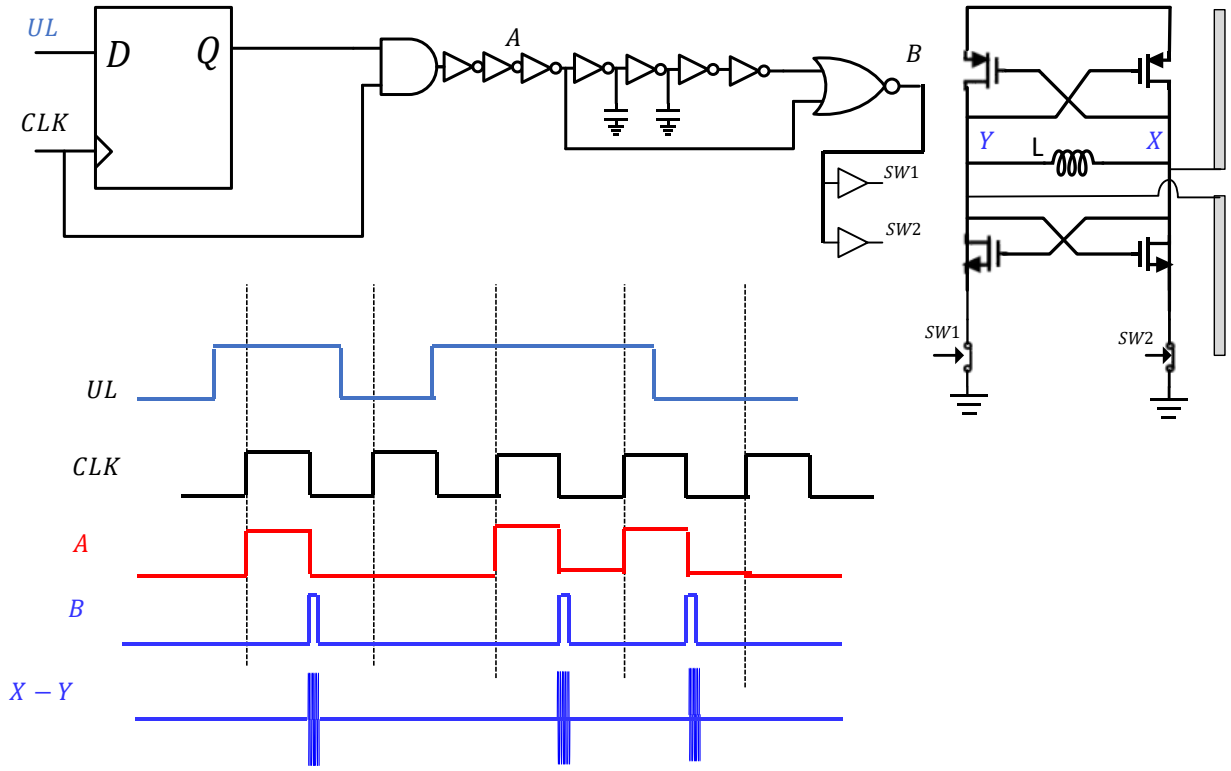

Figure 4.16. Circuit schematic of the UWB data transmitter and a conceptual timing diagram of the internal nodes.

The wireless link has been optimized by adopting an optimization algorithm as in [61]. Following the same procedure, the on-chip coil and the dipole antenna are designed with the geometry shown in Fig. 4.17 and dimensions are reported in Table 4.1.

Table 4.1 Values of dimension parameters of on-chip antennas.

Dimensions	**Transmitter**	**Receiver**
Width (W) (μm)	2250	2030
Length (L) (μm)	1010	2030
Trace Width (TW) (μm)	10	100
Trace Spacing (S) (μm)	100	50

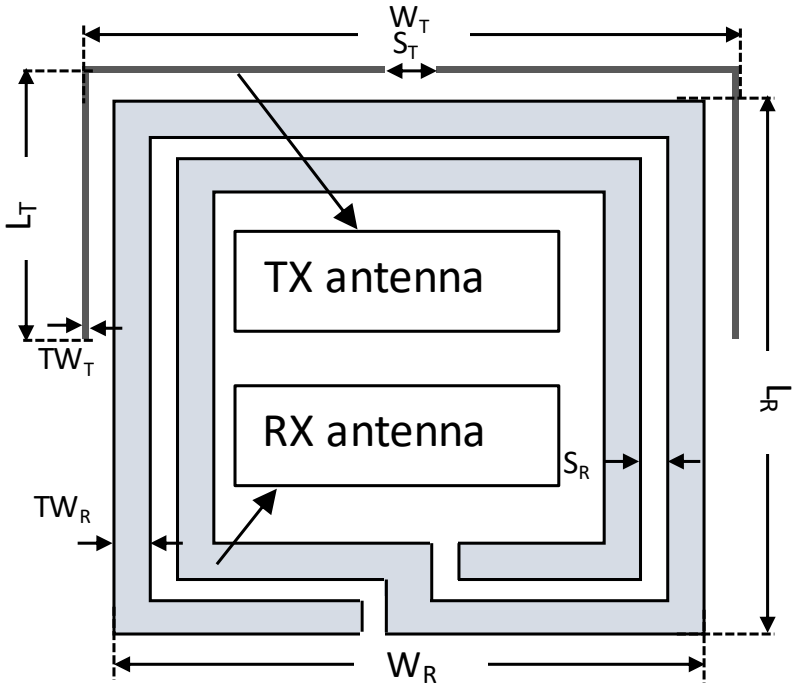

Figure 4.17. Detailed implementation of uplink and downlink wireless links.

4.2.3 Performance Evaluation

The proposed system is fabricated in TSMC 180 nm CMOS technology. The measurement setup for evaluating the performance is demonstrated in Fig. 4.18. The power carrier signal is fed to the LO node of a mixer and is modulated with a square wave connected to the IF

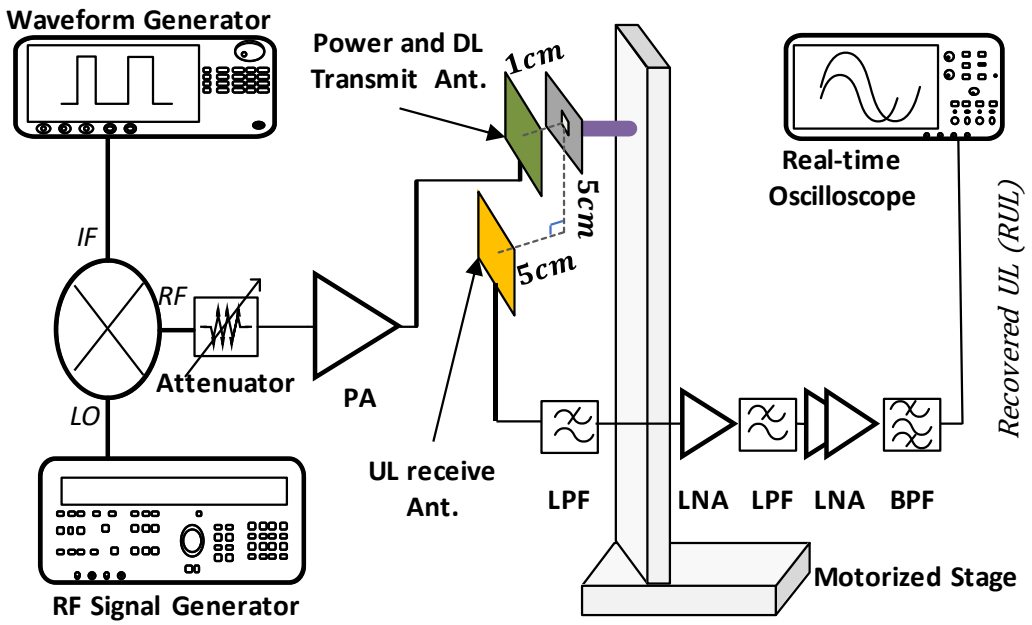

Figure 4.18. Measurement setup for performance evaluation of the proposed system.

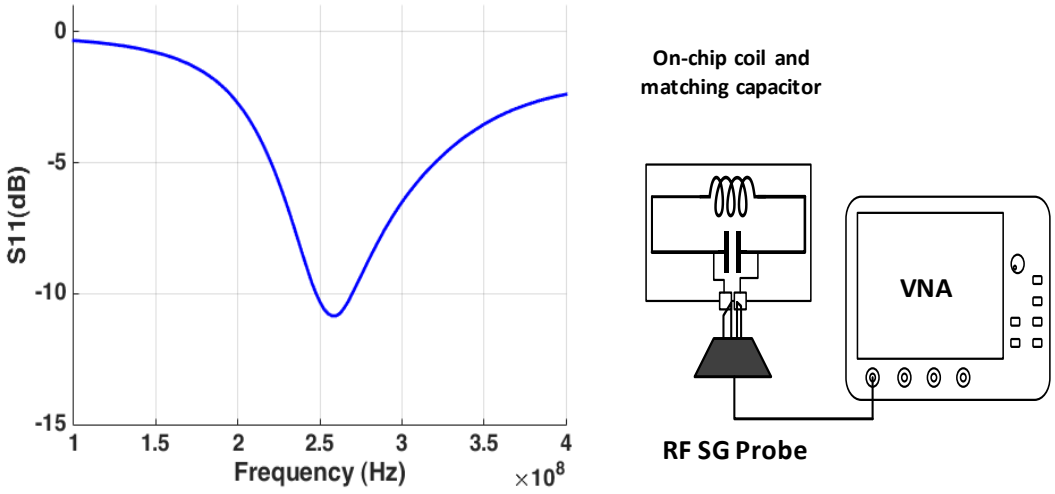

Figure 4.19. . (left) Measurement S_{11} of the on-chip coil. (right) Measurement setup for characterizing the on-chip coil.

terminal of the mixer. The modulation index is kept below 20% to ensure power delivery is not disturbed by the embedded clock signal into the power carrier. The modulated signal,

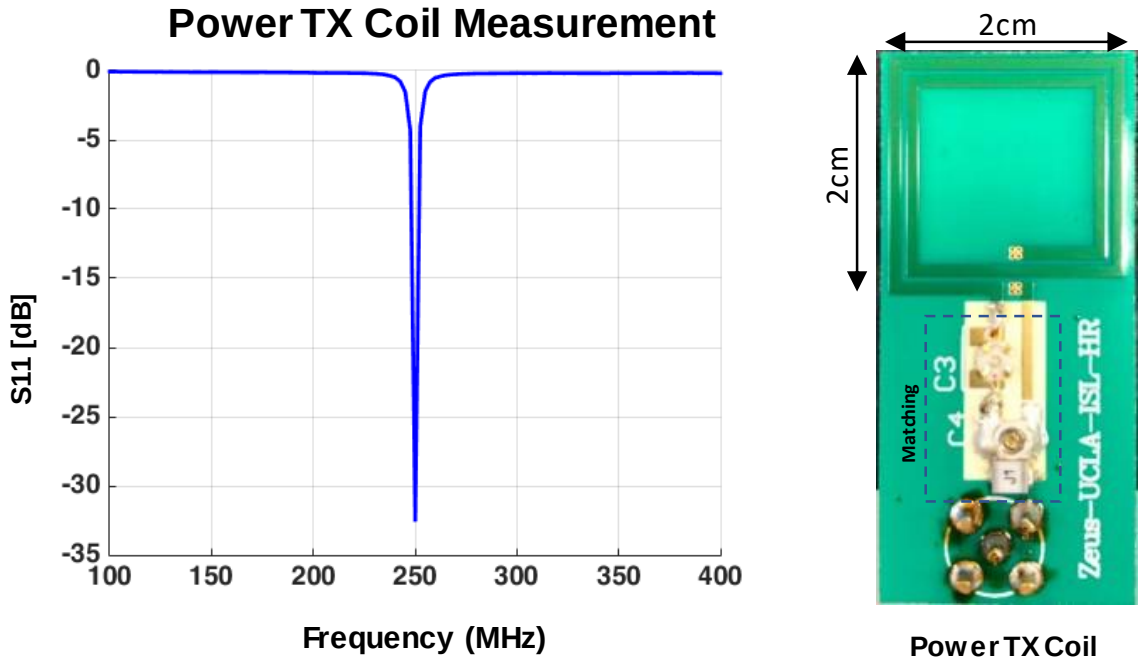

Figure 4.20. . (left) Measured S_{11} of the power TX antenna after matching. (right) Detailed implementation of the power TX loop [1].

which carries power and clock signal to the chip, is amplified and passed to the external loop antenna. The chip is located at a 1 cm distance from the power TX antenna. Another external broadband antenna is placed at a ∼7 cm distance from the chip to receive uplink (UL) data that is transmitted from the on-chip dipole antenna. The power carrier frequency is chosen based on the on-chip coil measurement. As shown in Fig. 4.19, measured S_{11} of the on-chip coil indicates a resonance happening at a frequency ∼250 MHz. Therefore, the power TX antenna is matched to the 50Ω impedance of the source. Detailed implantation of the power TX antenna and matching circuits are shown in Fig. 4.20 [1]. Simulated results indicate that the maximum efficiency of the wireless power transfer link can reach as high as -22.6 dB under perfect matching condition (rectifier loss is excluded).

The proposed system can be utilized as a transponder or as a data transmitter. In transponder mode, the recovered clock signal that is outputted from the RX (DL pad) is

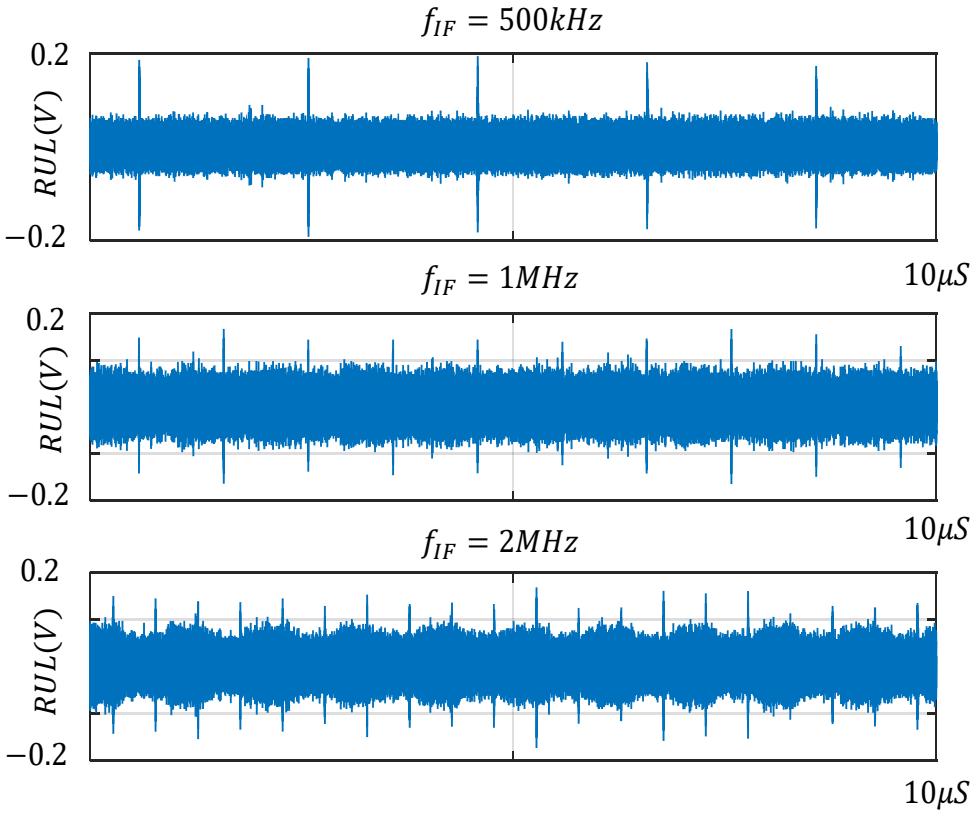

Figure 4.21. Recovered uplink data for various clock rates in transponder configuration.

connected to the CLK pad of the TX and UL pad, which is the data stream into the TX, is connected to the regulated voltage of the LDO. In this configuration, the chip transmits a train of short pulses when the system is powered up which resembles the performance of a transponder that can be used for localization applications. The Recovered uplink (RUL) data is demonstrated in Fig. 4.21 for various clock frequencies. As evident from this plot, the repetition rate of the RUL signal is uniquely controlled by the frequency of the square wave connected to the IF terminal of the mixer. It worth mentioning that for a higher clock frequency, modulation index should be increased to boost the transient response of the RX block. Also, the transmitted power level is increased for a higher clock rate. The maximum transmitted power from the antenna is kept below 28 dBm to avoid interference between the

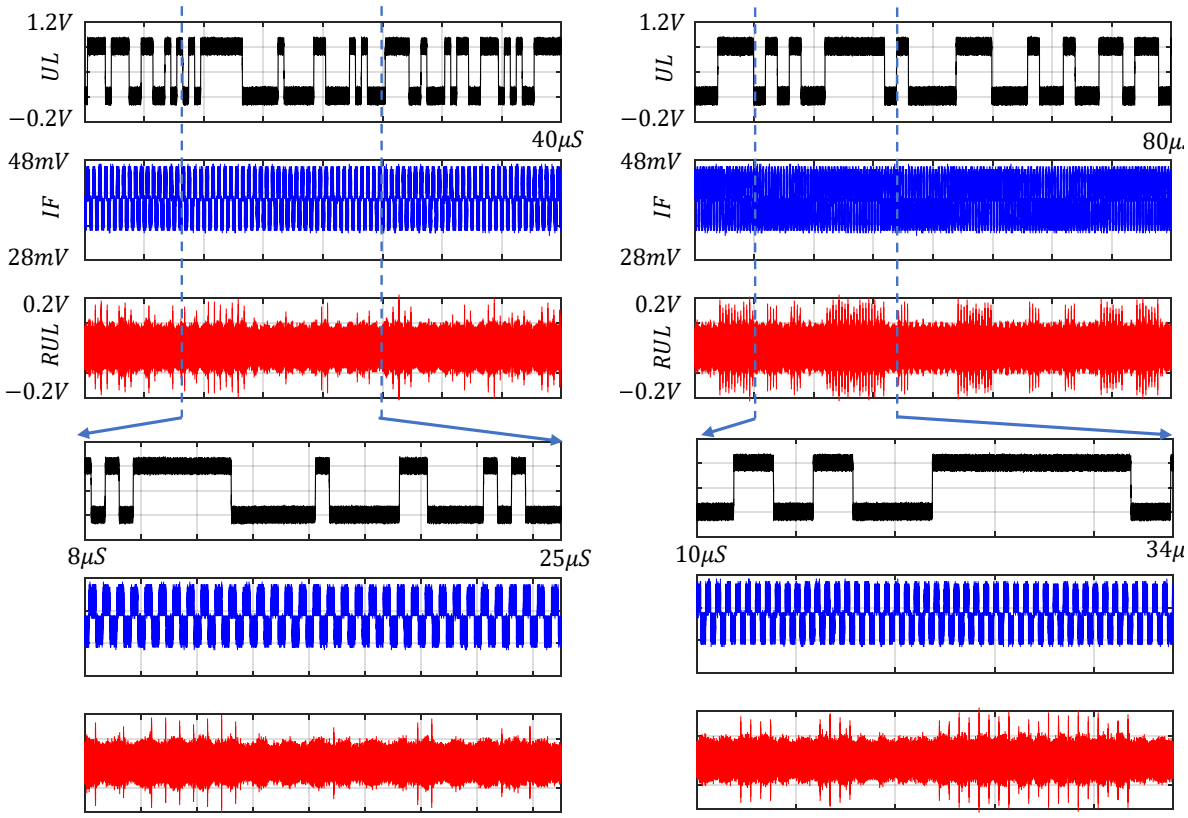

Figure 4.22. Measured RUL waveform in UWB transmitter configuration with f_{IF} = 2MHz, (left) bit rate of UL = 2Mbps, (right) bit rate of UL = 500kbps.

power link and data communication link due to injection pulling phenomena.

In data transmitter mode, the UL pad is connected to an arbitrary wave generator (Agilent 33522A) that feeds a sequence of Pseud-Random Binary Sequence (PSBR) to the chip. Fixing the clock frequency at 2 MHz, the RUL is recorded for two different bit rates of PSBR data and plotted in Fig. 4.22. Inspecting Fig. 4.22 shows that the number of recovered pulses in the RUL waveform is equal to the number of clock signal cycles that happen when the UL is '1'. It should be noted that the measured instantaneous power consumption of the oscillator is about 3.73 mW and based on the simulation results 21% of this power is delivered to the on-chip dipole antenna [1]. In UWB communication, the

pulse-width of each impulse is about 50 ns. Therefore, the average power consumption of the TX scales with the operating frequency. For instance, for a clock rate of 2 MHz, the average power consumption of the oscillator scales down to 37.3 μW.

4.2.4 Conclusion

In this work, we presented a 2.4 $\times$ 2.3 mm^2 wirelessly powered RFID tag that integrates two on-chip antennas for power delivery and data communication, respectively. The proposed system was powered at 250 MHz and the chip can extract a digital clock signal with frequencies up to 2 MHz. The measured results indicate that the proposed design can be used either as a transponder or an energy-efficient data transmitter. The presented system is compatible with the requirements of next-generation ubiquitous sensing systems and is a promising solution for UWB localization applications. The micrograph of this design is annotated and demonstrated in Fig. 4.23.

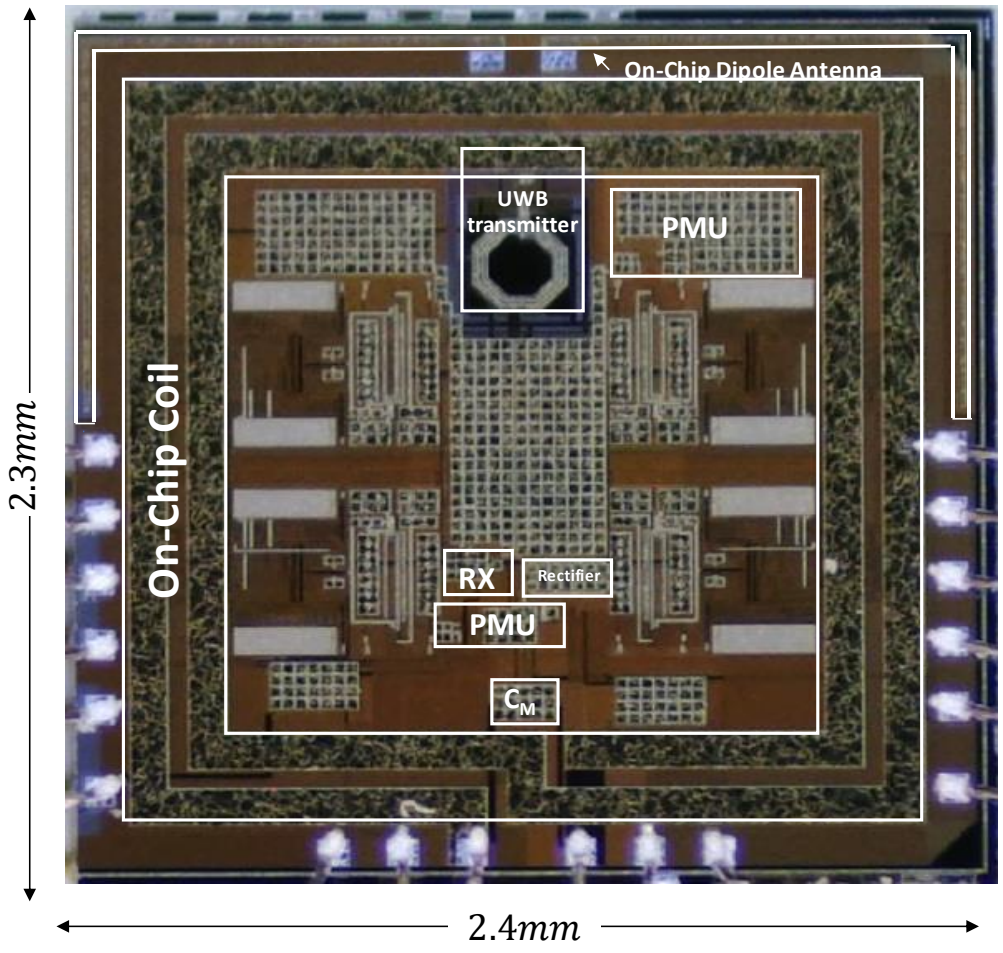

Figure 4.23. Annotate chip micrograph.

4.3 Conclusion

4.3.1 Closing Remarks

In this dissertation, I investigated RF wirelessly powered integrated circuits as a robust tool for enabling next-generation medical implants and IoT devices. The overall form-factor of the developed devices is limited to millimeter scale that results in many unprecedented opportunities in terms of cost, resolution, and scalability. Taking advantage of the integration capability of CMOS technology, silicon-based and fully on-chip designs were explored to tackle the challenges associated with power delivery, data communication, and low-power data front-ends. In addition, I investigated the opportunities offered by mm-sized form factor of the developed chips and proposed novel techniques to utilize the capabilities of numerous chips to overcome the limited operating range.

I investigated the main challenges for the development of a fully on-chip mm-sized power receiver system in CMOS technology. In chapter 2, I studied the wireless power transmission to mm-sized systems operating in the near-field electromagnetic region and presented an iterative optimization algorithm for maximizing the power transfer efficiency. I also adopted a comprehensive approach and jointly addressed the challenges of wireless power delivery that stem from safety regulations and non-linear behavior of voltage rectifier circuitry. Also, it was shown that there is an optimum frequency for power transmission, and the effect of intervening medium in the wireless link on the optimum frequency was investigated. Through extensive electromagnetic simulations, I showed that the maximum harvested power by mm-sized systems is limited to a few hundreds of micro-Watts and is susceptible to drop drastically in case of movement and misalignment of power transmitter and receiver. To address this issue, I presented a power management technique that makes enable the power harvesting system to operate reliably under various available power budgets. in addition, the power management technique enables the power harvesting system to drive power demanding blocks of a system with micro-Watt level incoming power under the duty-cycled scheme. in

chapter 2, I developed a 1.6×1.6 mm^2 power harvesting system that is capable of delivering up to 1.17 mW in the duty-cycled mode while the amount of transmitted power is 15 dBm.

In chapter 3, I focused on the data communication problem and proposed a fully integrated data transceiver that is compatible with the power budget and form-factor of the mm-sized wirelessly powered systems. Due to miniaturization, the available power budget is very small. Another main challenge of a mm-sized system is the low efficiency of an on-chip antenna that is used for data communication. To tackle these problems and design a data transceiver that is capable of supporting high-throughput communication, I proposed an RF powered dual-antenna transceiver that operates in a frequency division duplexing manner. Wireless power and downlink data are transferred to the chip through a 250 MHz RF link while the uplink data is transferred through a separate wireless link centered at 4.16 GHz. The designed radio supports up to 2.5 Mbps data rate in the downlink path and an instantaneous data rate of up to 150 Mbps in the uplink, respectively. Compared with prior-art TRXs that utilize any type of antenna for data communications, the proposed IC advances the energy efficiency for the RX by $\times 50$, and for the TX by $\times 2.3$. Considering the small form-factor and the ability for supporting high data rates, the proposed radio is an effective solution for the high-performance medical implant and IoT sensing systems.

Wireless integrated circuits and their capabilities in IoT is discussed in chapter 4. in particular, I explored localization as one of the prominent examples of next-generation IoTs and utilized mm-sized microchips in a distributed network. I presented a synchronization technique through injection-locked oscillators. In this technique, the power carrier serves for synchronizing the microchips that are placed in close proximity to each other. I demonstrated the theoretical framework for coherent power combining from a synchronized distributed sensor network and discussed how the received SNR from a cluster of microchips can improve the localization accuracy of the MUSIC algorithm. I also proposed a mm-sized IC for proximity-based localization. The proposed system acts as an active

RFID tag that is equipped with a UWB transmitter. Once the reader is in the operating range, the tag declares its presence by sending back short pulses as a transponder.

Advancement of CMOS technology and artificial intelligence have shown a promising path towards a connected and smart world. To open the gates toward and intelligent world, it is our responsibility, as researchers, to close the gap between the existing tools and demands of a connected world. It is predicted that by 2025, the number of IoT devices exceeds 25 billion. The astronomical growth of smart objects relies on the main pillars of IoT technology: Low-power connectivity, efficient processing algorithms, and ubiquitous sensing. In my view, adopting a comprehensive design approach that jointly captures the main pillars of future smart objects will open unprecedented opportunities and will take human life to an unimaginable era.

4.3.2 Future Direction

The topics covered in this dissertation provide techniques and solutions for a variety of problems toward next-generation SoCs. Challenges of wireless power delivery and data communication to mm-sized SoCs were extensively discussed for medical applications and IoT sensor nodes. There are still many research opportunities in the area of wirelessly powered SoCs and distributed sensor networks.

In near future and in the continuation of the research problems discussed in this thesis, I will collaborate with the Integrated Systems and Circuit (ISL) lab to develop intelligent and low-power sensing systems for medical applications and IoT nodes. My recent efforts on the development of such sensing systems are not included in this dissertation. However, it worth mentioning that we have explored machine-learning-assisted intelligent sensors for wound healing and preliminary results suggest that a proper classification algorithm for processing dielectric constants of various biological tissues can significantly relax the bandwidth, complexity, and power consumption of a dielectric sensing hardware [116]. Intelligent sensors are also explored by the ISL lab for spectroscopy purposes. [117].

To demonstrate an integrated mm-sized system that is capable of biological signal acquisition, I have continued the research efforts primarily presented in Chapter 3 and designed a wirelessly powered SoC for neural signal acquisition with clock recovery and a UWB data communication circuitry. The SoC is fabricated on a commercial CMOS technology and is composed of the following building blocks: 1- A power harvesting system that receives RF energy through an inductive wireless link. 2- A wireless clock receiver to provide an accurate clock signal for the digital blocks of the SoC with no external components such as a crystal oscillator. 3- A four-channel low-power and low-noise-amplifier sense neural activity and increase the voltage amplitude. 4- A four-channel Successive Approximation Register (SAR) Analog to Digital Converter (ADC) to convert the amplified signal by the LNAs to a 10-bit digital signal. 5- A Parallel-Input-Serial-Output (PISO) shift register unit that loads the digitized data from four recording channels and passed the serialized data stream to the data transmitter. 6- An Ultra-Wideband (UWB) data transmitter for wireless transmission of the recorded data to an external receiver. The designed system is not discussed in this dissertation and is currently going through the measurement process.

Intelligent and power-efficient sensing systems are one of the main pillars of future wireless technology. Hence, I believe utilizing artificial intelligence in conjunction with mm-sized SoCs will emerge as a promising solution in a broad range of applications and adopting a comprehensive research approach that jointly considered the hardware-associated challenges and evaluates system-level requirements is the key step toward this end.

In Chapter 2, I mainly focused on RF wireless power transmission systems for medical applications and IoT sensor nodes. However, I believe hybrid power delivery methods and energy harvesting options should be further explored to tackle the current challenges of wireless systems. Many practical issues such as misalignment of power TX/RX, the variation of wireless link composition, and Line-of-Sight blockage severely alters the link efficiency. As a result, wireless SoCs are prone to losing the continuous power flow in a practical

case. I believe research on sustainable power delivery and energy storage technologies will play an important role in next-generation wireless systems since the available power budget dominantly determines the functionality and the operating range.

Although this dissertation has addressed the challenges for data communication in mm-sized integrated systems, there is still more room to improve the overall energy efficiency and the operating range. With the emerging new technologies such as meta-materials, it is expected to enhance the efficiency of on-chip antennas that currently is one of the limiting factors both for communication and power delivery.

A very attractive, yet unexplored, research areas is the muti-nodal sensor networks built from mm-sized integrated systems. In Chapter 4, I discussed one of the examples of a multi-node networks for combating the low SNR problem in localization applications. However, there is still a significant gap between the proposed method and an actual localization system. Developing a larger array of network for further enhancement of SNR, implementation of an antenna array, and forming a synthetic radar aperture are the next steps toward a localization system. In addition, the efficacy of this idea should be evaluated with proper AoA algorithms.

APPENDIX A

Power Gains from S-Parameters for a Two-Port Network

The S-parameter matrix of a two-port network is a 2×2 matrix that can be written as in A.1,

$$S = \begin{bmatrix} s_{12} & s_{12} \\ s_{21} & s_{22} \end{bmatrix}. \tag{A.1}$$

Power reflection at different parts of the system can be calculated using the following coefficients written in equations A.2 – A.5.

$$\Gamma_{in} = \frac{Z_{in} - Z_0}{Z_{in} + Z_0} = s_{11} + \frac{s_{12}s_{21}\Gamma_L}{1 - s_{22}\Gamma_L} \tag{A.2}$$

$$\Gamma_{out} = \frac{Z_{out} - Z_0}{Z_{out} + Z_0} = s_{22} + \frac{s_{12}s_{21}\Gamma_G}{1 - s_{11}\Gamma_G} \tag{A.3}$$

$$\Gamma_G = \frac{Z_G - Z_0}{Z_G + Z_0} \tag{A.4}$$

$$\Gamma_L = \frac{Z_L - Z_0}{Z_L + Z_0} \tag{A.5}$$

Z_0 is the reference impedance, which is 50 Ω in this case. Γ_{in} and Γ_{out} are reflection coefficients at port 1 (input) and port 2 (output), respectively. Γ_{in} and Γ_G represent

reflection coefficients at the load and the source, respectively.

Similar to [33], we use the **S** matrix to calculate the system's power flow. The available power of the generator (P_{avG}) is the maximum power that can be delivered to the input port of the two-port network. In a case that network's input impedance (Z_{in}) is not conjugate matched to the impedance of the source (Z_G), a portion of P_{avG} reflects, and less power is delivered to the network (P_{in}).

An equivalent circuit model for the two-port network can be calculated by converting the **S** matrix to a **Z** matrix that includes impedance parameters of the two-port network. The **Z** matrix can be calculated using the transformation in equation A.6):

$$\mathbf{Z} = (\mathbf{I}_{2\times2} - \mathbf{S})^{-1}(\mathbf{I}_{2\times2} + \mathbf{S})^{-1} = \begin{bmatrix} Z_{11} & Z_{12} \\ Z_{21} & Z_{22} \end{bmatrix}]. \tag{A.6}$$

In Figure A.1, V_{Ind} is the induced voltage at the receiving side of the system due to the input power to the network. The values of V_{Ind}, Z_{in}, and Z_{out} are calculated in equations A.7 – A.9

$$V_{Ind} = \frac{Z_{21}V_G}{Z_{11} + Z_G} \tag{A.7}$$

$$Z_{in} = Z_{11} - \frac{Z_{12}Z_{21}}{Z_{22} + Z_L} \tag{A.8}$$

$$Z_{out} = Z_{22} - \frac{Z_{12}Z_{21}}{Z_{11} + Z_G} \tag{A.9}$$

P_{avG}, P_{in} , the maximum available power of the network at the output port (P_{avN}), and the delivered power to the load (P_L) are derived from the following equations which are calculated using the equivalent circuit model:

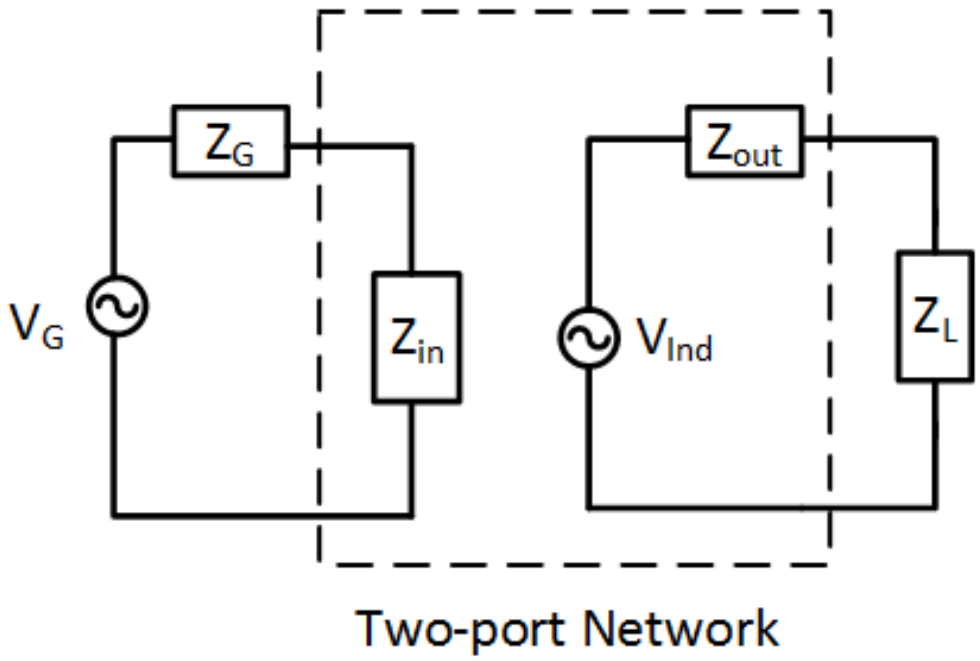

Figure A.1. An equivalent circuit model for a two-port network.

$$P_{avG} = \frac{|V_G|^2}{8Z_0}\frac{|1-\Gamma_G|^2}{1-|\Gamma_G|^2} \tag{A.10}$$

$$P_{in} = \frac{|V_G|^2}{8Z_0}\frac{(1-|\Gamma_{in}|^2)|1-\Gamma_G|^2}{|1-\Gamma_{in}\Gamma_G|} \tag{A.11}$$

$$P_{avN} = \frac{|V_G|^2}{8Z_0}\frac{|1-\Gamma_G|^2|s_{21}|^2}{(1-|\Gamma_{out}|^2)|1-s_{11}\Gamma_G|^2} \tag{A.12}$$

$$P_L = \frac{|V_G|^2}{8Z_0}\frac{|1-\Gamma_G|^2|s_{21}|^2(1-|\Gamma_L|^2)}{|(1-\Gamma_{in}\Gamma_G)(1-s_{22}\Gamma_L)|^2}. \tag{A.13}$$

If the source is conjugate matched to the input impedance of the two-port network ($\Gamma_{in} = \Gamma_G^*$), P_{in} becomes equal to P_{avG}. Similarly, having a matching circuit at the output results in $\Gamma_{out} = \Gamma_L^*$ and maximizes the delivered power to the load.

We can use equations A.10 – A.13, to define different metrics for measuring power transfer efficiency in a two-port network. Similar to [33], we define the fraction of delivered power to the load over available power of the source as transducer gain (G_T). Operating power gain (G_p) is another definition of power gain that is used frequently To calculate PTE in this chapter. As mentioned earlier in this thesis, PTE is calculated assuming the mismatch of the RX antenna and its load as an influential factor. It means that there is no matching circuit at the receiving side. In order to evaluate the effect of this mismatch on PTE, we introduce a new power gain: desired gain (G_{des}). G_{des} is the ratio of P_{avN} to P_{in}:

$$G_T = \frac{Delivered\,power\,to\,load}{Maximum\,available\,power\,of\,generator} = \frac{P_L}{P_{avG}} \tag{A.14}$$

$$G_p = \frac{Delivered\,power\,to\,load}{Input\,power\,to\,network} = \frac{P_L}{P_{in}} \tag{A.15}$$

$$G_{des} = \frac{Maximum\,avaibale\,power\,out\,of\,network}{Input\,power\,to\,network} = \frac{P_{avN}}{P_{in}} \tag{A.16}$$

The power gains in equations A.14 – A.16 can be expressed in terms of scattering parameters or impedance parameter. It is insightful to look to different power gains in a situation that Z_G and Z_L are matched to Z_0. In this case, $\Gamma_G = \Gamma_L = 0$ and $\Gamma_{in} = s_{11}$, $\Gamma_{out} = s_{22}$. Recalculating power gains results in the reduced formats written in equation A.17:

$$G_T = |s_{12}|^2,\ G_p = \frac{|s_{21}|^2}{(1-|s_{11}|^2)},\ G_{des} = \frac{|s_{21}|^2}{(1-|s_{11}|^2)(1-|s_{22}|^2)}. \tag{A.17}$$

Equation A.17 clearly shows the effect of mismatch on the PTE. In comparing the terms, it is evident that the portion of the generator's available power that is equal to $|s_{11}|^2 P_{avG}$ is reflected at the input port. Similarly, $|s_{22}|^2 P_{avN}$ is reflected at the output port of the network due to the mismatch. G_T is the most general term that includes the effect of impedance mismatches on both transmitting and receiving side. G_p only takes into account mismatches

on the receiving side, while G_{des} is completely independent from any impedance mismatch and is a function of s_{21}. s_{21} can be views as a coupling coefficient that dominantly determines PTE when there is no impedance mismatch in the system. **S** matrix of a passive network is symmetric, which means that s_{12} and s_{21} are equal. This assumption is valid for all passive networks. In a passive network, $|s_{12}| \leq 1$. The equality only happens for a loss-less network and means that 100% of input power to the network is transferred to its output port. s_{12} is an intrinsic feature of the network that depends on the network's physical properties such as dimension and types of materials. A wireless link that includes material with high losses, has smaller s_{21}.

In a two-port network, the power loss due to impedance mismatch at the output port is usually reported by defining "input return loss" as seen in equation A.18. "Insertion loss" and "output return loss" are two other terms used to formulate losses from the input port to the output and impedance mismatch at the output port (A.19, A.20).

$$IRL = 10log_{10}|\frac{1}{s_{11}^2}| = -20log_{10}|s_{11}|(dB) \tag{A.18}$$

$$IL = -20log_{10}|s_{12}|(dB) \tag{A.19}$$

$$ORL = 10log_{10}|\frac{1}{s_{22}^2}| = -20log_{10}|s_{22}|(dB) \tag{A.20}$$

The dependency of S parameters on the dimensions of the system implies that the impedance mismatch of TX and RX antennas is not the only factor that must be considered for designing an efficient power transfer method. Antenna structure and dimensions also could impact the S parameters and, consequently, change the performance of the system.

REFERENCES

[1] H. Rahmani and A. Babakhani, "A 1.6mm^3 wirelessly powered reconfigurable FDD radio with On-Chip antennas achieving 4.7 pJ/b TX and 1 pJ/b RX energy efficiencies for medical implants," in *Proc. IEEE Custom Integr. Circuits Conf. (CICC)*, 2020, pp. 1–4.

[2] A. P. Chandrakasan, N. Verma, and D. C. Daly, "Ultralow-power electronics for biomedical applications," *Annu. Rev. Biomed. Eng.*, vol. 10, pp. 247–274, 2008.

[3] B. Jamali and A. Babakhani, "A Fully Integrated 50280-GHz Frequency Comb Detector for Coherent Broadband Sensing," *IEEE Trans. Terahertz Sci. Technol.*, vol. 9, no. 6, pp. 613–623, 2019.

[4] S. Razavian, J. Han, B. Jamali, P. Pribyl, M. Hosseini, Y. Mehta, M. Forghani, W. Gekelman, and A. Babakhani, "Plasma Characterization using a Silicon-Based Terahertz Frequency Comb Radiator," *IEEE Sens. Lett.*, pp. 1–1, 2020.

[5] S. Razavian, M. M. Assefzadeh, M. Hosseini, and A. Babakhani, "Multi-Spectral THz Micro-Doppler Radar Based on a Silicon-Based Picosecond Pulse Radiator," in *Proc. IEEE MTT-S Int. Microw. Symp*, 2020.

[6] S. Razavian and A. Babakhani, "Thz micro-doppler measurements based on a silicon-based picosecond pulse radiator," in *Proc. IEEE MTT-S Int. Microw. Symp*, 2019, pp. 309–311.

[7] B. Jamali, S. Razavian, and A. Babakhani, "Fully electronic silicon-based THz pulse sources and detectors," in *Terahertz Photonics*, vol. 11348. International Society for Optics and Photonics, 2020, p. 113480E.

[8] N. Tandon, A. V. Alexopoulos, A. Warbel, I. M. Najm, and W. E. Bingaman, "Occipital epilepsy: spatial categorization and surgical management: clinical article," *J. Neurosurgery*, vol. 110, no. 2, pp. 306–318, 2009.

[9] H. Hamer *et al.*, "Complications of invasive video-eeg monitoring with subdural grid electrodes," *Neurology*, vol. 58, no. 1, pp. 97–103, 2002.

[10] B. Burle, L. Spieser, C. Roger, L. Casini, T. Hasbroucq, and F. Vidal, "Spatial and temporal resolutions of EEG: Is it really black and white? a scalp current density view," *Int. J. Psychophysiology*, vol. 97, no. 3, pp. 210–220, 2015.

[11] R. A. Normann, B. A. Greger, P. House, S. F. Romero, F. Pelayo, and E. Fernandez, "Toward the development of a cortically based visual neuroprosthesis," *J. Neural Eng.*, vol. 6, no. 3, p. 035001, 2009.

[12] D. Ahn and M. Ghovanloo, "Optimal design of wireless power transmission links for millimeter-sized biomedical implants," *IEEE Trans. Biomed. Circuits Syst.*, vol. 10, no. 1, pp. 125–137, Feb 2016.

[13] J.-U. Meyer, T. Stieglitz, O. Scholz, W. Haberer, and H. Beutel, "High density interconnects and flexible hybrid assemblies for active biomedical implants," *IEEE Trans. Advanced Package.*, vol. 24, no. 3, pp. 366–374, 2001.

[14] M. Kiani, U. M. Jow, and M. Ghovanloo, "Design and optimization of a 3-coil inductive link for efficient wireless power transmission," *IEEE Trans. Biomed. Circuits Syst.*, vol. 5, no. 6, pp. 579–591, Dec. 2011.

[15] A. Rajagopalan, A. K. RamRakhyani, D. Schurig, and G. Lazzi, "Improving power transfer efficiency of a short-range telemetry system using compact metamaterials," *IEEE Trans. Microw. Theory Techn.*, vol. 62, no. 4, pp. 947–955, Apr. 2014.

[16] U. M. Jow and M. Ghovanloo, "Design and optimization of printed spiral coils for efficient transcutaneous inductive power transmission," *IEEE Trans. Biomed. Circuits Syst.*, vol. 1, no. 3, pp. 193–202, Sep. 2007.

[17] A. S. Y. Poon, S. O'Driscoll, and T. H. Meng, "Optimal frequency for wireless power transmission into dispersive tissue," *IEEE Trans. Antennas Propag.*, vol. 58, no. 5, pp. 1739–1750, May 2010.

[18] A. Ibrahim and M. Kiani, "A figure-of-merit for design and optimization of inductive power transmission links for millimeter-sized biomedical implants," *IEEE Trans. Biomed. Circuits Syst.*, vol. 10, no. 6, pp. 1100–1111, Dec. 2016.

[19] M. Zargham and P. G. Gulak, "Fully integrated on-chip coil in 0.13 μm CMOS for wireless power transfer through biological media," *IEEE Trans. Biomed. Circuits Syst.*, vol. 9, no. 2, pp. 259–271, Apr. 2015.

[20] C. Kim, S. Ha, J. Park, A. Akinin, P. P. Mercier, and G. Cauwenberghs, "A 144-MHz fully integrated resonant regulating rectifier with hybrid pulse modulation for mm-sized implants," *IEEE J. Solid-State Circuits*, vol. 52, no. 11, pp. 3043–3055, Nov. 2017.

[21] H. Rahmani and A. Babakhani, "A fully integrated electromagnetic energy harvesting circuit with an on-chip antenna for biomedical implants in 180 nm SOI CMOS," in *Proc. IEEE Sensors*, Oct. 2016, pp. 1–3.

[22] S. O'Driscoll, A. S. Y. Poon, and T. H. Meng, "A mm-sized implantable power receiver with adaptive link compensation," in *IEEE Int. Solid-State Circuits Conf. (ISSCC) Dig. Tech. Papers*, Feb. 2009, pp. 294–295,295a.

[23] R. Muller *et al.*, "A minimally invasive 64-channel wireless μECoG implant," *IEEE J. Solid-State Circuits*, vol. 50, no. 1, pp. 344–359, Jan. 2015.

[24] A. Y. S. Jou, H. Pajouhi, R. Azadegan, and S. Mohammadi, "A CMOS integrated rectenna for implantable applications," in *IEEE MTT-S Int. Microw. Symp. Dig.*, May 2016, pp. 1–3.

[25] A. Yakovlev, J. H. Jang, and D. Pivonka, "An 11 μW sub-pj/bit reconfigurable transceiver for mm-sized wireless implants," *IEEE Trans. Biomed. Circuits Syst.*, vol. 10, no. 1, pp. 175–185, Feb. 2016.

[26] M. Zargham and P. G. Gulak, "A 0.13 μm CMOS integrated wireless power receiver for biomedical applications," in *Proc. IEEE Eur. Solid-State Circuits Conf. (ESSCIRC)*. IEEE, Sep. 2013, pp. 137–140.

[27] H. Rahmani, "Integrated electromagnetic wireless power harvesting system for mm-size biomedical implants," Master's thesis, Rice University, 2017.

[28] M. Mark, "Powering mm-size wireless implants for brain-machine interfaces," Ph.D. dissertation, UC Berkeley, 2011.

[29] A. Drossos, V. Santomaa, and N. Kuster, "The dependence of electromagnetic energy absorption upon human head tissue composition in the frequency range of 300-3000 MHz," *IEEE Trans. Microw. Theory Techn.*, vol. 48, no. 11, pp. 1988–1995, Nov. 2000.

[30] K. Na, H. Jang, H. Ma, and F. Bien, "Tracking optimal efficiency of magnetic resonance wireless power transfer system for biomedical capsule endoscopy," *IEEE Trans. Microw. Theory Techn.*, vol. 63, no. 1, pp. 295–304, Jan. 2015.

[31] M. Q. Nguyen, Z. Hughes, P. Woods, Y. S. Seo, S. Rao, and J. C. Chiao, "Field distribution models of spiral coil for misalignment analysis in wireless power transfer systems," *IEEE Trans. Microw. Theory Techn.*, vol. 62, no. 4, pp. 920–930, Apr. 2014.

[32] H. Rahmani and A. Babakhani, "A wireless power receiver with an on-chip antenna for millimeter-size biomedical implants in 180 nm SOI CMOS," in *IEEE MTT-S Int. Microw. Symp.*, Jun. 2017, pp. 300–303.

[33] S. J. Orfanidis, *Electromagnetic waves and antennas*. Rutgers University New Brunswick, NJ, 2002.

[34] C. Gabriel, S. Gabriel, and E. Corthout, "The dielectric properties of biological tissues: I. literature survey," *Physics in medicine and biology*, vol. 41, no. 11, p. 2231, 1996.

[35] M. Zargham and P. G. Gulak, "Maximum achievable efficiency in near-field coupled power-transfer systems," *IEEE Trans. Biomed. Circuits Syst.*, vol. 6, no. 3, pp. 228–245, Jun. 2012.

[36] U. M. Jow and M. Ghovanloo, "Modeling and optimization of printed spiral coils in air, saline, and muscle tissue environments," *IEEE Trans. Biomed. Circuits Syst.*, vol. 3, no. 5, pp. 339–347, Oct. 2009.

[37] A. K. RamRakhyani, S. Mirabbasi, and M. Chiao, "Design and optimization of resonance-based efficient wireless power delivery systems for biomedical implants," *IEEE Trans. Biomed. Circuits Syst.*, vol. 5, no. 1, pp. 48–63, Feb. 2011.

[38] K. Agarwal, R. Jegadeesan, Y.-X. Guo, and N. V. Thakor, "Wireless power transfer strategies for implantable bioelectronics," *IEEE Rev. Biomed. Eng.*, vol. 10, pp. 136–161, 2017.

[39] N.-C. Kuo, B. Zhao, and A. M. Niknejad, "Equation-based optimization for inductive power transfer to a miniature CMOS rectenna," *IEEE Trans. Microw. Theory Techn.*, vol. 66, no. 5, pp. 2393–2408, 2018.

[40] S. Mandal and R. Sarpeshkar, "Low-power CMOS rectifier design for RFID applications," *IEEE Trans. Circuits Syst. I, Reg. Papers*, vol. 54, no. 6, pp. 1177–1188, Jun. 2007.

[41] "Mentor Graphics. HyperLynx 3D EM, IE3D. [Online]. Available: http://www.mentor.com/pcb/hyperlynx/3d-em/."

[42] A. M. Silva *et al.*, "Ethnicity-related skeletal muscle differences across the lifespan," *American Journal of Human Biology*, vol. 22, no. 1, pp. 76–82, 2010.

[43] B. W. Flynn and K. Fotopoulou, "Rectifying loose coils: Wireless power transfer in loosely coupled inductive links with lateral and angular misalignment," *IEEE Microw. Mag.*, vol. 14, no. 2, pp. 48–54, Mar. 2013.

[44] M. Q. Nguyen, Z. Hughes, P. Woods, Y. S. Seo, S. Rao, and J. C. Chiao, "Field distribution models of spiral coil for misalignment analysis in wireless power transfer systems," *IEEE Trans. Microw. Theory Techn.*, vol. 62, no. 4, pp. 920–930, Apr. 2014.

[45] K. N. Bocan and E. Sejdić, "Adaptive transcutaneous power transfer to implantable devices: A state of the art review," *Sensors*, vol. 16, no. 3, p. 393, 2016.

[46] "CST microwave studio getting started, CST-comput. simulation technol." *Darmstadt, Germany*, 2016.

[47] G. Papotto, F. Carrara, A. Finocchiaro, and G. Palmisano, "A 90-nm CMOS 5-Mbps crystal-less RF-powered transceiver for wireless sensor network nodes," *IEEE J. Solid-State Circuits*, vol. 49, no. 2, pp. 335–346, Feb. 2014.

[48] M. Stoopman, S. Keyrouz, H. J. Visser, K. Philips, and W. A. Serdijn, "Co-design of a CMOS rectifier and small loop antenna for highly sensitive RF energy harvesters," *IEEE J. Solid-State Circuits*, vol. 49, no. 3, pp. 622–634, Mar. 2014.

[49] S. Hemour *et al.*, "Towards low-power high-efficiency RF and microwave energy harvesting," *IEEE Trans. Microw. Theory Techn.*, vol. 62, no. 4, pp. 965–976, Apr. 2014.

[50] E. Falkenstein, M. Roberg, and Z. Popovic, "Low-power wireless power delivery," *IEEE Trans. Microw. Theory Techn.*, vol. 60, no. 7, pp. 2277–2286, Jul. 2012.

[51] C. Lu *et al.*, "17.4 a sub-mw antenna-impedance detection using electrical balance for single-step on-chip tunable matching in wearable/implantable applications," in *IEEE Int. Solid-State Circuits Conf. (ISSCC) Dig. Tech. Papers*, Feb. 2017, pp. 298–299.

[52] M. Song *et al.*, "An energy-efficient antenna impedance detection using electrical balance for single-step on-chip tunable matching in wearable/implantable applications," *IEEE Trans. Biomed. Circuits Syst.*, vol. 11, no. 6, pp. 1236–1244, Dec. 2017.

[53] A. Tavakol and R. B. Staszewski, "An impedance sensor for MEMS adaptive antenna matching," in *IEEE Radio Freq. Integr. Circuits (RFIC) Symp. Dig. Papers*, May 2015, pp. 379–382.

[54] M. Baghaei-Nejad, D. S. Mendoza, Z. Zou, S. Radiom, G. Gielen, L.-R. Zheng, and H. Tenhunen, "A remote-powered RFID tag with 10Mb/s UWB uplink and $-18.5dbm$ sensitivity uhf downlink in 0.18 μm CMOS," in *IEEE Int. Solid-State Circuits Conf. (ISSCC) Dig. Tech. Papers*, Feb. 2009, pp. 198–199,199a.

[55] M. Seok, G. Kim, D. Blaauw, and D. Sylvester, "A portable 2-transistor picowatt temperature-compensated voltage reference operating at 0.5 v," *IEEE J. Solid-State Circuits*, vol. 47, no. 10, pp. 2534–2545, Oct. 2012.

[56] V. Karkare, S. Gibson, and D. Markovi, "A 75-μW, 16-channel neural spike-sorting processor with unsupervised clustering," *IEEE J. Solid-State Circuits*, vol. 48, no. 9, pp. 2230–2238, 2013.

[57] C. Jeon, J. Koo, K. Lee, M. Lee, S. Kim, S. Shin, S. K. Hahn, and J. Sim, "A smart contact lens controller IC supporting dual-mode telemetry with wireless-powered backscattering LSK and EM-radiated RF transmission using a single-loop antenna," *IEEE J. Solid-State Circuits*, vol. 55, no. 4, pp. 856–867, 2020.

[58] X. Qian, Y. Wu, T. Yang, C. Cheng, H. Chu, W. Cheng, T. Yen, T. Lin, Y. Lin, Y. Lee, J. Chang, S. Lin, S. Li, T. Wu, C. Huang, C. Lee, C. Yang, C. Hung, T. Chi, C. Liu, M. Ker, and C. Wu, "A bone-guided cochlear implant cmos microsystem preserving acoustic hearing," in *Proc. Symp. VLSI Circuits*, 2017, pp. C46–C47.

[59] H. Ando, K. Takizawa, T. Yoshida, K. Matsushita, M. Hirata, and T. Suzuki, "Wireless multichannel neural recording with a 128-Mbps UWB transmitter for an implantable

brain-machine interfaces," *IEEE Trans. Biomed. Circuits Syst.*, vol. 10, no. 6, pp. 1068–1078, 2016.

[60] M. Manteghi, "Fundamental limits, bandwidth, and information rate of electrically small antennas: Increasing the throughput of an antenna without violating the thermodynamic Q-factor," *IEEE Antennas Propag. Mag.*, vol. 61, no. 3, pp. 14–26, 2019.

[61] H. Rahmani and A. Babakhani, "A dual-mode RF power harvesting system with an on-chip coil in 180-nm SOI CMOS for Millimeter-Sized biomedical implants," *IEEE Trans. Microw. Theory Techn.*, vol. 67, no. 1, pp. 414–428, 2019.

[62] C. Kim, S. Ha, A. Akinin, J. Park, R. Kubendran, H. Wang, P. P. Mercier, and G. Cauwenberghs, "Design of miniaturized wireless power receivers for mm-sized implants," in *Proc. IEEE Custom Integr. Circuits Conf. (CICC)*, 2017, pp. 1–8.

[63] H. Rahmani and A. Babakhani, "A 434 MHz Dual-Mode Power Harvesting System with an On-chip Coil in 180 nm CMOS SOI for mm-Sized Implants," in *IEEE MTT-S Int. Microw. Symp. Dig.*, 2018, pp. 1130–1133.

[64] C. Jeon, J. Koo, K. Lee, S. Kim, S. K. Hahn, B. Kim, H. Park, and J. Sim, "A 143nw glucose-monitoring smart contact lens IC with a dual-mode transmitter for wireless-powered backscattering and RF-radiated transmission using a single loop antenna," in *Proc. Symp. VLSI Circuits*, 2019, pp. C294–C295.

[65] J. Thimot, K. Kim, C. Shi, and K. L. Shepard, "A 27-Mbps, 0.08-mm3 CMOS transceiver with simultaneous near-field power transmission and data telemetry for implantable systems," in *Proc. IEEE Custom Integr. Circuits Conf. (CICC)*, 2020, pp. 1–4.

[66] S. Ha, C. Kim, J. Park, S. Joshi, and G. Cauwenberghs, "Energy recycling telemetry IC with simultaneous 11.5 mW power and 6.78 Mb/s backward data delivery over a single 13.56 MHz inductive link," *IEEE J. Solid-State Circuits*, vol. 51, no. 11, pp. 2664–2678, 2016.

[67] Y. Shi, M. Choi, Z. Li, Z. Luo, G. Kim, Z. Foo, H. Kim, D. D. Wentzloff, and D. Blaauw, "A 10 mm3 inductive coupling radio for syringe-implantable smart sensor nodes," *IEEE J. Solid-State Circuits*, vol. 51, no. 11, pp. 2570–2583, 2016.

[68] S. A. Mirbozorgi, H. Bahrami, M. Sawan, L. A. Rusch, and B. Gosselin, "A single-chip full-duplex high speed transceiver for multi-site stimulating and recording neural implants," *IEEE Tran. Biomed. Circuits Syst.*, vol. 10, no. 3, pp. 643–653, 2016.

[69] T. C. Chang, M. L. Wang, J. Charthad, M. J. Weber, and A. Arbabian, "27.7 a 30.5mm3 fully packaged implantable device with duplex ultrasonic data and power

links achieving 95kb/s with ¡104 BER at 8.5cm depth," in *Int. Solid-State Circuits Conf. (ISSCC) Dig. Tech. Papers*, 2017, pp. 460–461.

[70] Y. Rajavi, M. Taghivand, K. Aggarwal, A. Ma, and A. S. Y. Poon, "An RF-powered FDD radio for neural microimplants," *IEEE J. Solid-State Circuits*, vol. 52, no. 5, pp. 1221–1229, 2017.

[71] F. Goodarzy, E. Skafidas, and S. Gambini, "Feasibility of energy-autonomous wireless microsensors for biomedical applications: Powering and communication," *IEEE Rev. Biomed. Eng.*, vol. 8, pp. 17–29, 2015.

[72] J. Tan, W. Liew, C. Heng, and Y. Lian, "A 2.4 GHz ULP reconfigurable asymmetric transceiver for single-chip wireless neural recording IC," *IEEE Trans. Biomed. Circuits Syst.*, vol. 8, no. 4, pp. 497–509, 2014.

[73] A. Roy, A. Klinefelter, F. B. Yahya, X. Chen, L. P. Gonzalez-Guerrero, C. J. Lukas, D. A. Kamakshi, J. Boley, K. Craig, M. Faisal, S. Oh, N. E. Roberts, Y. Shakhsheer, A. Shrivastava, D. P. Vasudevan, D. D. Wentzloff, and B. H. Calhoun, "A 6.45 μW self-powered SoC with integrated energy-harvesting power management and ULP asymmetric radios for portable biomedical systems," *IEEE Trans. Biomed. Circuits Syst.*, vol. 9, no. 6, pp. 862–874, 2015.

[74] J. Charthad, M. J. Weber, T. C. Chang, and A. Arbabian, "A mm-sized implantable medical device (IMD) with ultrasonic power transfer and a hybrid bi-directional data link," *IEEE J. Solid-State Circuits*, vol. 50, no. 8, pp. 1741–1753, 2015.

[75] X. Liu, M. M. Izad, L. Yao, and C. Heng, "A 13 pJ/bit 900 MHz QPSK/16-QAM band shaped transmitter based on injection locking and digital PA for biomedical applications," *IEEE J. Solid-State Circuits*, vol. 49, no. 11, pp. 2408–2421, 2014.

[76] M. Elhebeary and C. K. Yang, "A Class-D FVF LDO With Multi-Level PWM Gate Control, 280-ns Settling Time, and No Overshoot/Undershoot," *IEEE Trans. Circuits Syst. I, Reg. Papers*, pp. 1–11, 2020.

[77] M. Elhebeary and C. K. Yang, "A 92%-Efficiency Battery Powered Hybrid DC-DC Converter for IoT Applications," *IEEE Trans. Circuits Syst. I, Reg. Papers*, pp. 1–10, 2020.

[78] L. Fanori and P. Andreani, "Class-d CMOS oscillators," *IEEE J. Solid-State Circuits*, vol. 48, no. 12, pp. 3105–3119, 2013.

[79] M. Babaie, M. Shahmohammadi, and R. Staszewski, *RF CMOS Oscillators for Modern Wireless Applications*. River Publishers, 2019. [Online]. Available: https://books.google.com/books?id=Vi15xQEACAAJ

[80] D. Barras, F. Ellinger, H. Jackel, and W. Hirt, "Low-power ultra-wideband wavelets generator with fast start-up circuit," *IEEE Trans. Microw. Theory Techn.*, vol. 54, no. 5, pp. 2138–2145, 2006.

[81] A. M. El-Gabaly and C. E. Saavedra, "A quadrature pulse generator for short-range UWB vehicular radar applications using a pulsed oscillator and a variable attenuator," *IEEE Trans. Circuits Syst. I: Reg. Papers*, vol. 58, no. 10, pp. 2285–2295, 2011.

[82] D. Puccinelli and M. Haenggi, "Wireless sensor networks: applications and challenges of ubiquitous sensing," *IEEE Circuits Syst. Mag.*, vol. 5, no. 3, pp. 19–31, Sep., 2005.

[83] X. Jia, Q. Feng, T. Fan, and Q. Lei, "RFID technology and its applications in internet of things (IoT)," in *Proc. Int. Conf. Consum. Electron. Commun. Netw. (CECNet)*, Apr. 2012, pp. 1282–1285.

[84] A. W. Nagpurkar and S. K. Jaiswal, "An overview of WSN and RFID network integration," in *Proc. 2nd Int. Conf. Electron. Commun. Syst. (ICECS)*, Feb 2015, pp. 497–502.

[85] L. Wang, L. D. Xu, Z. Bi, and Y. Xu, "Data cleaning for RFID and WSN integration," *IEEE Trans. Ind. Inform.*, vol. 10, no. 1, pp. 408–418, Feb. 2014.

[86] D. Arnitz and M. S. Reynolds, "Wireless power transfer optimization for nonlinear passive backscatter devices," in *Proc. IEEE Int. Conf. RFID (RFID)*, Apr. 2013, pp. 245–252.

[87] A. Costanzo and D. Masotti, "Energizing 5G: Near- and far-field wireless energy and data trantransfer as an enabling technology for the 5G IoT," *IEEE Microw. Mag.*, vol. 18, no. 3, pp. 125–136, May 2017.

[88] S. Thomas and M. S. Reynolds, "QAM backscatter for passive UHF RFID tags," in *Proc. IEEE RFID Conf.*, Apr. 2010, pp. 210–214.

[89] B. S. Cook, R. Vyas, S. Kim, T. Thai, T. Le, A. Traille, H. Aubert, and M. M. Tentzeris, "RFID-based sensors for zero-power autonomous wireless sensor networks," *IEEE Sensors J.*, vol. 14, no. 8, pp. 2419–2431, Aug. 2014.

[90] B. Zhao, N. Kuo, B. Liu, Y. Li, L. Iotti, and A. M. Niknejad, "A 5.8GHz power-harvesting 116mx116m dielet near-field radio with on-chip coil antenna," in *IEEE Int. Solid-State Circuits Conf. (ISSCC) Dig. Tech. Papers*, Feb., 2018, pp. 456–458.

[91] A. Babakhani, "Systems and methods for fracture mapping via frequency-changing integrated chips," Sep. 24 2019, US Patent 10,422,214.

[92] Y. K. Cherivirala, H. Lyu, H. A. Alhowri, A. Babakhani *et al.*, "Wirelessly powered microchips for mapping hydraulic fractures," *SPE J.*, 2019.

[93] N. Iliev and I. Paprotny, "Review and comparison of spatial localization methods for low-power wireless sensor networks," *IEEE Sensors J.*, vol. 15, no. 10, pp. 5971–5987, Oct. 2015.

[94] J. Cota-Ruiz, J. Rosiles, P. Rivas-Perea, and E. Sifuentes, "A distributed localization algorithm for wireless sensor networks based on the solutions of spatially-constrained local problems," *IEEE Sensors J.*, vol. 13, no. 6, pp. 2181–2191, Jun. 2013.

[95] H. Rahmani, Y. Sun, M. Kherwa, S. Pal, and A. Babakhani, "Coherent radiation from a swarm of wirelessly powered and synchronized sensor nodes," *IEEE Sensors J.*, pp. 1–1, 2020.

[96] N. A. Alrajeh, M. Bashir, and B. Shams, "Localization techniques in wireless sensor networks," *Int. J. Distribut. Sensor Netw.*, vol. 9, no. 6, p. 304628, 2013.

[97] G. Mao, *Localization Algorithms and Strategies for Wireless Sensor Networks: Monitoring and Surveillance Techniques for Target Tracking: Monitoring and Surveillance Techniques for Target Tracking.* IGI Global, 2009.

[98] F. Wen, Q. Wan, R. Fan, and H. Wei, "Improved music algorithm for multiple noncoherent subarrays," *IEEE Signal Process. Lett.*, vol. 21, no. 5, pp. 527–530, May 2014.

[99] J. C. Curlander and R. N. McDonough, *Synthetic aperture radar.* Wiley, New York, 1991, vol. 11.

[100] J. C. Mosher and R. M. Leahy, "Source localization using recursively applied and projected (RAP) MUSIC," *IEEE Trans. Signal. Process.*, vol. 47, no. 2, pp. 332–340, 1999.

[101] Qing Chen and Ruolun Liu, "On the explanation of spatial smoothing in MUSIC algorithm for coherent sources," in *Int. Conf. Inf. Sci. and Technol.*, 2011, pp. 699–702.

[102] R. Solimene, G. Leone, and A. DellAversano, "MUSIC algorithms for rebar detection," *J. Geophys. Eng.*, vol. 10, no. 6, p. 064006, 2013.

[103] X. Chen, "Multiple signal classification method for detecting point-like scatterers embedded in an inhomogeneous background medium," *J. Acoust. Soc. Amer.*, vol. 127, no. 4, pp. 2392–2397, 2010.

[104] H. Tang, "DOA estimation based on MUSIC algorithm, masters thesis, linnaeus university, kalmar, sweden, may 2015."

[105] Y. Sun and A. Babakhani, "A wirelessly powered injection-locked oscillator with on-chip antennas in 180-nm SOI CMOS for spectroscopy application," *IEEE Sens. Lett.*, vol. 3, no. 7, pp. 1–4, 2019.

[106] Munkyo Seo, M. Rodwell, and U. Madhow, "A feedback-based distributed phased array technique and its application to 60-GHz wireless sensor network," in *IEEE MTT-S Int. Microw. Symp. Dig.*, Jun. 2008, pp. 683–686.

[107] Y. Sun and A. Babakhani, "Wirelessly-powered dielectric sensor with on-chip antennas in 180 nm soi cmos process," *IEEE Sensors J.*, vol. 19, no. 7, pp. 2613–2620, Apr. 2019.

[108] B. Razavi, "The role of PLLs in future wireline transmitters," *IEEE Trans. Circuits Syst. I, Reg. Papers*, vol. 56, no. 8, pp. 1786–1793, Aug. 2009.

[109] B. Jamali and A. Babakhani, "Wireless time transfer with subpicosecond accuracy based on a fully integrated injection-locked picosecond pulse detector," *IEEE Trans. Microw. Theory Techn.*, vol. 68, no. 1, pp. 160–169, Jan. 2020.

[110] S. Cheng, P. Hallbjorner, and A. Rydberg, "Printed slot planar inverted cone antenna for ultrawideband applications," *IEEE Antennas Wireless Propag. Lett.*, vol. 7, pp. 18–21, 2008.

[111] Nai-Chung Kuo, Bo Zhao, and A. M. Niknejad, "Near-field power transfer and backscattering communication to miniature RFID tag in 65 nm CMOS technology," in *IEEE MTT-S Int. Microw. Symp. Dig.*, May 2016, pp. 1–4.

[112] A. Yakovlev, J. H. Jang, and D. Pivonka, "An 11 μW Sub-pJ/bit Reconfigurable Transceiver for mm-Sized Wireless Implants," *IEEE Trans. Biomed. Circuits Syst.*, vol. 10, no. 1, pp. 175–185, Feb. 2016.

[113] M. Tabesh, N. Dolatsha, A. Arbabian, and A. M. Niknejad, "A power-harvesting pad-less millimeter-sized radio," *IEEE J. Solid-State Circuits*, vol. 50, no. 4, pp. 962–977, Apr. 2015.

[114] H. Rahmani and A. Babakhani, "An integrated battery-less wirelessly powered rfid tag with clock recovery and data transmitter for uwb localization," in *IEEE MTT-S Int. Microw. Symp. Dig.*, 2020, pp. 1–4.

[115] H. Wang, X. Wang, A. Barfidokht, J. Park, J. Wang, and P. P. Mercier, "A battery-powered wireless ion sensing system consuming 5.5 nW of average power," *IEEE J. Solid-State Circuits*, vol. 53, no. 7, pp. 2043–2053, Jul. 2018.

[116] H. Rahmani, M. M. Archang, B. Jamali, M. Forghani, A. M. Ambrus, D. Ramalingam, Z. Sun, P. O. Scumpia, H. A. Coller, and A. Babakhani, "Towards a Machine-Learning-Assisted dielectric sensing platform for point-of-care wound monitoring," *IEEE Sens. Lett.*, vol. 4, no. 6, pp. 1–4, 2020.

[117] B. Jamali, D. Ramalingam, and A. Babakhani, "Intelligent material classification and identification using a broadband millimeter-wave frequency comb receiver," *IEEE Sens. Lett.*, vol. 4, no. 7, pp. 1–4, 2020.